Hardware studies, in-situ prototype calibration and data analysis of the novel multi-PMT digital optical module for the KM3NeT neutrino telescope

Hardware-Studien, In-Situ-Prototyp-Kalibrierung und Datenanalyse des neuartigen multi-PMT digitalen optischen Moduls für das KM3NeT-Neutrinoteleskop

der Naturwissenschaftlichen Fakultät
der Friedrich-Alexander-Universität Erlangen-Nürnberg
zur Erlangung des Doktorgrades Dr. rer. nat.

vorgelegt von
Jonas Reubelt
aus Fürth

Als Dissertation genehmigt von der Naturwissenschaftlichen Fakultät
der Friedrich-Alexander-Universität Erlangen-Nürnberg

Tag der mündlichen Prüfung:	19.11.2018
Vorsitzender des Promotionsorgans:	Prof. Dr. Georg Kreimer
Gutachter:	Prof. Dr. Ulrich Katz Prof. Dr. Alexander Kappes

Abstract

The KM3NeT neutrino telescope is currently being built in the Mediterranean Sea. It will, upon completion, be the first cubic-kilometre-size neutrino telescope in the northern hemisphere. Although the recent discovery of a high-energy cosmic neutrino flux by the IceCube detector was a major breakthrough in the field of neutrino astronomy, the sources of cosmic neutrinos remain unknown. The KM3NeT/ARCA (Astroparticle Research with Cosmics in the Abyss) detector will help to shed light on the question of the origins of high-energy cosmic neutrinos by complementing the IceCube telescope and expanding the field of view into the direction of the Galactic Centre. In addition, open questions in particle physics like fundamental neutrino properties and neutrino oscillations are tackled by the KM3NeT/ORCA (Oscillation Research with Cosmics in the Abyss) detector.

Both sub-detectors consist of a three-dimensional grid of optical sensors, so-called digital optical modules (DOM), which are deployed at different sites in a depth of up to 3500 m. They are designed to measure the Cherenkov radiation of secondary charged particles produced in interactions of neutrinos with nuclei in the water. While the optical sensors of existing neutrino telescopes house only one big photomultiplier tube (PMT), the KM3NeT detector is the first to use a novel type of DOMs housing 31 smaller PMTs. The so-called multi-PMT DOM has crucial advantages compared to conventional optical modules, of which the most important are: a three times larger overall photocathode area; enhanced angular acceptance; intrinsic directional sensitivity; improved photon counting; and improved capability of background suppression.

The focus of this thesis is on the characterisation and selection of optical components for the application in the novel multi-PMT DOM as well as the calibration and in-situ data analysis of prototype DOMs. Specification and characterisation of crucial PMT parameters guarantee high performance and stable operation of the DOMs. By using auxiliary optical devices like reflector rings surrounding the PMTs, the sensitivity of the DOMs has been increased. Since in KM3NeT all data is sent to shore, special electronic devices were developed to transform the PMT signals into hit times and so-called time over thresholds (ToT), significantly reducing the amount of data to be transferred and stored. The determination of the relation between signal charge and ToT is part of this work, enabling the conservation of the information of the signal charge in spite of the significant data reduction. A measurement of the angular acceptance of a fully integrated DOM shows good agreement with Monte Carlo simulations, confirming the superior performance of the multi-PMT DOM compared to conventional single-PMT DOMs. The analysis of in-situ prototype data verifies the capability of self-calibration of single DOMs. In addition, it is shown that by using high multiplicity coincidences, single DOMs are able to identify atmospheric muons and their directional distribution. With the help of radioactive decays of the potassium 40 isotope (^{40}K) in the sea water, the time calibration between PMTs in a DOM can be performed in situ. An accuracy of better than 1 ns is achieved. Furthermore, the efficiencies of the PMTs are determined with such a high precision that even small variations in the quality of the glass spheres surrounding the DOMs can be identified.

Zusammenfassung

Das KM3NeT-Neutrino-Teleskop befindet sich in der Aufbauphase im Mittelmeer. Mit der Fertigstellung wird es das erste kubikkilometer-große Neutrino-Teleskop der nördlichen Hemisphäre sein. Obwohl die kürzlich vom IceCube-Detektor entdeckten, hochenergetischen kosmischen Neutrinos ein großer Durchbruch für die Neutrinoastronomie waren, bleiben die Quellen dieser Neutrinos unbekannt. Durch die Ergänzung des IceCube-Neutrino-Teleskops und die Erweiterung des Sichtfeldes in Richtung des Galaktischen Zentrums wird der KM3NeT/ARCA (Astroparticle Research with Cosmics in the Abyss)-Detektor in Zukunft dabei helfen, die offenen Fragen über die Quellen der höchstenergetischen kosmischen Neutrinos zu beantworten. Zusätzlich wird der KM3NeT/ORCA (Oscillation Research with Cosmics in the Abyss)-Detektor offene Fragen der Teilchenphysik, insbesondere zu fundamentalen Neutrinoeigenschaften und zur Neutrinooszillation angehen.

Beide Detektoren bestehen aus einem dreidimensionalen Raster von optischen Sensoren, sogenannten digitalen optischen Modulen (DOM), die an verschiedenen Standorten in einer Tiefe von bis zu 3500 m aufgebaut werden. Sie sind speziell konzipiert, um die Cherenkov-Strahlung von geladenen sekundären Teilchen, die in Wechselwirkungen von Neutrinos mit Atomkernen im Wasser entstehen, zu messen. Während optische Module von existierenden Neutrino-Teleskopen mit nur einem großen Photosensor (Photomultiplier-Röhre, PMT) ausgestattet sind, werden für den KM3NeT-Detektor erstmals neuartige Module mit 31 PMTs eingesetzt. Das sogenannte multi-PMT DOM hat entscheidende Vorteile gegenüber den konventionellen optischen Modulen. Die wichtigsten Vorteile sind: eine insgesamt dreifach größere Photokathodenfläche; vergrößerte Winkelakzeptanz; intrinsische Richtungssensitivität; bessere Abschätzung der Zahl gemessener Photonen; und bessere Untergrundunterdrückung.

Der Schwerpunkt dieser Arbeit liegt auf der Charakterisierung und Auswahl von optischen Komponenten für das neuartige multi-PMT DOM und auf der Inbetriebnahme, Datenanalyse und Kalibrierung von Prototypen. Die Vorgabe von PMT-Qualitätsparametern sowie deren Messung im Labor garantieren hohe Leistung und stabile Operation der DOMs. Durch die zusätzliche Benutzung von weiteren optischen Instrumenten wie Reflektorringen wird die Sensitivität erhöht. Da im KM3NeT-Experiment alle Daten zur Küste geschickt werden, wurden spezielle elektronische Schaltungen entwickelt, die die analogen PMT-Signale in Startzeiten und Zeiten, in denen sich das Signal über einer bestimmten Schwelle befindet (ToT), umwandeln. Dadurch wird die Datenmenge, die zur Küste übertragen und dort gespeichert werden muss, deutlich verkleinert. Die Bestimmung des Zusammenhangs zwischen der Ladung des PMT-Signals und der ToT ist Teil dieser Arbeit und ermöglicht die Erhaltung der Information über die Ladung des Signals trotz signifikanter Datenreduktion. Die Winkelakzeptanzmessung eines vollständig zusammengebauten DOMs zeigt eine gute Übereinstimmung mit Monte-Carlo-Simulationen und bestätigt die überlegene Sensitivität des multi-PMT DOMs im Vergleich zu konventionellen DOMs, die mit nur einem einzelnen PMT bestückt sind. Die

Analyse von In-Situ-Prototypdaten bestätigt die Fähigkeit der Selbstkalibrierung der DOMs. Zusätzlich wird gezeigt, dass unter Benutzung von koinzidenten Signalen mit hoher Multiplizität sogar einzelne DOMs dazu in der Lage sind, atmosphärische Myonen und deren Richtungsverteilung zu messen. Mit Hilfe von Zerfällen des natürlich im Salzwasser vorkommenden Kalium-40-Isotops kann die Zeitkalibrierung zwischen PMTs in einem DOM in situ durchgeführt und eine Präzision von besser als 1 ns erreicht werden. Darüber hinaus können die relativen Effizienzen der PMTs mit einer Genauigkeit bestimmt werden, mit der sogar kleine Abweichungen in der Qualität der Glaskugeln, die die DOMs umgeben, erkannt werden können.

Contents

Part I

Cosmic neutrinos and their detection

In this part sources, propagation and detection of cosmic neutrinos are introduced. This comprises production mechanisms of neutrinos in the sources, their propagation to Earth and the interactions that produce secondary particles. Additionally, existing and future neutrino telescopes, and their capability to detect these secondary particles are described. Finally, the composition and basic functionality as well as critical parameters of photomultiplier tubes are presented.

Chapter 1

Motivation

Starting in ancient times with observations made with the naked eye, optical astronomy is arguably the oldest field of physics and has been the only possibility to study the cosmos beyond Earth for a long time. The expansion of the observations to different parts of the electromagnetic spectrum covering radio, microwaves, infrared, ultraviolet, X-rays and gamma rays in the 20th century yielded a deeper knowledge of our Universe. With the discovery of cosmic rays by Victor Hess in 1912 [1], another type of cosmic messengers emerged. Cosmic rays are charged particles consisting of protons, alpha particles and heavier nuclei. Similar to photons, cosmic rays cover a wide energy range and have been studied by a variety of experiments. While photons and charged particles are undoubtedly excellent messengers of processes in the Universe, they have important drawbacks. Since cosmic rays consist of charged particles, they are deflected by galactic and extra-galactic magnetic fields. Thus, they loose the directional information about their origin. Photons, however, carry directional information about their source but are often absorbed by dust or other dense matter on their way to Earth.

The neutrino has become a promising candidate to overcome those disadvantages as cosmic messenger. First proposed in 1930 by Wolfgang Pauli [2], it served as a "desperate remedy" to explain the observed continuous spectrum in the beta decay. In 1934, Enrico Fermi published an effective theory of weak interactions, including the neutrino in the pool of elementary particles [3]. Since the direct detection in 1956 by Clyde Cowan and Frederick Reines [4], many experiments have been performed to learn more about the mysterious particle. In 1957, Bruno Pontecorvo formulated the mechanism of neutrino oscillations [5], describing the change of their flavour upon propagation. Evidence was found in 1998 by the Super-Kamiokande collaboration [6], awarded with the Nobel Prize in 2015. Starting in the 1970s, with feasibility studies of underwater neutrino telescopes, the field of neutrino astronomy has employed a number of different experiments working in deep lakes, the deep sea and the deep ice. Finally, in 2012, IceCube, a neutrino telescope at the Antarctic, measured two neutrinos with energies around 1 PeV and attributed them a cosmic origin with a confidence level of greater than 90% [7]. Until the present day, more than 100 cosmic neutrinos with energies between 100 TeV and 10 PeV have been measured by the IceCube detector [8]. In July 2018, the first indication of an extragalactic neutrino source was found as a result of a multimessenger observation of gamma-rays, x-rays, as well as optical and radio photons in coincidence with a high-energy IceCube neutrino [9]. The source likely was the blazar TXS 0506+056 located more than a billion light years away from Earth.

The neutrino complements the conventional cosmic messengers, having important advantages. Since neutrinos are chargeless and only interact via the weak force in the standard model of particle

physics (SM), they can travel to Earth, remaining mostly unspoiled. Furthermore, they can easily escape dense sources and thus carry information from their inside. This information can help to improve the knowledge of the highest-energy acceleration processes in the Universe. The fugitive nature of neutrinos, responsible for their power as cosmic messengers, represents also a great challenge when it comes to detecting them on Earth. Since they interact with matter so rarely, huge detector volumes and advanced measurement techniques are necessary to trace them.

Neutrino telescopes are novel types of particle detectors that aim to measure the direction and energy of high-energy cosmic neutrinos. Since neutrinos cannot be observed directly, neutrino telescopes are designed to measure the signature of secondary particles produced by rare interactions of neutrinos with nuclei in or around the detector. The neutrinos of interest, and thus the charged secondary particles produced, have highly relativistic energies. When propagating through a transparent detector medium like water or ice, the so-called Cherenkov light [10] they produce can be measured by a three-dimensional grid of optical sensors. The recorded signature in space and time allows for the reconstruction of energy and direction of the neutrino.

The KM3NeT neutrino telescope, which is currently in construction, will, upon completion, be the first cubic-kilometre-size neutrino telescope in the northern hemisphere. It is built deep in the Mediterranean Sea, using the sea water as detector medium.

Neutrino astronomy, with the ultimate goal to detect cosmic neutrino point sources, will be covered by the ARCA (Astroparticle Research with Cosmics in the Abyss) sub-detector of KM3NeT. In addition, fundamental properties of neutrinos will be studied with the ORCA (Oscillation Research with Cosmics in the Abyss) sub-detector. For this purpose, atmospheric neutrinos that emerge from interactions of cosmic rays with nuclei of the Earth's atmosphere are used. In particular, neutrino oscillations will be investigated with the main goal to determine the neutrino mass hierarchy. This represents one of the big open questions of particle physics beyond the SM.

Chapter 2

Neutrino astronomy

Neutrinos are uncharged elementary particles with spin 1/2 and very small masses compared to other fermions. They only interact via the weak force and gravity. Three generations of neutrinos exist: the electron neutrino, the muon neutrino and the tau neutrino as well as their respective antiparticles. In order to extend the spectrum of observation methods of the high-energy Universe, neutrino astronomy focuses on the detection of neutrinos from the most powerful processes in the Universe. These processes, which by the current state of scientific knowledge produce neutrinos in large numbers, are described in this chapter. Furthermore, propagation, interaction and detection of neutrinos are discussed.

2.1 Neutrino sources

There is a variety of neutrino sources in the Universe, producing neutrinos in a wide energy range. Figure 2.1 shows terrestrial and cosmic sources of neutrinos and their fluxes as a function of their energy.

At the low energy end, neutrinos from the cosmic neutrino background (CνB), also called cosmological neutrinos, that emerged approximately one second after the Big Bang when they decoupled from electrons and protons are expected. Their energy has since decreased dramatically due to the expansion of the Universe to energies around 10^{-3} eV.

At energies of roughly 1 MeV terrestrial neutrinos from natural radioactive decays or reactor neutrinos (e.g. $n \rightarrow p + e + \bar{\nu}$) as well as solar neutrinos stemming from nuclear fusion in the Sun dominate the neutrino spectrum.

Another known source of neutrinos are supernova explosions. When a massive star reaches its last stage of evolution, it increases in size and luminosity. With the radiation pressure powered by the nuclear fusion fading, the gravitational force causes a collapse that is followed by an explosion. During these processes, a large number of neutrinos is produced, carrying away 99% of the released energy. 20 neutrinos from the supernova 1987A have been measured in the energy range from 6.3 to 40 MeV by the Kamiokande-II [12] and the IMB [13] experiments.

Atmospheric neutrinos emerge e.g. from interactions of cosmic rays with the Earth's atmosphere. When a cosmic ray proton hits a nucleus of the atmosphere, charged pions can be produced:

$$p + X \rightarrow Y + \pi^{\pm} \,. \tag{2.1}$$

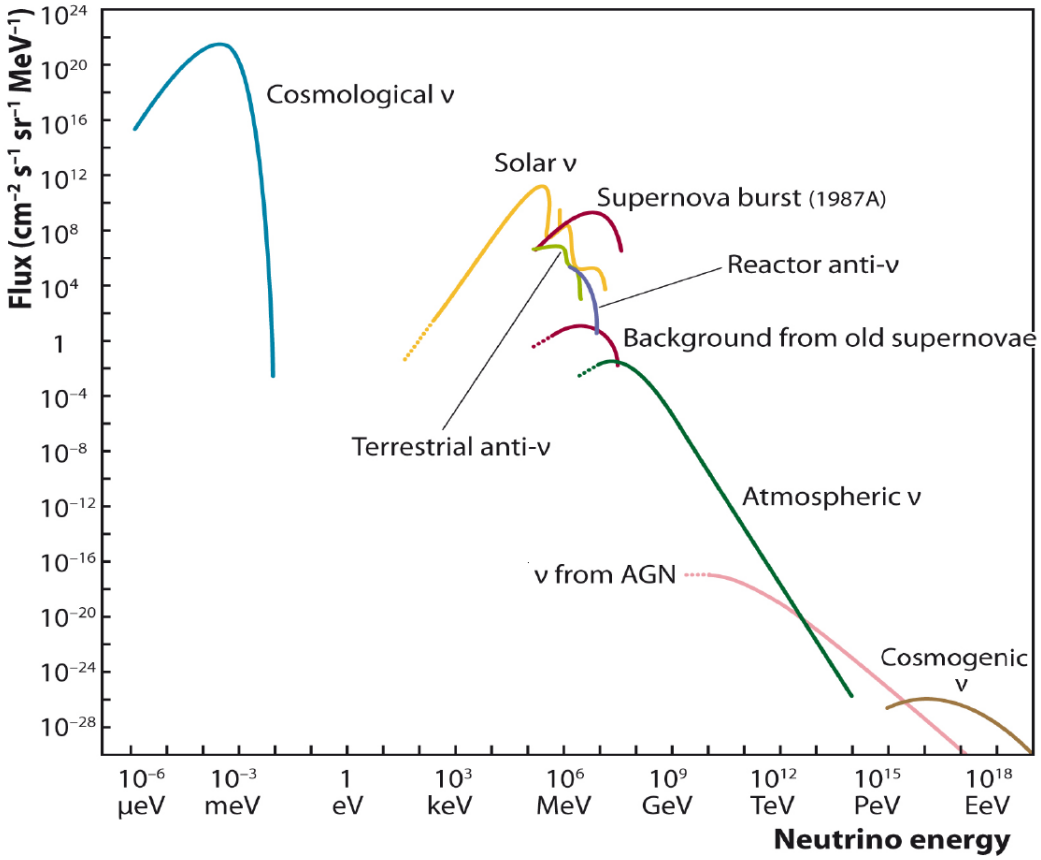

Figure 2.1: *Fluxes of different terrestrial and cosmic neutrino sources. Figure taken from [11].*

These pions then decay into muons and muon neutrinos and their antiparticles:

$$\pi^{\pm} \rightarrow \mu^{\pm} + \overset{(-)}{\nu}_{\mu} . \tag{2.2}$$

Shortly afterwards the muons (anti-muons) decay into electrons (positrons), muon-neutrinos (muon anti-neutrinos) and electron anti-neutrinos (electron-neutrinos):

$$\mu^{\pm} \rightarrow e^{\pm} + \overset{(-)}{\nu}_{\mu} + \overset{(-)}{\nu}_{e} . \tag{2.3}$$

Starting at energies of the order of magnitude of the muon and pion masses ($m_{\mu} = 106\,\text{MeV}$, $m_{\pi} = 140\,\text{MeV}$), the upper limit of atmospheric neutrino energies is determined by the GZK cut-off [14,15], which hinders cosmic ray protons with energies above $\approx 10^{20}\,\text{eV}$ from reaching the Earth. These highest energetic protons interact with photons of the cosmic microwave background (CMB) by pion photoproduction via the Δ^{+} resonance:

$$p + \gamma_{CMB} \rightarrow \Delta^{+}(1232) \rightarrow p + \pi^{0} \tag{2.4}$$

and

$$p + \gamma_{CMB} \rightarrow \Delta^{+}(1232) \rightarrow n + \pi^{+} . \tag{2.5}$$

Protons with energies of $\approx 10^{20}\,\text{eV}$ that contribute to the pion photoproduction have a mean free path of the order of Mpc. Thus, cosmic rays from extragalactic sources, which are understood to exclusively contribute to the highest energy flux, will eventually interact and not reach the Earth.

The highest energetic (ultra-high energy = UHE) neutrinos are produced in galactic and extra-galactic accelerators. Potential phenomena being able to produce such UHE neutrinos are listed below.

Supernova Remnants (SNR) are relics of supernova explosions. The matter ejected after the core collapse forms shock fronts that propagate into the interstellar matter with velocities of up to 10% of the speed of light. Charged particles, however, can be accelerated to much higher energies by multiple scattering at inhomogeneities of magnetic fields in the shock fronts. This process is called Fermi acceleration and is described in detail in [16]. Protons can then interact with the shock front or the interstellar matter in the vicinity of the SNR and produce neutrinos via the Equations 2.1, 2.2 and 2.3.

Active Galactic Nuclei (AGN) consist of a super-massive black hole in the centre of a galaxy surrounded by an accretion disk and so-called jets with relativistic matter outflows. These jets can, similar to SNRs, form shock fronts but are believed to accelerate protons to even higher energies. The production mechanisms of neutrinos again follow Equations 2.1, 2.2 and 2.3. If neutrons are created by the interaction of protons with photons via Equation 2.5, and they can escape the jet, they can decay into protons, electrons and electron antineutrinos via:

$$n \rightarrow p + e + \bar{\nu}_e \,. \tag{2.6}$$

Gamma Ray Bursts (GRB) are supposed to be the most powerful processes in the Universe where enormous amounts of gamma rays are released within a few seconds. The most common illustration of a GRB is the fireball model [17] where e.g. a star collapses into a black hole. During this process, a large amount of matter is ejected, forming highly relativistic shock fronts. If the outermost layer is overhauled by its successors, Fermi acceleration can accelerate protons to ultra-high energies. Via photo-meson production (e.g. Δ-resonance, see 2.5), charged pions can be produced by the interaction of protons and gamma-ray photons, which then decay into neutrinos as shown in the Equations 2.2 and 2.3 [18].

The deficit in the spectrum of atmospheric neutrinos caused by the GZK cut-off provides an additional neutrino source: the **cosmogenic neutrinos** [19]. These neutrinos emerge when the charged pions from Equation 2.5 decay into muon neutrinos and electron neutrinos, amongst other particles. Together with neutrinos stemming from reactions of high-energy cosmic rays with cosmic photon backgrounds, the GZK neutrinos form the cosmogenic neutrinos.

2.2 Neutrino propagation and interaction

The fact that neutrinos only interact via the weak force in the standard model of particle physics (SM) makes them an excellent messenger for the detection and localisation of cosmic accelerators. Since charged particles like electrons, protons or heavier nuclei as well as photons, often struggle to escape dense sources due to electromagnetic interactions, they only give information about processes in the border areas of the sources. In addition, on their way to Earth, charged particles are deflected by galactic or extragalactic magnetic fields and lose the information of their original direction. Photons, however, point back to their sources, but can be absorbed by dust and interstellar media or by interaction with radiation fields. Since neutrinos are not deflected by magnetic fields and are rarely absorbed by matter, they carry direct information about their origin. This advantage, however, complicates their detection on Earth and requires advanced measurement techniques that are described in the following sections.

2.3 Neutrino detection

The fugitive nature of neutrinos, which makes them unique cosmic messengers, is also a big challenge when it comes to their detection. The interaction most relevant for this work is deep-inelastic scattering of neutrinos on nucleons at energies above 10 GeV. Feynman diagrams of neutral-current (Z^0 as mediator) and charged-current ($W^\pm$ as mediator) interactions are shown in Figure 2.2. The charged secondary particles can form showers (e.g. in the neutral-current or electron neutrino charged-current channels) or tracks (in the muon neutrino charged-current channel). In both cases charged particles with energies high enough for them to be superluminal in a medium (not vacuum) are produced. When these particles propagate in a transparent, polarisable medium, the produced Cherenkov radiation [10] can be measured by optical sensors; see Figure 2.3 for a schematic. The characteristic angle θ_C, under which the Cherenkov light is emitted, is given by

$$\theta_C = \arccos\left(\frac{1}{n\beta}\right), \tag{2.7}$$

where n is the refractive index of the medium and $\beta = \frac{v}{c}$ is the velocity of the charged particle. For relativistic particle energies ($\beta \approx 1$) and a refractive index of water, $n_{water} = 1.33$, the Cherenkov angle is 41°. Depending on the energy, the above-mentioned showers and tracks can have extensions exceeding traditional detector sizes by far. For the reconstruction of the energy and the direction of a particle, it is useful to contain the whole signature of a shower or track in the detector. By using naturally occuring water or ice, one can achieve huge detector volumes by installing 3-D arrays of photodetectors in it. Predestined locations for the construction of a so-called neutrino telescope are the deep sea, deep ice or deep lakes. All three possibilities were explored and working neutrino telescopes were built. The ANTARES telescope in the Mediterranean Sea as well as the IceCube detector in the deep ice at the South Pole will be described in the following sections.

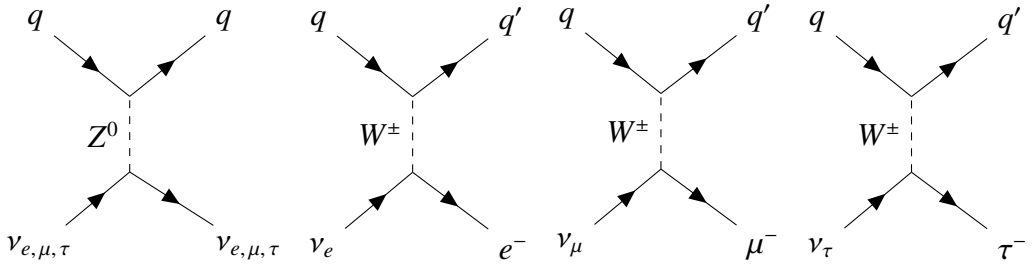

Figure 2.2: *Neutral-current (left) and charged-current weak interactions of neutrinos with the quark constituents of nucleons. Time runs from left to right. Arrows in positive time direction indicate particles, those in negative time direction indicate antiparticles.*

2.4 ANTARES

The ANTARES (Astronomy with a Neutrino Telescope and Abyss environmental RESearch) detector is the first-ever working deep-sea neutrino telescope [20]. Its primary scientific goal is the detection of cosmic neutrinos emitted from galactic or extragalactic sources. It is located in the Mediterranean

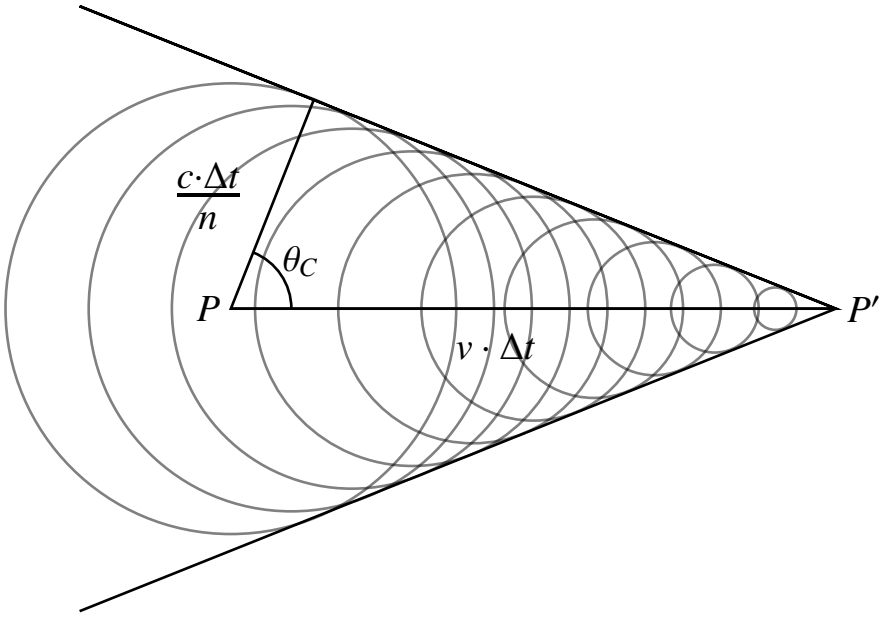

Figure 2.3: *If a charged particle moves with superluminal speed from point P to P' in a transparent medium, Cherenkov light is emitted under the characteristic angle $\theta_C = \arccos\left(\frac{1}{n\beta}\right)$, where n is the refractive index of the material and $\beta = \frac{v}{c}$ the velocity of the charged particle.*

Sea at a depth of 2475 m, roughly 40 km offshore the city of Toulon on the French coast. The ANTARES detector comprises 12 so-called strings, anchored at the seabed and pulled upwards by buoys. Each string is equipped with 25 storeys, each carrying three optical modules (OM) and an electronics container. An OM consists of a pressure-resistant glass sphere, housing a 10-inch photomultiplier tube (PMT) facing 45° downwards, a high-voltage base and magnetic shielding. The supply voltage and PMT signals are transferred via copper cables from the electronics container to the OM and vice versa. The data of all strings is gathered at the so-called junction box and is sent to shore via optical fibres. In addition to the optical components, ANTARES also comprises acoustical instruments. A few storeys consist of a composition of hydrophones instead of OMs. The AMADEUS (ANTARES Modules for the Acoustic Detection Under the Sea) project studies the feasibility of acoustic detection of UHE neutrinos [21]. Figure 2.4 shows a schematic of the structure and composition of ANTARES.

The pattern of Cherenkov light, emitted by charged secondary particles of neutrino interactions in or near the detector, follows characteristic event shapes (tracks or showers, see Section 2.3). These signatures can be resolved in position and time by the 3-D grid of OMs, allowing for the reconstruction of energy and direction of the neutrinos. To achieve a reasonable accuracy, a precise calibration of the detector is inevitable. Position calibration of the OMs is achieved by an acoustic positioning system using triangulation, where signals are emitted from the seabed and are measured at several storeys at each line [22]. The orientation of the OMs is calibrated with a compass and a tiltmeter. For time synchronisation, light pulses running through the optical fibres and light pulses emitted by LEDs and measured by the PMTs are used.

There are some background sources that complicate the measurement of cosmic neutrinos. These are the dark rates of the PMTs themselves (see Section 4.9), photon-emitting deep-sea organisms (bioluminescence) and radioactive decays of the ^{40}K isotope (see Section 3.4) as well as

atmospheric neutrinos and atmospheric muons.

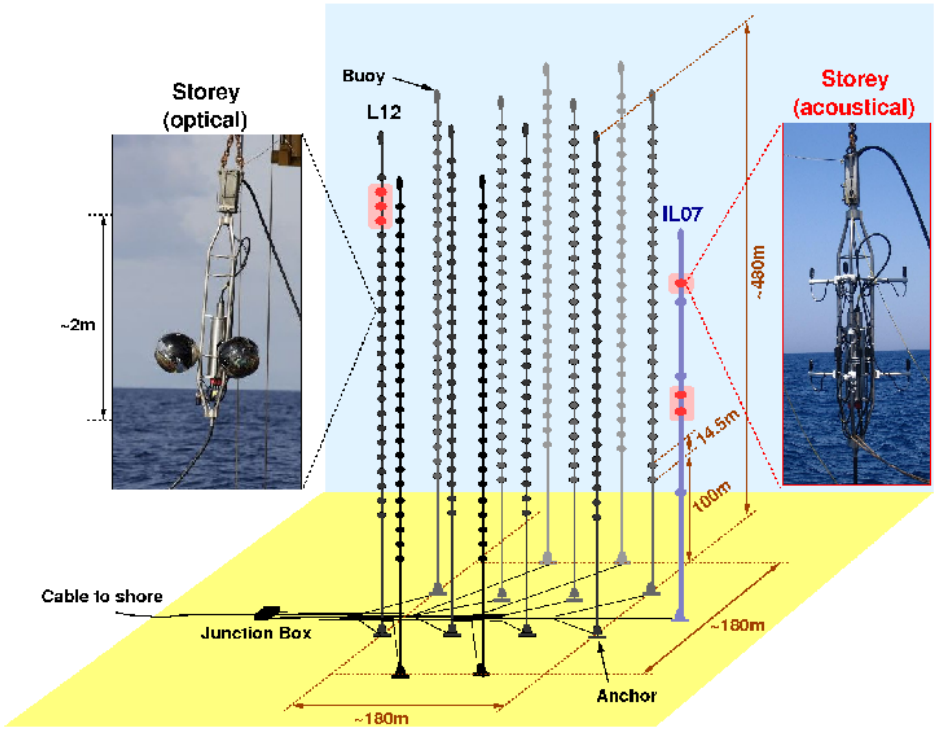

Figure 2.4: *Schematic of the ANTARES neutrino telescope. Storeys equipped with hydrophones (acoustical storeys) are marked in red. Figure taken from [23].*

While not having discovered neutrino point sources in the Universe yet, the ANTARES collaboration has published a large amount of scientific results since the start of data taking in 2007. These are e.g. upper limits on the diffuse muon neutrino flux and measurement of neutrino mixing parameters being conformable with other experiments [24]. Last but not least, planning, construction and running of ANTARES have produced a good deal of expert knowledge and experience nourishing the development of subsequent projects with the motivation to eventually discover cosmic neutrino point sources.

2.5 IceCube

The IceCube Neutrino Observatory [25] is a second-generation neutrino telescope located at the South Pole with its optical sensors buried up to 2450 m into the Antarctic ice. It is the successor of the AMANDA (Antarctic Muon and Neutrino Detector Array) project [26], but has much larger dimensions. IceCube consists of 86 strings expanding vertically from a depth of 1450 to 2450 m with a mean horizontal distance of 125 m between neighbouring strings. Each string holds 60 digital optical modules (DOM) with a vertical spacing of 17 m, adding up to a total amount of 5160 DOMs for the whole detector. In addition, another 324 DOMs compose IceTop, which is a surface detector constructed as a veto for atmospheric muons and atmospheric neutrinos [27] and can also

be used as an independent air shower detector. In order to lower the energy threshold of detectable neutrinos, one part of the IceCube detector is instrumented much denser. This sub-detector is called DeepCore [28] and consists of 7 standard IceCube strings plus 6 strings with vertical DOM spacings of 7 m. As a consequence, the mean horizontal distance between strings in the DeepCore region is reduced to 72 m. In addition, DeepCore DOMs house PMTs with enhanced quantum efficiency (see Section 4.2). A schematic of the IceCube detector is shown in Figure 2.5, the instrumented volume is roughly one cubic kilometre. An IceCube DOM [29] consists of a 10-inch PMT facing downwards, surrounded by a pressure-resistant 13-inch glass sphere, magnetic shielding, readout electronics and calibration devices. Analogue PMT signals are digitised in the DOM and then sent to the surface.

The science goals of IceCube include the detection of ultra-high energy neutrinos from point sources, the search for exotic particles like WIMPs or magnetic monopoles, as well as the establishing of a supernova warning system. Due to the low rate of dark counts and other optical background of the IceCube DOMs in the cold vicinity of the Antarctic ice, a small overall increase of the count rate due to a large flux of MeV neutrinos from a supernova explosion in our Galaxy could be detected [30]. IceCube's scientific discoveries comprise the measurement of more than 100 cosmic neutrinos between energies of 100 TeV and 10 PeV [8]. In July 2018, a multimessenger observation of the blazar TXS 0506+056 was announced. The measurement of a high-energy neutrino with the IceCube detector in spatial coincidence with gamma-ray, x-ray, optical and radio photon observations indicate that the first extragalactic neutrino source has been found [9].

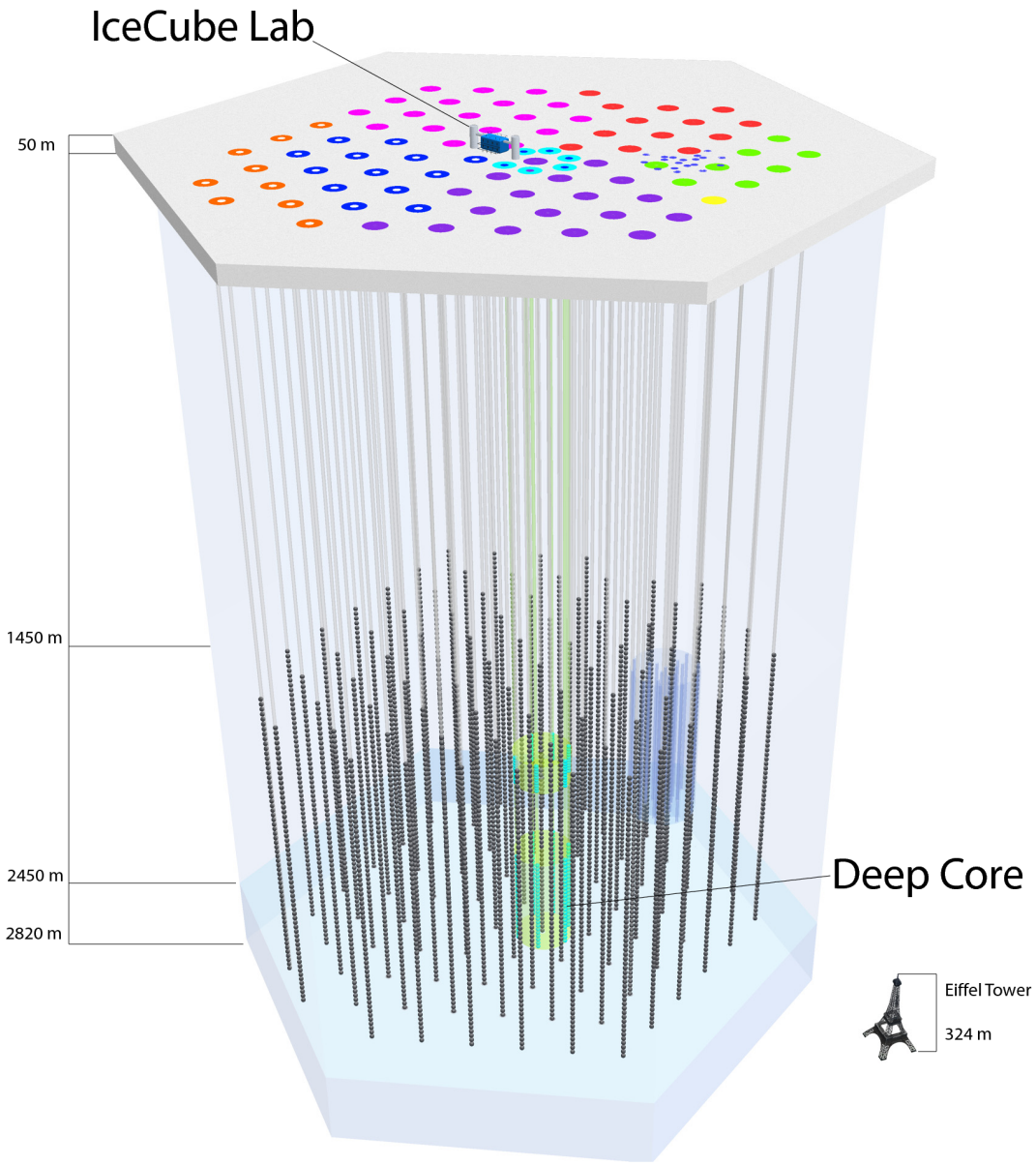

Figure 2.5: *Schematic of the IceCube neutrino telescope. Figure taken from [31].*

Chapter 3

KM3NeT

Given the success of the ANTARES neutrino telescope but considering its small size, it was decided in 2002 that a cubic kilometre scale neutrino telescope should be built in the northern hemisphere, with the intention to complement the IceCube Observatory at the South Pole. Including the centre of our Galaxy, the field of view of such a telescope would expand the coverage of the sky for the search for diffuse and directed cosmic neutrino fluxes. Initiated by this idea, the KM3NeT collaboration was formed by the existing Mediterranean neutrino telescope community. In 2006, a conceptual design report was published [32], followed by a technical design report in 2008 [33]. This Design Study and the subsequent Preparatory Phase were funded by the EU. In 2016, the letter of intent for KM3NeT 2.0 ARCA (Astroparticle Research with Cosmics in the Abyss), studying high-energy cosmic neutrinos, and ORCA (Oscillation Research with Cosmics in the Abyss) was published [34], introducing another scientific goal, namely to study neutrino oscillations and to measure the neutrino mass hierarchy.

During the preparation phase, prototypes of a digital optical module (DOM) [35] and a detection unit (DU) [36] have been successfully deployed and tested. At the end of 2015, the first full line was deployed and since then, data analysis and successive line construction and deployment have run in parallel.

3.1 Detector design

In its complete configuration, KM3NeT will consist of several building blocks each comprising a total of 115 strings with 18 DOMs each. The so-called detection units (DU) are anchored at the seabed and pulled upwards by submerged buoys. Figure 3.1 shows an artist's view of one KM3NeT building block. Although the dimensions of the ARCA (horizontal distance between lines: 90 m, vertical distance between DOMs: 36 m) and ORCA (horizontal distance between lines: 20 m, vertical distance between DOMs: 6 m) building blocks will be different due to optimisation for their scientific goals, the same technology will be used for both. Figure 3.2 shows a comparison of the footprints of an ARCA and an ORCA building block.

Each KM3NeT DOM contains 31 close to isotropically distributed 3-inch PMTs in a 17-inch glass sphere, allowing for an almost 4π coverage in angular acceptance and increasing the overall photocathode area by at least a factor of 3 compared to traditional single 10-inch PMT DOMs. In addition, calibration devices like nano-beacon LEDs for DOM-to-DOM time synchronisation, piezo modules for the acoustic positioning system, compasses and tiltmeters for directional calibration as

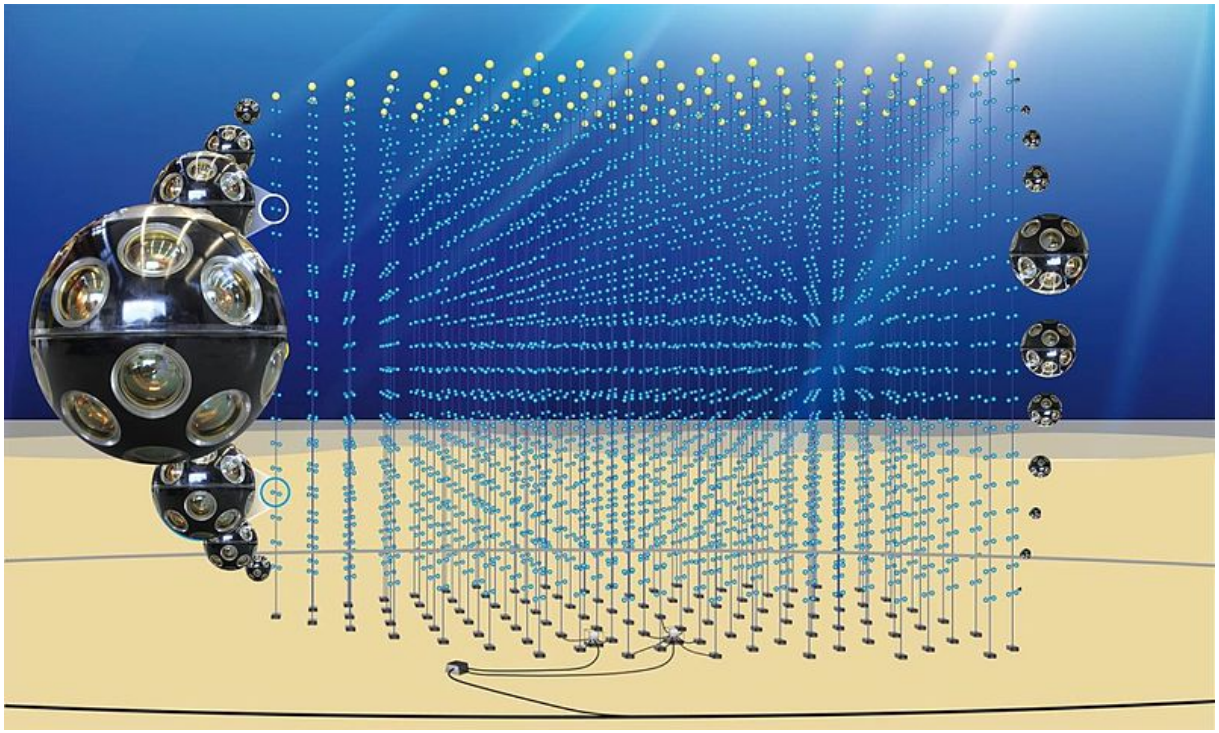

Figure 3.1: *Artist's view of one KM3NeT building block. The vertical lines, also called DUs, are equipped with 18 DOMs each. Figure taken from [37].*

well as components for signal processing are fitted into the DOMs. The analogue PMT signals (see Chapter 4 for a detailed description) are transformed into a rectangular signal by using a comparator and an adjustable threshold. The length of this rectangular signal, the so-called time-over-threshold (ToT), the start time of the signal and the PMT ID constitute the data of a so-called hit. The ToT provides a measure of the charge of the original signal, and the relation between both is discussed in Chapter 8 and is subject of this work.

3.2 Data acquisition

Since in KM3NeT all digitised data is sent to shore to be further processed, efficient filters are needed to reduce the amount of data to be stored on hard drives. The total data stream of a KM3NeT building block will be roughly 25 Gb/s, which has to be reduced by a factor of 10^5. In order to reduce the data size, different filters have been developed.

The level-zero trigger (L0) is the threshold that a PMT signal has to reach in order to initiate a hit. The L0 trigger is thus the only filtering applied off-shore. The level-one trigger (L1) requires at least two PMT hits on one DOM in a certain time window (e.g. 10 ns). This filter efficiently eliminates the dark rate of the PMTs as well as most of the bioluminescence induced signals. The L1 rate of a DOM is of the order of 1000 Hz. It mainly consists of ^{40}K and random coincidences which can be further reduced by cutting on the angle between affected PMTs. Another level of triggering can be introduced by requesting e.g. five or more L1 coincidences on several DOMs in a time window of the order of hundred of microseconds, taking into account the light emission properties of tracks

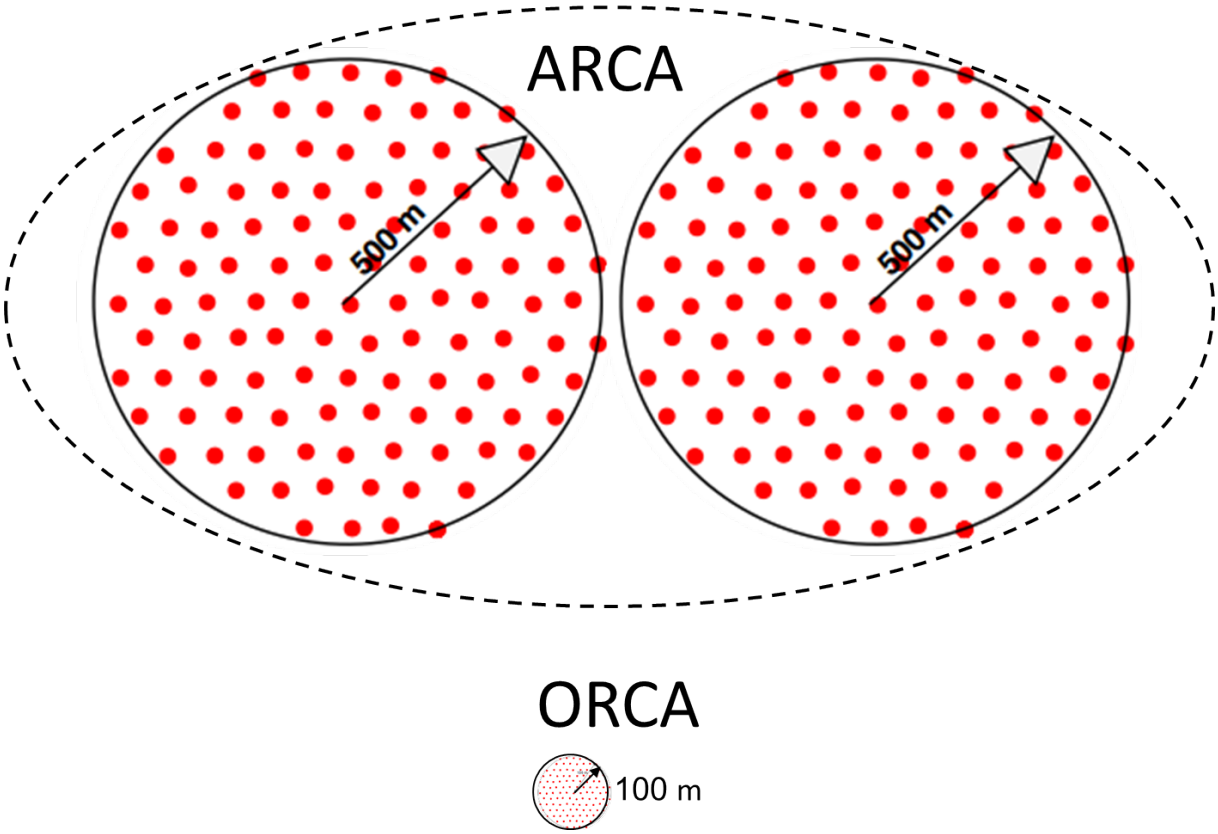

Figure 3.2: *Footprints of ARCA and ORCA. Figure taken from [37].*

and showers in sea water. In this case all hits in a certain time window around the first triggered hit are stored, called snapshot hits and comprise an event.

A period of data taking with constant environmental conditions is called a run. The events of a run are stored on hard drives and can be analysed by dedicated algorithms for shower or track reconstructions. For more details on data acquisition and reconstruction see [34].

3.3 Science case

As mentioned above, KM3NeT is divided into two subprojects, ARCA and ORCA. While ARCA is looking for high-energy cosmic neutrinos either from the diffuse flux or from point sources, ORCA is designed to be sensitive to lower energetic atmospheric neutrinos in order to determine the neutrino mass hierarchy.

Motivated by the IceCube discovery of a high-energy astrophysical neutrino flux [38], detailed simulations of the response of a future ARCA detector to such a neutrino flux have been performed [34] to study the potential of investigating such a signal with KM3NeT. Figure 3.3 shows the significance of the detection of an IceCube-like diffuse neutrino flux over time with two ARCA building blocks. The cascade channel is shown in red and the track channel in black. The error bands stem from the uncertainties in the conventional and prompt neutrino fluxes. The result of a combined analysis is shown in blue. A significance of $5\,\sigma$ will be reached in two years.

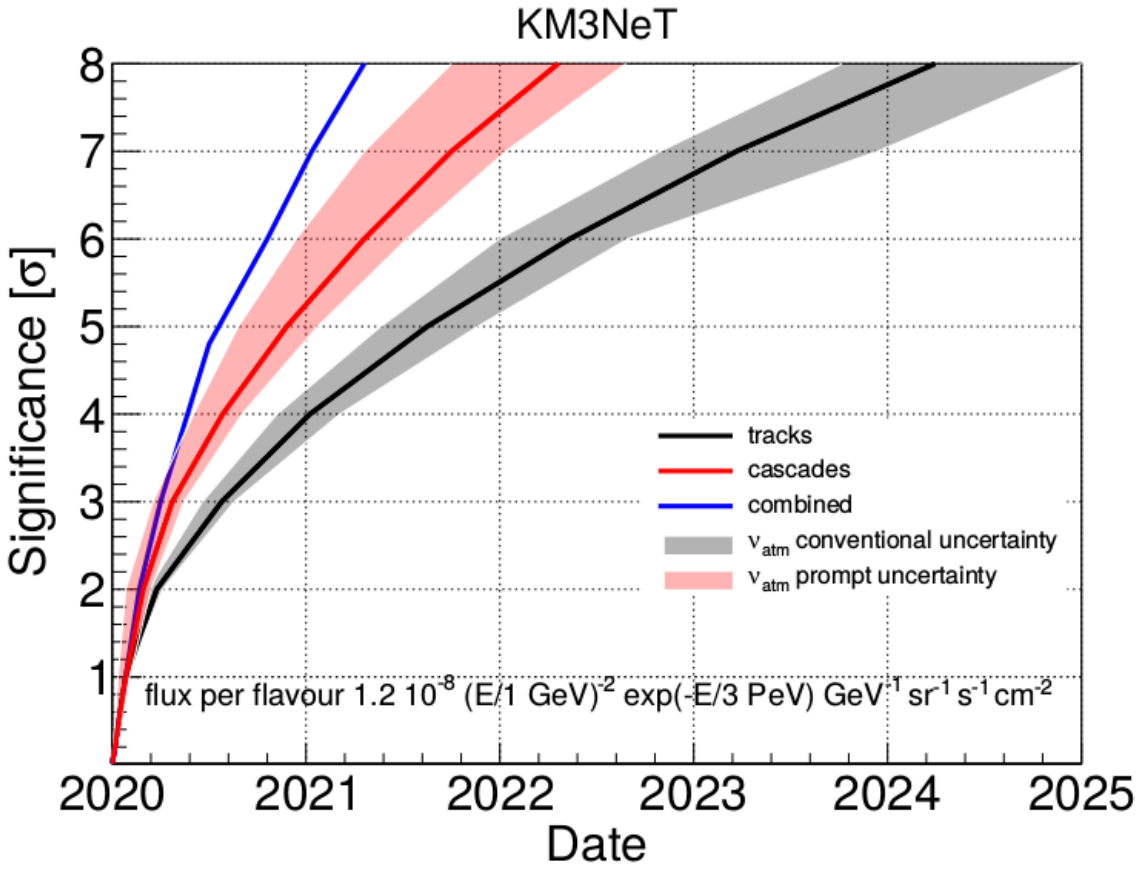

Figure 3.3: *Sensitivity of the KM3NeT detector to the high-energy diffuse neutrino flux reported by IceCube. The cascade channel is shown in red and the track channel in black. Error bands are due to uncertainties in the conventional and prompt neutrino fluxes. The results of a combined analysis are shown in blue. Figure taken from [34].*

For ORCA, the determination of the neutrino mass hierarchy with a significance of 3σ can be achieved after three years of data taking. Figure 3.4 shows the time needed to reach a certain significance for the different hierarchies and atmospheric mixing angles. This represents a competitive timeline compared to other experiments.

3.4 Optical background

In addition to track- or shower-like background events such as atmospheric neutrinos or atmospheric muons, the two major contributors to the optical background in the KM3NeT detector are:

- **Bioluminescence** is the capability of organisms to emit optical photons. In the vicinity of the KM3NeT detector these organisms can continuously emit a small number of photons adding up to a significant increase of background rate in the DOMs. In addition, stress-related bursts (higher number of photons in a small time window) can occur on contact with the structure of the detector. Both backgrounds can be significantly reduced by using local coincidences on

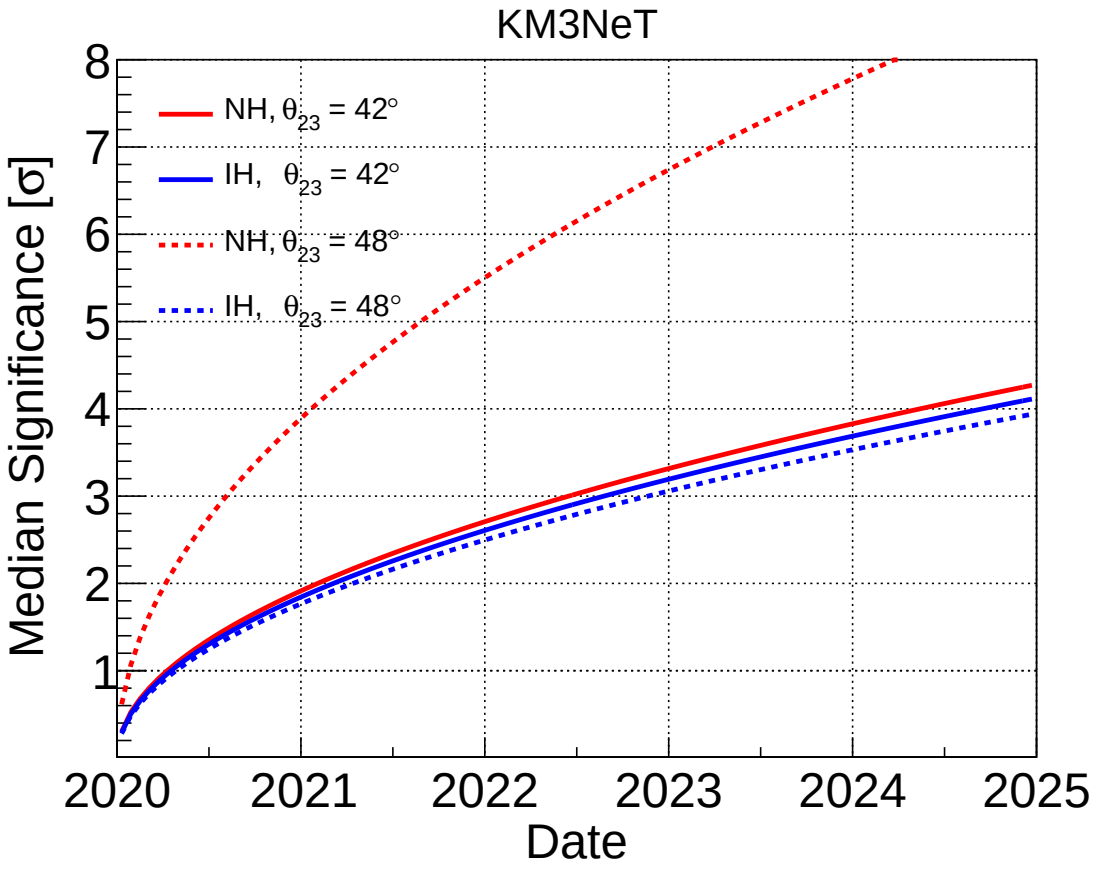

Figure 3.4: *Sensitivity of one ORCA building block to the determination of the neutrino mass hierarchy. Red lines for normal hierarchy, blue lines for inverted hierarchy, solid lines for an atmospheric mixing angle θ_{23} of 42°, dashed lines for $\theta_{23} = 48°$. Figure taken from [34].*

the nanosecond time scale.

- **Potassium 40** is a radioactive isotope naturally occurring in sea water with a half-life of 1.3×10^9 years. Its density and thus the activity per litre highly depends on the salinity of the water. ^{40}K can decay via beta decay

$$^{40}\mathrm{K} \rightarrow {}^{40}\mathrm{Ca} + e^- + \bar{\nu}_e \tag{3.1}$$

with a branching ratio of 89.28%. The arising electron has a maximum energy of 1.3 MeV and can thus be superluminal in sea water. The ^{40}K atom can also decay via electron capture with a branching ratio of 10.72%:

$$^{40}\mathrm{K} + e^- \rightarrow {}^{40}\mathrm{Ar}^* + \nu_e \rightarrow {}^{40}\mathrm{Ar} + \nu_e + \gamma\,. \tag{3.2}$$

In this case, the emerging gamma has an energy of 1.5 MeV and can interact with an electron via the Compton effect. The emitted electron has a maximum energy of 1.3 MeV and is thus also superluminal in sea water. The range after which the electron has lost enough energy to lose superluminal speed and thus the capability of emitting Cherenkov light is of the order of

1 cm. In addition, a dedicated simulation study shows that most of the ^{40}K decays resulting in multiple photon hits on a DOM occur within a 5 m radius around the DOM [39]. Single ^{40}K decays can thus be considered point-like light sources isotropically distributed around the DOM.

Chapter 4

Photomultiplier tubes

Photomultiplier tubes (PMTs) are powerful instruments for the detection of very low amounts of light, finding application in a wide range of scientific and applied fields such as medical diagnoses, spectroscopy, or high energy physics. With the first documented operation of a PMT in 1934, the device has since undergone an enormous evolution in its performance, permitting the possibility of measuring single photons with nanosecond time resolution. In this chapter the design and properties of PMTs are described, especially those important for their application in the KM3NeT project. The descriptions in this chapter follow mainly the references [40] and [41] and references therein.

4.1 Basic functionality

PMTs are vacuum tubes with a photocathode at the entrance window, a dynode system and an anode. The basic structure of a PMT is shown in Figure 4.1. When a photon hits the photocathode of the PMT, there is a chance that a so-called photoelectron is created via the photoelectric effect. Accelerated by electric fields and formed by consecutively increased electric potentials at the dynodes, the electron is focused on the first dynode starting an electron avalanche by producing several secondary electrons which are further amplified from dynode to dynode. The gradation of electric potentials can e.g. be achieved by a voltage divider with several resistances (see Section 4.10).

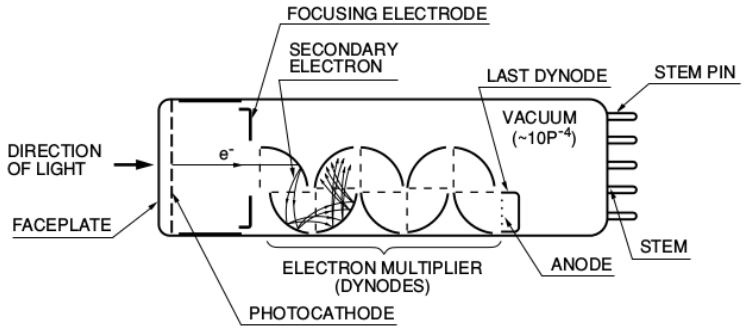

Figure 4.1: *Basic structure of a PMT. Figure taken from [40].*

4.2 Photocathode

Structure and composition

The first step in the photon detection of a PMT is the conversion of incoming photons into electrons, which can then be amplified and monitored. This conversion proceeds via the photoelectric effect discovered by Einstein in 1905.

There is a vast amount of possible photocathode materials that are sensitive to a large spectral range of photons varying from deep UV to infrared wavelengths. Using a combination of materials with two alkali metals, e.g. antimony-rubidium-caesium (Sb-Rb-Cs) or antimony-potassium-caesium (Sb-K-Cs), is referred to as bialkali-photocathode and has good spectral coverage as well as large quantum efficiency and small dark rate. Considering those advantages combined with relatively low cost, PMTs with bialkali-photocathodes are currently integrated in DOMs for the KM3NeT project.

Sensitivity

The sensitivity of the photocathode of a PMT is often described as the quantum efficiency (QE). The quantum efficiency is given by the number of photoelectrons emitted by the photocathode divided by the number of incident photons at the photocathode. The energy of the incoming photon is transferred to an electron in the valence band of the photocathode material. If the energy of the electron is high enough so that it can escape the photocathode material, it can be liberated and further propagated to form a signal. The energy of a photon is inversely proportional to its wavelength and thus the quantum efficiency of a PMT is highly wavelength-dependent. Another measure of the sensitivity of a photocathode is the radiant sensitivity S_k. It is described by the quotient of the photoelectric current I_k and the radiant flux L_p of a light source:

$$S_k = \frac{I_k}{L_p}\,. \tag{4.1}$$

The quantum efficiency can be calculated using the radiant sensitivity:

$$\mathrm{QE} = \frac{h \cdot c}{\lambda \cdot e} \cdot S_k = \frac{1240\,\mathrm{Wm/A}}{\lambda} \cdot S_k\,, \tag{4.2}$$

where h is the Planck constant, c the speed of light in vacuum, λ the wavelength of the photons and e the elementary charge.

A usual setup to determine the quantum efficiency of a PMT, $\mathrm{QE_{PMT}}$, is to connect the dynodes electrically with the anode and count the photoelectrons by measuring the resulting current I_{PMT}. Using, e.g., a photodiode (PHD) with known quantum efficiency $\mathrm{QE_{PHD}}$ as a reference (I_{PHD}) and a light source with an illuminated spot smaller than the active areas of the PMT and PHD, it is possible to calculate the quantum efficiency of the PMT as follows:

$$\mathrm{QE_{PMT}} = \frac{I_{\mathrm{PMT}}}{I_{\mathrm{PHD}}} \cdot \mathrm{QE_{PHD}}\,. \tag{4.3}$$

The spectral range of a PMT is limited by cut-offs at short and long wavelengths. While the cut-off at short wavelengths is dominated by the transmittance of the glass of the front window, the cut-off at long wavelengths is limited by the photocathode material and its work function.

4.3 Dynode system

There are many different possibilities to arrange a dynode system in a PMT. Although they all serve different applications, the aim is always to multiply the number of electrons coming from the photocathode to a detectable amount at the anode. To achieve that, the dynode material makes use of the secondary emission of electrons after the impact of an initial electron. The secondary emission coefficients δ_i are hereby responsible for the overall amplification with the total number of electrons arriving at the anode

$$N_t = \delta_i^{N_d} \cdot N_{pe} \,, \tag{4.4}$$

where N_d is the number of dynodes, N_{pe} the number of photoelectrons, assuming that the secondary emission coefficient is equal for all dynodes.

The PMTs to be used in the KM3NeT project are equipped with a combination of box type and linear focused type dynodes [40]. The first two large dynodes (box type) guarantee good collection efficiency, while the further ones, being of linear focused type, provide for an overall low transit time spread (TTS). The collection efficiency is the probability that an electron, emitted by the photocathode (or any dynode), hits the first dynode (or the respective consecutive dynode).

4.4 Anode

Sensitivity

The anode sensitivity S_a can, similar to the photocathode sensitivity, be expressed as the quotient of the anode current I_a and the incident photon flux L_p:

$$S_a = \frac{I_a}{L_p} \,. \tag{4.5}$$

The anode sensitivity of a PMT takes losses like collection efficiency into account and thus more specifically reflects the probability to measure an incoming photon. There are still effects like afterpulses (see Section 4.8) that can contaminate the signal, but can be eliminated by time resolved measurements.

Single electron spectrum

In this section, the response of PMTs to time-separated single photons is described. When a photon-induced electron hits the dynode system, a cascade emerges, where every electron is multiplied by the secondary emission coefficient at each dynode. As this is not a deterministic process because the secondary emission underlies a Poisson distribution, the resulting number of electrons, or charge, at the anode varies for different events. If the voltage of a PMT signal is measured over time, e.g. by an oscilloscope with an input impedance, the area below the signal curve which represents the charge varies from signal to signal. Since, however, the time of arrival of each electron in the cascade also varies due to different flight paths through the dynode system, the shape of the signal diversifies as well. Regarding the distribution of the charge of many single photoelectron events, the shape comes close to a Gaussian distribution as a combined result of the Poissonian spread at each dynode. To distinguish single electron events from electrical noise, a threshold of e.g. 0.3 times the mean charge of a single photoelectron is used as a good compromise between

losing too many signals and using too many noise events. Figure 4.2 shows an example of a single electron charge distribution. The narrow peak on the left represents the electrical noise, also called pedestal. The wider peak on the right represents the single electron peak. To measure such a spectrum one often uses a pulsed light source with very low intensity where the number of photons per pulse is Poisson-distributed, e.g. an LED. This results in a Poisson distribution of the multiplicity of the pulse where the multiplicity is zero for electrical noise and one for single electron pulses. In order to measure a single electron spectrum, the mean of the Poisson distribution is chosen to be far below one, e.g. 0.1 to 0.01, which then results in the suppression of higher multiplicity events.

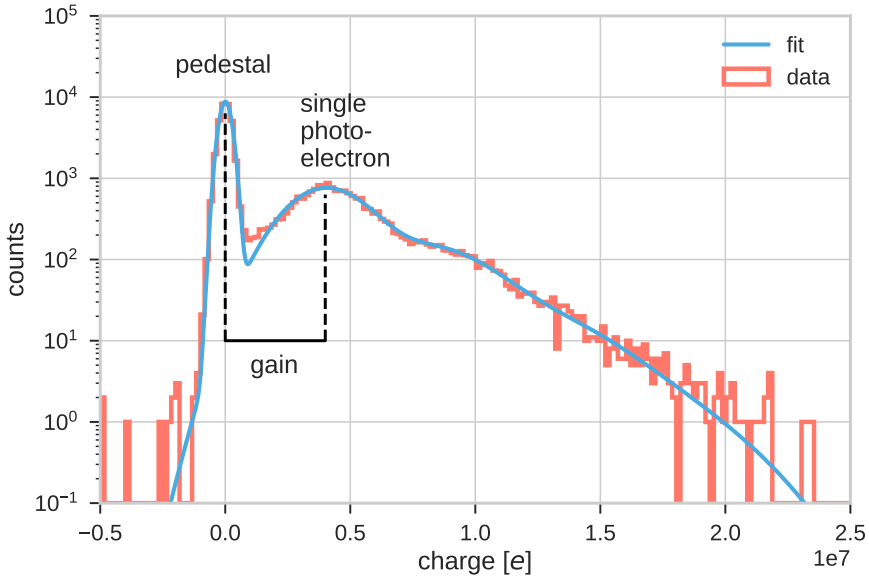

Figure 4.2: *Single photoelectron spectrum of a KM3NeT PMT. It is fitted by the PMT response function described in [42].*

4.5 Gain

The most commonly used measure for the amplification of a PMT is called gain G. It is defined as the quotient of the anode current I_a and the photocathode current I_c:

$$G = \frac{I_a}{I_c}\,. \tag{4.6}$$

The dependence of the gain G on the secondary emission coefficient δ_i of each dynode, the collection efficiencies of the first η, and further dynodes η_i for a PMT with N dynodes is described as:

$$G = \eta \prod_{i=1}^{N} \delta_i \eta_i = \eta \prod_{i=1}^{N} g_i\,. \tag{4.7}$$

where $g_i = \delta_i \eta_i$ is the gain of each dynode, which can be different by production variations or by design. A typical value for g_i is 4 so that the gain of a 10-stage PMT would be $4^{10} \approx 1 \times 10^6$.

It is common practice to increase the secondary emission coefficient of the first dynode, e.g. by increasing the potential between the photocathode and the first dynode, to achieve a better signal to noise ratio. In the scope of this work, gain refers to the gain of the dynode system only, i.e. $G = \prod_{i=1}^{N} g_i$, and the collection efficiency is meant to be the collection efficiency of the first dynode ($CE = \eta$).

4.6 Collection efficiency

The collection efficiency is the ratio of electrons reaching the first dynode and electrons emitted from the photocathode. After a photoelectron leaves the photocathode it is accelerated towards the first dynode by the electric field between photocathode and first dynode. The acceleration process strongly depends on the shape of the electric field, which is often manipulated by the use of so-called focusing electrodes. Furthermore, the collection efficiency depends on the initial speed of an electron when it leaves the photocathode and thus on the wavelength of the incoming photon. Finally, the collection efficiency also depends on the geometrical position where the photoelectron is produced due to the non-homogeneity of the electric field. A typical value for the geometry-averaged collection efficiency of common PMTs is 0.9.

4.7 Timing

The width (FWHM) of a PMT signal caused by a sub-nanosecond long photon pulse strongly depends on the PMT type. For typical 3-inch PMTs used in the KM3NeT project it is of the order of 10 ns. The rise time, defined as the duration of a signal pulse to rise from 10 to 90% of its maximum height, is of similar size. Another important characteristic of a PMT is the transit time. It is defined as the time an electron needs to travel from the photocathode to the anode and is of the order of several tens of nanoseconds. The most crucial timing parameter of a PMT is the time resolution or transit time spread (TTS). It is defined as the width (FWHM) of the distribution of different transit times. The transit time differs for different photoelectron transits due to different flight paths from the photocathode to the first dynode and between the dynodes. It depends on the initial speed of the photoelectron as well as on the voltage between the photocathode and the dynodes. For some PMT designs, the position on the photocathode where the photoelectron is produced is crucial, since the electric field between the photocathode and the first dynode can be highly irregular and the path lengths of the electrons can be different (in particular for PMTs with a flat opening window). That effect can be reduced by choosing a spherical opening window reducing the inhomogeneities of the electric field and the differences of the electron paths. Typical values for the TTS of spherical input window PMTs is 1 to 10 ns (FWHM), depending on their overall size.

4.8 Correlated background probability

Pre-pulses, delayed pulses and afterpulses are spurious pulses that arrive at the anode before or after the main signal pulse. They can be distinguished by their time of arrival and production mechanism.

Pre-pulses arriving before the main pulse can emerge when the photoelectron directly hits the second dynode. The transit time is thus reduced by the time an electron needs to travel from the first to the second dynode (< 10 ns for 3-inch PMTs used in KM3NeT). Another source of pre-pulses are photons passing the photocathode and initiate an electron via the photoelectric effect at the first dynode. The transit time of those pre-pulses is thus reduced by the time an electron needs to travel from the photocathode to the first dynode (15-20 ns for 3-inch PMTs used in KM3NeT).

Delayed pulses are produced when photoelectrons scatter elastically at the first dynode. If the electron is scattered towards the photocathode, it has a chance to be reaccelerated towards the first dynode and produce a pulse. In this case, the delayed pulse replaces the signal pulse but is shifted in time. The maximum time shift is twice the transit time from the photocathode to the first dynode (30-40 ns for 3-inch PMTs used in KM3NeT). To identify these pulses, count their rate and measure the delay time, a pulsed light source with known pulse-emitting time is used. Typical probabilities for delayed pulses are 5 to 10%.

Similar to delayed pulses, fast afterpulses can originate when photoelectrons scatter back from the first dynode but still produce a signal pulse. The fast afterpulse goes then alongside the signal pulse. A second mechanism that produces fast afterpulses is photon feedback produced on electron impact at the dynodes. Mostly red and infrared photons are produced and can trigger photoelectric effects at the photocathode. The maximum time for those fast afterpulses is of the order of the transit time of a PMT (≈ 40 ns for 3-inch PMTs used in KM3NeT). Late afterpulses, in contrast, emerge when electrons ionise residual gas molecules present in the tube and often accumulated at solid components like the dynodes. These molecules are residuals from the evacuation process of the tube or have been penetrating through the glass over time. When ionised, they are accelerated by the electric field in the direction of the photocathode and can, on impact, produce several free electrons. These delayed electrons form an afterpulse that can exceed the charge of the primal signal pulse. Unlike early afterpulses, late afterpulses can be measured separately from the signal pulses they originate from. The time delay of late afterpulses depends on the mass of the ionised gas molecule and the voltage between photocathode and first dynode and can range from several hundreds of nanoseconds to several microseconds. The typical probability that an afterpulse appears is of the order of 5 to 10%, depending on the density of residual gas in the tube.

4.9 Dark rate

The number of signals not induced by optical photons per time of a PMT is called dark rate. A possible origin can be thermionic emission, when an electron in the photocathode can overcome the work function of the material with its thermal energy only. A discrimination between the latter and photon-induced signal events is difficult but can be achieved using coincidences in time, e.g. with the trigger of a light source. Field effects and leakage currents can contribute to the dark rate as well. Another contribution to the dark rate is induced by the ionisation of residual gas in the tube which is also called ion feedback. In addition, cosmic rays, environmental gamma rays and radioactivity in the vicinity or in the PMT material itself, e.g. in the glass, can cause an increased dark rate. If an application contains more than one PMT, the interaction between two or more PMTs can result in electronic or optical cross-talk, which can also contribute to the dark rate.

4.10 PMT bases

Resistive bases

The proper operation of a PMT relies on the use of gradationally arranged electric potentials. The easiest way would be to provide the different high voltages with different power supplies. Since this is a rather impractical solution, a high-voltage supply and a voltage divider are used instead. Figure 4.3 shows a PMT with voltage divider. In addition to the serial connection of resistors to achieve the electric potentials, capacitors are connected in parallel to the resistors between the second to last dynode and last dynode as well as between the last dynode and the anode to provide enough charge for the amplified signal.

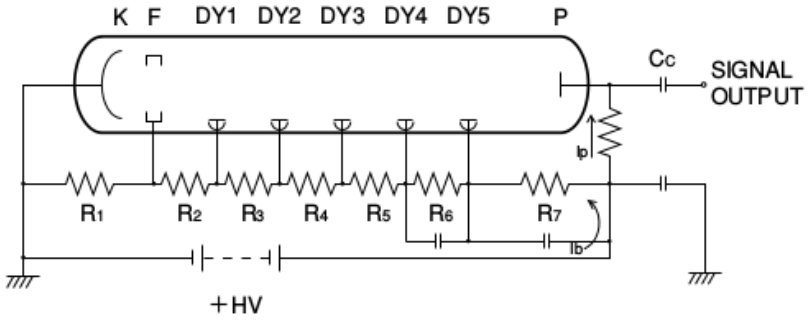

Figure 4.3: *PMT with photocathode (K), focus dynodes (F), dynode system (DY_i) and anode(P). The voltage divider consists of resistors (R_i) and capacitors. Figure taken from [40].*

Cockcroft-Walton bases

A more sophisticated way to accomplish the high voltages needed to drive a PMT is the Cockcroft-Walton multiplier. This technique is often used to convert small DC supply voltages into high DC voltages as well as AC voltages into DC voltages. Figure 4.4 shows the principle introduced by Cockroft and Walton in [43]. The principle idea is to move electric charges from the capacitors X_1 and X_2 to the capacitors C_2 and C_1 which all have the same capacity C, by switching between the connections S_i and S_i' (dashed lines and solid lines). For each additional capacitor C and X another potential difference V_0 is added to the total voltage. This means if there is a base DC voltage of V_0, you end up getting $n \cdot V_0$ if you use $2 \cdot n - 1$ capacitors.

The principle of the multiplication of AC voltages or pulsed DC voltages on the other hand is shown in Figure 4.5. In the example of a pulsed DC signal, each stage (e.g. C_1, C_2, D_1 and D_2) adds the pulse height of V_i to the DC output V_0. In the case of two stages, a square wave signal with a baseline of -1 V and a pulse height of 1 V, the multiplied DC voltage V_0 would be 4 V. By choosing the number of stages n, the output DC voltage becomes $2 \cdot n \cdot V_i$. In this way the different high voltages needed to drive a PMT can be produced on a micro chip level.

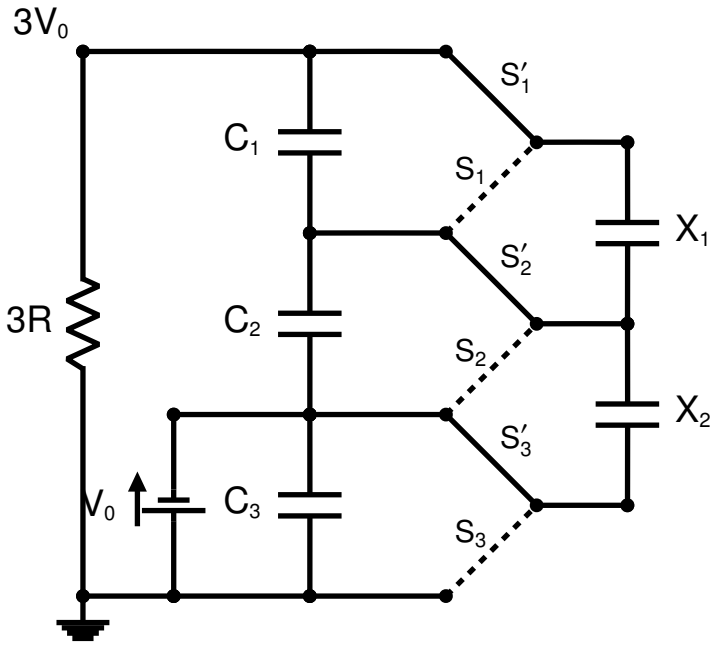

Figure 4.4: *Cockcroft-Walton schematic for DC multiplication. Figure adapted from [43].*

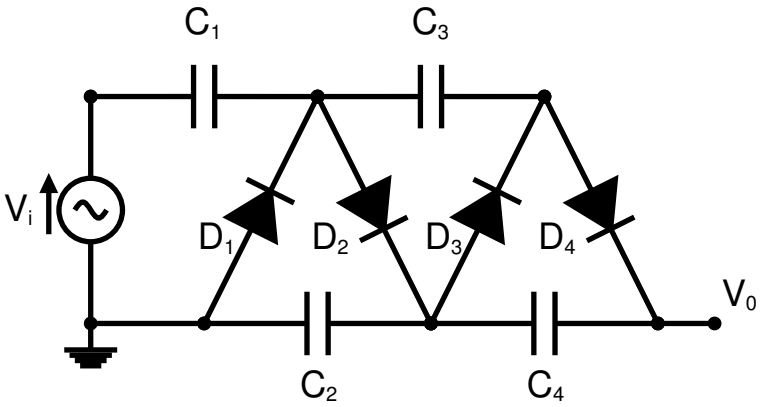

Figure 4.5: *Cockcroft-Walton schematic for AC multiplication and rectification.*

Part II

The digital optical module for KM3NeT

In this part the KM3NeT digital optical module (DOM) is introduced. The major advantages compared to conventional optical modules and the technical design is described. Techniques and results of the measurement of critical photomultiplier tube (PMT) parameters are presented. Furthermore, different PMT candidates and their applicability as photo sensors for the KM3NeT DOM are described. Passive optical components, like the pressure vessel, the optical gel and reflector rings, and their influence on the overall sensitivity of the DOM are examined. The KM3NeT active base and its signal shaping characteristics are investigated and a calibration necessary to conserve the information about the original PMT signal is presented. Finally, the results of angular acceptance measurements of a single PMT and a fully integrated DOM and a comparison to Monte Carlo simulations are shown.

Chapter 5

The multi-PMT design

In contrast to existing neutrino telescopes, whose optical modules feature only one 8 to 10 inch PMT, the KM3NeT collaboration decided to use a different approach for its digital optical modules (DOM). First proposed by S. O. Flyckt, the multi-PMT concept employs several smaller PMTs contained in a glass sphere with more or less evenly distributed angles of view, in addition to read-out electronics and different calibration devices. The KM3NeT DOM was decided to house 31 3-inch PMTs in a 17-inch glass sphere and has several advantages compared to traditional single PMT optical modules of which the most important ones are:

- **Increased photocathode area**: The overall photocathode area of a KM3NeT DOM with 31 3-inch PMTs is approximately three times larger than that of a conventional ANTARES or IceCube module while involving roughly the same cost per photocathode area.

- **Enhanced angular acceptance**: Since in the KM3NeT DOM the active areas of the PMTs are more uniformly distributed, the angular acceptance approximates a $4\,\pi$ coverage, whereas single PMT modules cover half of that at best.

- **Intrinsic directional sensitivity**: The directional information that each registered photon carries can be used in advanced algorithms for event reconstruction due to the segmentation of the photocathode area.

- **Improved photon counting**: The distribution of photons with different arrival times over several PMTs allows for a more precise determination of their number and arrival times.

- **Background suppression**: While the dark rate stays roughly the same per photocathode area when comparing single- and multi-PMT modules, it can be intrinsically suppressed by using coincidences between individual PMTs.

- **Self-calibration**: Using potassium 40 decays in the vicinity of a DOM allows for in-situ timing and efficiency calibration using coincidences, their rates and time differences.

- **Reduced risk**: The increased photocathode area per DOM reduces the number of bore-holes and penetrators in the glass per photocathode area and thus the risk of failure due to leakages.

The development of such a novel optical module involves not only the replacement of one big PMT by 31 small ones but also significant design changes in auxiliary devices and support structures. In addition, new PMT candidates with comparable or better performance in crucial parameters have to be found. Various manufacturers have indicated their interest in producing customised PMT models for the KM3NeT detector. Testing and benchmarking as well as the calibration of these PMT candidates is one of the subjects of this work and is presented in Chapter 6.

With the construction and deployment of several prototype DOMs [35,36], the KM3NeT collaboration has established a proof of concept in technical feasibility and physics capability.

Technical design

Figure 5.1 shows a photograph as well as a blow-up view of the KM3NeT DOM. Crucial components are indicated by names. Each KM3NeT DOM consists of a pressure-resistant 17-inch glass sphere divided into a top and bottom hemisphere. They are held together by a titanium collar surrounding the DOM and by a partial vacuum inside the DOM. Special tape sealing the joint of the two half spheres against the environment is hold in place by all-weather protection tape. Attached to the titanium collar, Dyneema® ropes connect all DOMs of a line. A special vertical electro-optical cable (VEOC), specifically developed for that purpose, is responsible for the data transfer and the power supply of the DOMs. It is an oil-filled plastic hose being at equal pressure compared to the deep sea in order to avoid mechanical stress on the cables and optical fibres. A special penetrator has been designed to guide the power cables and optical fibres through the glass sphere into the DOM.

The power board is in charge of the distribution of the power to the different components, adding up to an overall power consumption of only 7 W per DOM. The waste heat is collected by aluminium structures embedded in the composition of the electronics boards and guided to the top of the DOM where a mushroom-shaped aluminium plate radiates the heat through the glass sphere to the seawater. Keeping the temperature inside the DOM at a constantly low level allows for a stable operation of all electronic devices and especially limits the highly temperature-dependent dark rate of the PMTs.

The PMTs are equipped with conical reflector rings increasing the light collection (see Section 7.3). They are held in place by a 3D-printed support structure. Optical gel is used for optical coupling between the glass sphere and the PMT[1]. An active base provides tunable high voltage for the PMT, using the Cockcroft-Walton technique (see Chapter 8). After a charge-to-voltage conversion, the PMT signal is transformed into a digital time-over-threshold (ToT) signal using a comparator with an adjustable threshold. The ToT signals of each PMT-base pair are collected via two so-called octopus boards in the bottom and top hemispheres. The arrival times and ToTs of every registered photon hit are digitised by a time-to-digital converter implemented in a field-programmable gate array (FPGA) at the central logic board (CLB).

In addition, the CLB is also responsible for the readout of the data from a piezo sensor, tiltmeter, compass and temperature sensors as well as for controlling the nanobeacon. The piezo sensor is glued to the bottom half of the glass sphere and enables, together with acoustic emitters at the sea floor, the acoustic positioning system for the DOMs. Compass and tiltmeter measure the orientation of the DOMs, which has to be monitored continuously due to the floating of the lines caused by sea currents. The nanobeacon is an LED with tunable frequency, length and amplitude of its pulses. It is used for the inter-DOM time calibration (for details see Section 11.2). All data from the PMTs and

[1] Having a refractive index close to that of water and glass, the optical gel provides for a reflection-minimised photon path to the PMT photocathode.

other auxiliary devices are transmitted via optical fibres to the shore, using a unique wavelength for each DOM.

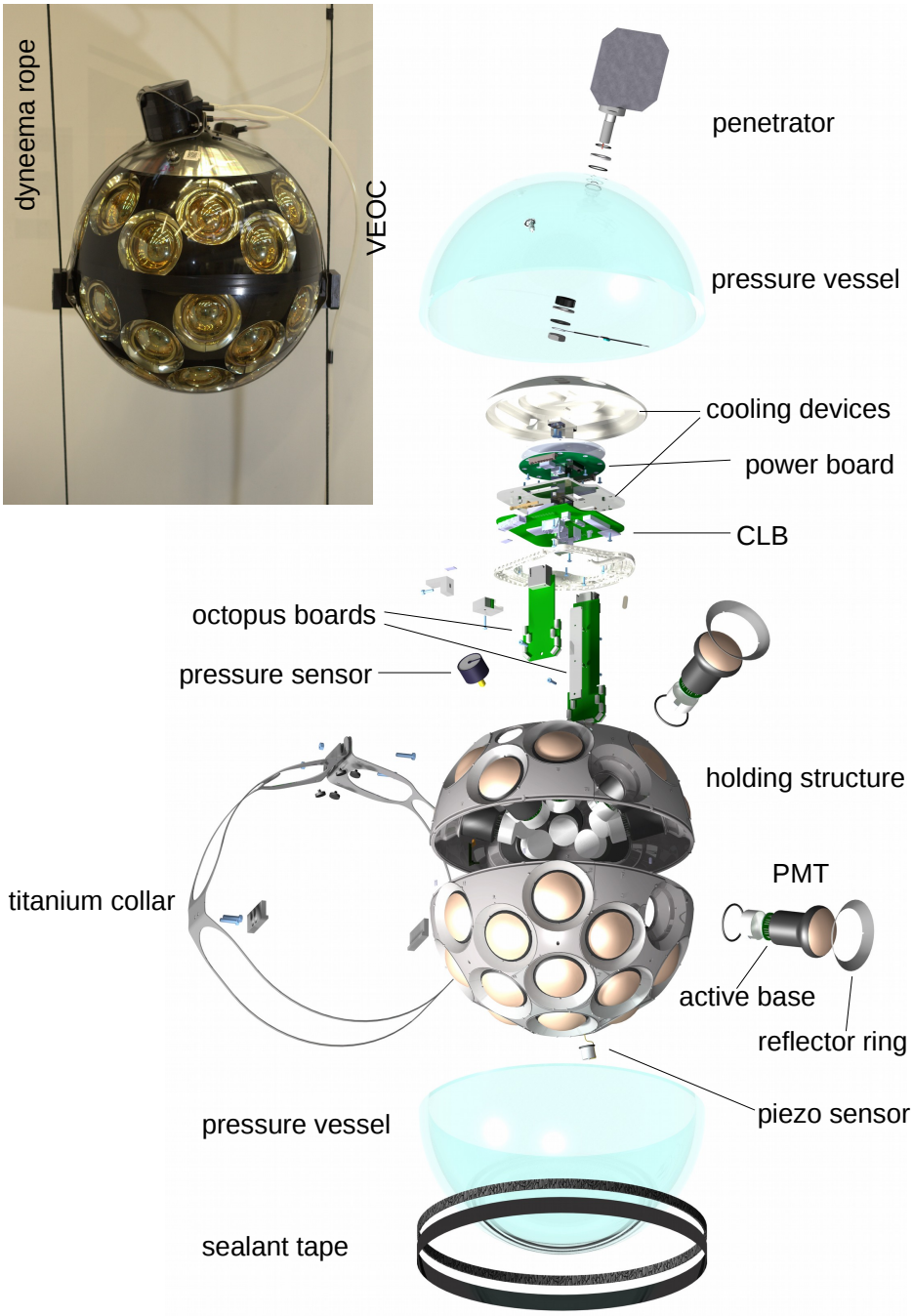

Figure 5.1: *Photograph and blow-up view of a KM3NeT digital optical module. The main components are indicated by name. Figure modified from [37].*

Chapter 6

PMT characterisation

When the multi-PMT module idea was first introduced, the XP53B20 PMT model by Photonis was the initial candidate as optical sensor. The performance properties of this tube represented a benchmark for PMT candidates to be used in the KM3NeT project. These quality parameters were specified by the collaboration in the conceptual and technical design reports of KM3NeT [32,33]. After Photonis stopped their PMT production, Hamamatsu Photonics [44], ET Enterprises Limited [45], MELZ FEU [46] and HZC Photonics [47] released modified or newly developed 3-inch PMTs to satisfy the requirements stated by the KM3NeT collaboration. Figure 6.1 shows the models from the different manufacturers currently being considered PMT candidates for the KM3NeT detector.

6.1 PMT specifications for KM3NeT

The track and shower reconstructions in KM3NeT are based on the detection of single photons. Increasing the number of measured photoelectrons improves the overall sensitivity of the detector and introduces a first quality criterion, the quantum efficiency. Being cost-effective but still delivering a decent quantum efficiency, standard bialkali photocathode materials have been chosen for all PMT candidates. Another crucial parameter for event reconstruction is the time measurement of the registered photon hits which is limited by the transit time spread of the PMTs. In order to minimise the effect of different photoelectron path lengths from the photocathode to the first dynode, 3-inch PMTs with spherical input windows were first introduced by Hamamatsu with the R12133 model and later on by the other manufacturers. Keeping spurious pulses, falsifying the measured signatures of events necessitates the introduction of upper limits on dark rate, pre-pulsing, delayed pulsing and afterpulsing. An upper limit of the supply voltage providing a specified gain insures a stable operation and a long lifetime whereas a lower limit guarantees a good collection efficiency between the photocathode and the first dynode. All quality parameters and their quantities are summarised in Table 6.1.

6.2 Characterisation of critical properties

When first promising PMT candidates for the KM3NeT DOM became available, a characterisation campaign was started by groups in Amsterdam (Nikhef), Catania (INFN) and Erlangen (ECAP). Dedicated setups were developed in order to determine if the performance of the novel prototype

Figure 6.1: *Photographs of PMT candidates for KM3NeT. From top left to bottom right: Hamamatsu R12199-02, HZC XP82B20, MELZ FEU, ETL D783KFLA, ETL D792KFLA.*

parameter	**value**
quantum efficiency (404 nm)	$\geqslant$ 23%
quantum efficiency (470 nm)	$\geqslant$ 18%
supply voltage	900 – 1400 V
transit time spread (FWHM)	$<$ 5 ns
dark rate (at 20 °C)	$<$ 2 kHz
pre pulsing	$<$ 1%
delayed pulsing	$<$ 3.5%
afterpulsing	$<$ 10%

Table 6.1: *Summary of the critical PMT parameters and the required values.*

tubes meets the requirements. Furthermore, detailed feedback was given to the manufacturers to stimulate further improvement of existing tubes as well as the development of new models. A description of the measurement techniques and setups used as well as the results of the mass tests in Erlangen are introduced in this section. The workload of the characterisation of more than 200 PMTs in total was split between the members of the KM3NeT hardware group in Erlangen. Main contributions were made by the author, L. Classen, O. Kalekin and student assistants.

6.2.1 Efficiency

The quantum efficiency (QE) measurements of the PMTs were performed in current mode without amplification. That means that the dynode system and the anode were electrically connected to the input of a picoampere meter. The negative potential applied to the photocathode was roughly equivalent to a representative potential difference between the photocathode and the first dynode in amplification mode. As the quantum efficiency is highly wavelength-dependent (see Section 4.2), a broad spectrum xenon lamp in combination with a monochromator was used for a spectral scan. Covering the whole responsive range of standard bialkali photocathodes, the quantum efficiency was measured for wavelengths λ between 280 and 700 nm. With < 2 nm, the width of each wavelength segment was well below the step size of 5 nm. The monochromator and the picoampere meter were remotely controllable by a PC allowing for an automated measurement process. Figure 6.2 shows a schematic of the quantum efficiency measurement setup. Since in former calibration measurements the long term variation of the intensity output of the light source had been found to be of the order of 1%, the current measurements of the PMT, I_{PMT}, and the reference photodiode, I_{PHD}, were performed in quick succession. With the wavelength-dependent quantum efficiency of the photodiode, QE_{PHD}, being well-known due to calibration by the manufacturer, the spectral quantum efficiency can be calculated using

$$\text{QE}_{\text{PMT}}(\lambda) = \frac{I_{\text{PMT}}(\lambda) - I_{\text{dark, PMT}}}{I_{\text{PHD}}(\lambda) - I_{\text{dark, PHD}}} \cdot \text{QE}_{\text{PHD}}(\lambda)\,, \tag{6.1}$$

where $I_{\text{dark, PMT}}$ and $I_{\text{dark, PHD}}$ are the measured dark currents of the PMT and photodiode respectively. The dark currents are monitored before and after the scan and tend to be rather constant on the time scale of a scan duration. Figure 6.3 shows the results of the quantum efficiency scans of all tested PMTs.

In earlier studies, the QE measurement setup was found to produce significant amounts of parasitic stray light. Colour filters for different wavelength bands were used in order to suppress the effect of the stray light. After the main source of stray light, light leaks in the dark box had been found, the colour filters were no longer necessary and were not used in most parts of the mass QE measurements. The remaining stray light caused by the grating in the monochromator used to split up the spectrum of the xenon lamp is unavoidable. It was found to have a systematic effect below 0.5 percent points and has thus a negligible influence on the QE measurement.

In a dedicated study, the detection efficiency DE in pulse mode of a smaller sample size of Hamamatsu-R12199 PMTs was investigated [48]. With relation to the quantum efficiency QE

$$\text{DE} = \text{QE} \cdot \text{CE}\,, \tag{6.2}$$

the collection efficiency could be calculated. A mean value of approximately 90% was found.

6.2.2 Gain

The gain measurements of the KM3NeT PMT candidates were carried out in pulse mode. The tested PMTs were located in a light-tight environment featuring close to light-tight cable inlets necessary for the measurement. These were the supply voltage and signal cables of the PMT as well as a light-guiding optical fibre for the photons from a pulse-driven LED. By putting a diffuser right behind the optical fibre at roughly 1 m distance to the PMT, the whole photocathode area of the PMT was illuminated with close to parallel light. The optical fibre was fed with short (800 ps) photon

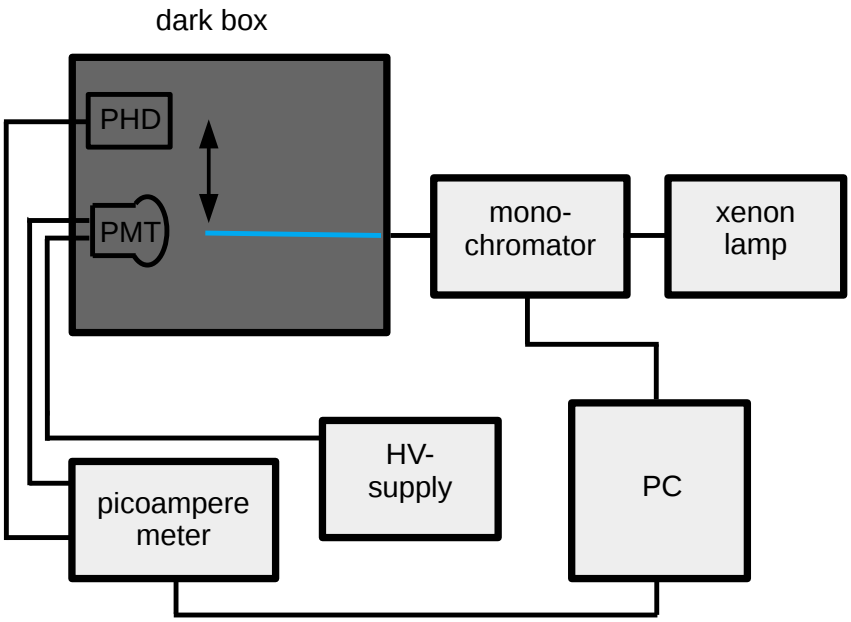

Figure 6.2: *Schematic of the QE measurement setup. The spectral scans were performed consecutively, one with the PMT positioned in front of the light beam and the other one with the reference photodiode in front of the light beam.*

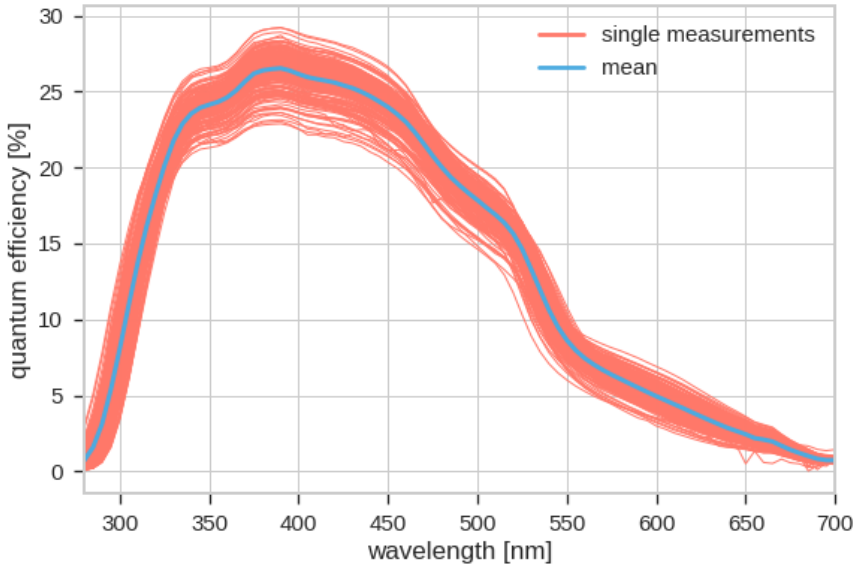

Figure 6.3: *Spectral quantum efficiency of all tested Hamamatsu R12199-02 PMTs.*

pulses from an LED with a peak wavelength[1] of 470 nm driven by a function-generator-triggered PicoQuant PDL 800 B Picosecond pulsed LED driver. The anode of the PMT was connected to an oscilloscope with 50 Ω input resistance, while the function generator was used as an external trigger. The high-voltage polarity was negative. A schematic of the described setup is shown in Figure 6.4.

A pulse frequency of 1 kHz was chosen to prevent the accidental measurement of afterpulses in the next triggered time window but still providing enough statistics per acquisition time. Each triggered signal (waveform) at the oscilloscope was stored on a disk to be analysed afterwards. The waveforms could then be integrated[2] to fill a histogram with the resulting charge. In order to get access to the single photoelectron peak (see Section 4.4), the amplitude of the LED driver was adjusted so that the PMT would yield, in average, approximately 0.1 photo electrons per pulse. The charge spectrum was then fitted by a PMT response function, which is a convolution of the Poisson-distributed multiplicity of the number of photoelectrons and the Gaussian distributions of the charge of the different multiplicities, in order to determine the charge of the pedestal and single photoelectron distribution (see [42] for details). Free parameters are: the mean number of photoelectrons; the mean charge and sigma of the single photoelectron peak; and a parameter representing the number of entries in the histogram. The mean value and sigma of the pedestal was determined by an independent Gaussian fit and fixed during the fit of the PMT response function. An example of a fitted charge histogram is shown in Figure 6.5. The gain G could then be calculated via

$$G = \frac{Q_{\text{spe}} - Q_{\text{ped}}}{e}, \tag{6.3}$$

where e is the elementary charge and Q_{spe} and Q_{ped} are the mean charges of the pedestal and single photoelectron distribution, respectively. This procedure was performed several times in a ±100 V range of the manufacturer-provided nominal high voltage for a gain of 3×10^6. On a logarithmic scale, a linear relation between gain and supply voltage is expected and is called gain slope (see Figure 6.5) by means of which the actual high voltage for a gain of 3×10^6 can be calculated.

6.2.3 Transit time spread

The transit time spread (TTS) is, as shown in Section 4.7, a measure of the time resolution of a PMT. It was measured using the setup shown in Figure 6.4. In this scenario it is important to point out that the whole photocathode area was illuminated by sub-nanosecond (800 ps) light pulses during the measurement since the main deviations of the transit times are expected to originate in different locations of photoelectron production on the photocathode. The transit time of a single photoelectron signal was defined as the time between the trigger and the crossing of a voltage threshold corresponding to 0.3 photoelectrons[3]. The distribution of the gathered transit times of photon hits uniformly distributed across the whole photocathode features a main peak. The standard deviation σ of a Gaussian fit applied to the main peak was converted to the TTS (FWHM):

$$\text{TTS} = 2 \cdot \sqrt{2 \cdot \ln 2} \cdot \sigma\,. \tag{6.4}$$

[1] The chosen wavelength represents the maximum in the expected flux in the deep sea which is a convolution of the Cherenkov spectrum and the local water transparency.

[2] The voltage drop at the input impedance of the oscilloscope is caused by the current from the anode of the PMT. By integrating this current over time, the charge of the PMT signal can be calculated.

[3] The relation between charge and voltage threshold was determined in a dedicated measurement.

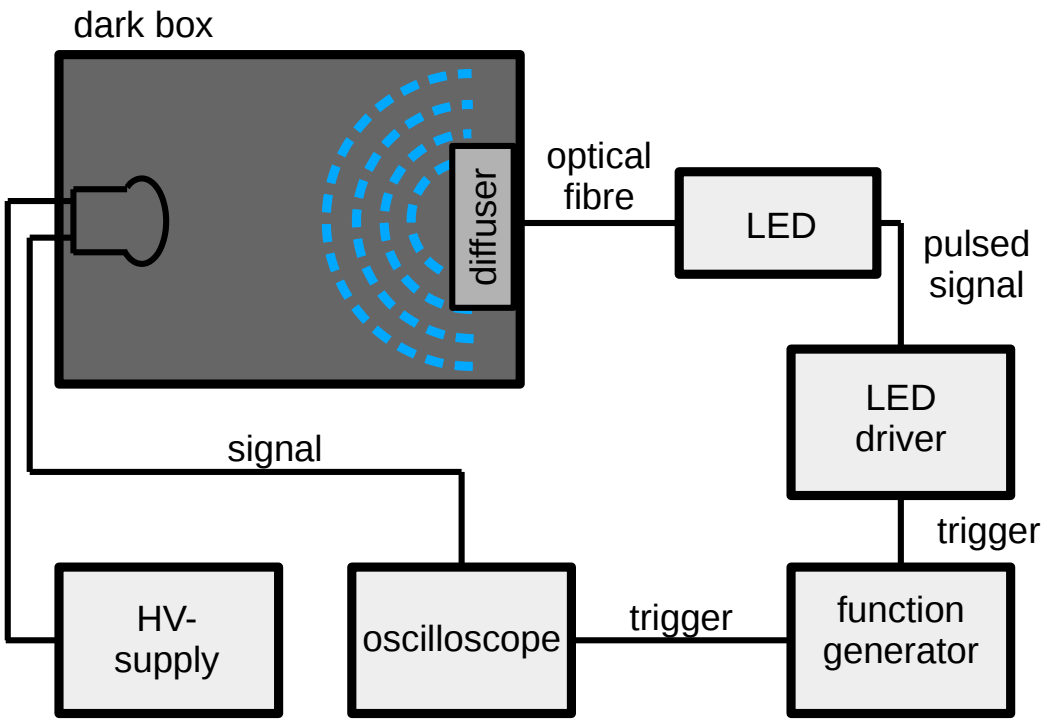

Figure 6.4: *Schematic of the pulse-mode measurement setup.*

Figure 6.6 shows a typical transit time distribution of a Hamamatsu-R12199 tube. In addition to the main peak it features pre-pulses and delayed pulses (see Section 4.8).

Afterwards, the measured TTS values were corrected for the light-source pulse width T_{pulse}:

$$\text{TTS}_{\text{PMT}} = \sqrt{\text{TTS}^2 - T_{\text{pulse}}^2}\,. \tag{6.5}$$

As stated in [33], the chromatic dispersion of light in water represents an intrinsic limit on the time resolution of an underwater neutrino telescope and amounts to 2 ns (σ) for a light-travelling distance of 50 m. The TTS of the PMTs is thus required to be $\sigma < 2$ ns, which corresponds to an FWHM of < 4.7 ns. The measurement results are shown in Section 6.3.

6.2.4 Correlated background probability

It is possible that the transit time of a PMT pulse lies outside of the usual time window, see Section 4.8. The probabilities of pre- and delayed pulses were determined using the measurement setup shown in Figure 6.4. The transit times were identified as described in Section 6.2.3. The number of pulses in the corresponding time windows in Figure 6.6 was counted and divided by the total number of pulses. In order to measure the afterpulse probability, waveforms were recorded within

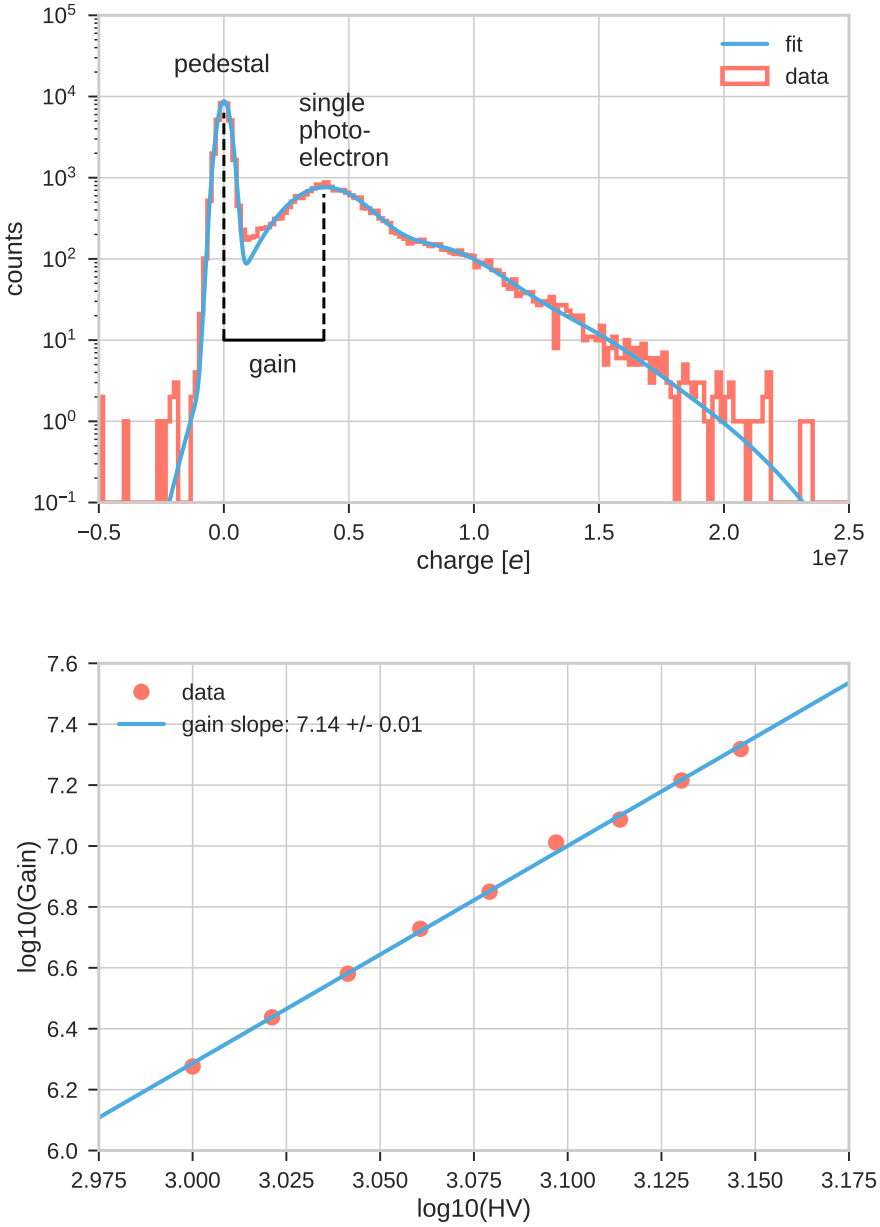

Figure 6.5: *Charge histogram for the determination of the gain for a certain HV (top) and gain slope fit of different gain measurements with different HVs (bottom).*

a bigger time window of 5 μs. If a main pulse was detected and its charge was found to be below 1.7 photoelectrons, afterpulses were counted in a time window starting 100 ns after the initial pulse to avoid a contamination with delayed pulses. The afterpulse probability could then be calculated by dividing the number of afterpulses found by the number of main pulses with a charge below 1.7 photoelectrons.

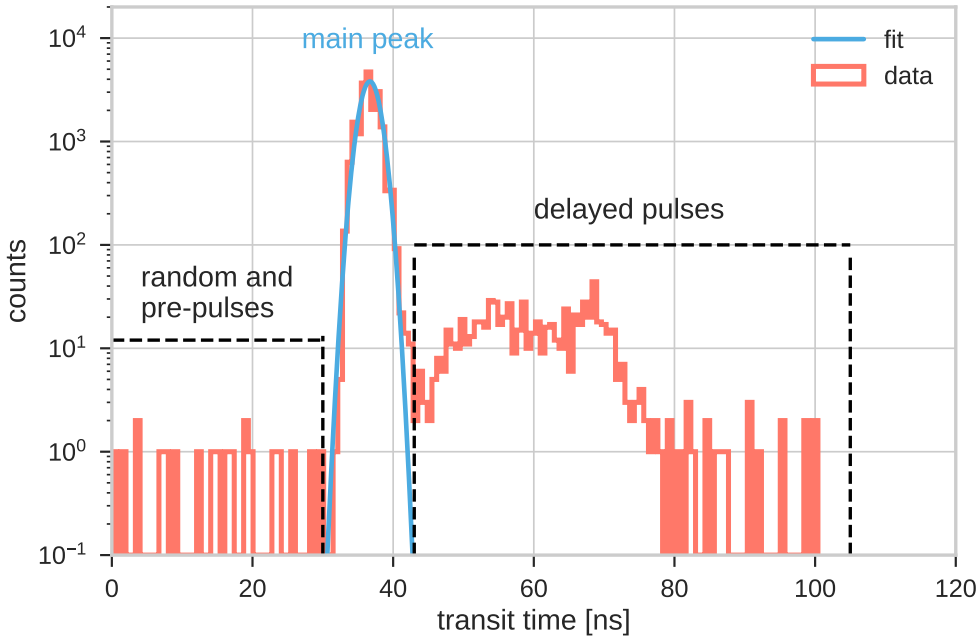

Figure 6.6: *Typical transit time distribution of a Hamamatsu-R12199 PMT. The plot features the transit times and a Gaussian fit to the main peak. The sigma here is roughly 1.3 ns and meets the requirement of < 2 ns. Pre-pulses and delayed pulses are indicated.*

6.2.5 Dark rate

As described in Section 4.9, the dark rate comprises all non-photon induced signals in a PMT in pulse mode. For the mass measurements of the dark rate, the PMTs were placed in a dark box for at least 12 hours with negative high voltage corresponding to a gain of 3×10^6 applied. The measurements were carried out at room temperature ($\approx 20°$C); humidity was not monitored. Using a discriminator, a NIM signal was produced each time a dark-rate induced PMT signal exceeded a threshold corresponding to 0.3 photoelectrons. After the conversion into a TTL pulse, the dark rate was determined by dividing the number of pulses registered by a counter by the corresponding time interval (usually 100 s, measured with a hand-held stopwatch). Since the dark box is not completely light-tight, the measured dark rate might be overestimated but holds as an upper limit.

6.3 Evaluation of the tested PMT models

In total, 203 Hamamatsu R12199-02 PMTs were tested by different groups of the KM3NeT collaboration in Amsterdam, Catania and Erlangen. Table 6.2 shows the results of the characterisation of the critical parameters. The table contains minimum, maximum and mean of the measured values as well as the specified values. Figure 6.7 shows distributions of the different measured values of a sample of the first 1500 Hamamatsu R12199-02 PMTs delivered. The results show that the vast majority of the tested tubes fulfil the specifications.

- All but one PMT meet the **quantum efficiency** specifications and the mean values at 390 and 470 nm are 26.5% and 21.6%, well above the respective specifications.
- Concerning the **high voltage** at a gain of 3×10^6 only two PMTs have measured voltages of below 900 V and 5 have voltages above 1400 V. The mean value is 1181 V, which is within the specified range of 900 - 1400 V.
- With a mean measured **transit time spread** (FWHM) of 3.9 ns and none of the PMTs exceeding the upper limit of 5 ns, the timing of the Hamamatsu R12199 PMTs totally complies with the specifications.
- The **dark rates** of 19 of the measured tubes exceed the specified limit of 2 kHz. Some of the PMTs with too large dark rate have been measured again after a much longer time in the darkroom and have finally been found to meet the specification. With a mean value of only 0.9 kHz the dark rate requirement of the PMTs is, on average, well met.
- All tubes have a **pre-pulse probability** of well below the specified value of 1% and with a mean value of 0.11% they fulfil the criterion very well.
- With 57 PMTs having a **delayed pulse probability** above the specified value of 3.5% it is a delicate parameter but with the mean value of 3.3% lying below the specified value the PMT model still shows a reasonable performance in this respect.
- The **afterpulse probability**, in contrast, meets the requirements very well with only one tube exceeding the limit of 10% and a mean value of 6.3% well below the specified value.

parameter	minimum	maximum	mean	specified value
quantum efficiency (390 nm)	22.9%	29.2%	26.5%	$\geqslant$ 23%
quantum efficiency (470 nm)	18.2%	23.5%	21.6%	$\geqslant$ 18%
nominal high voltage	875 V	1440 V	1181 V	900 - 1400 V
transit time spread (FWHM)	2.8 ns	4.7 ns	3.9 ns	$<$ 5 ns
dark rate	0.1 kHz	4.5 kHz	0.9 kHz	$<$ 2 kHz
pre-pulsing	0.01%	0.76%	0.11%	$<$ 1%
delayed pulsing	2.2%	6.1%	3.3%	$<$ 3.5%
afterpulsing	1.5%	13.1%	6.3%	$<$ 10%

Table 6.2: *Summary of the parameters measured on 203 Hamamatsu R12199-02 PMTs.*

In addition to the Hamamatsu R12199 PMT, different models from the manufacturers ET Enterprises Ltd. (ETL), MELZ FEU and HZC have been tested for their suitability as photodetectors for the KM3NeT project. The ETL type D783KFLA model shows overall compliance with the KM3NeT specifications and was used in the prototypes PPM-DOM [35] and PPM-DU [36] (in two

of the three DOMs). In context of the ^{40}K analysis with the PPM-DU, a significantly smaller overall efficiency of the DOMs equipped with the ETL D783KFLA PMTs compared to the DOM equipped with Hamamatsu R12199 PMTs was found (see Chapter 12). The comparatively high cost of the ETL D783KFLA model is due to a lens which is mounted in front of the photocathode. It has an outer curvature matching the inner curvature of the glass spheres in order to reduce the amount of optical gel needed to fill the cavity between the PMTs and the glass sphere. Later on, models with spherical input window (similar to the Hamamatsu R12199 type) were presented. The D793KFLA, D792KFLA and D9320KFL models with diameters of 77 mm, 86 mm and 90 mm respectively were tested and found to meet the specifications.

While the previously tested PMT model from the MELZ FEU manufacturer for the KM3NeT project did not fulfil the requirements, a modified version is currently in the process of characterisation. The latest version (XP82B20) of the manufacturer HZC does meet the specifications and is thus a promising candidate for the KM3NeT photodetectors.

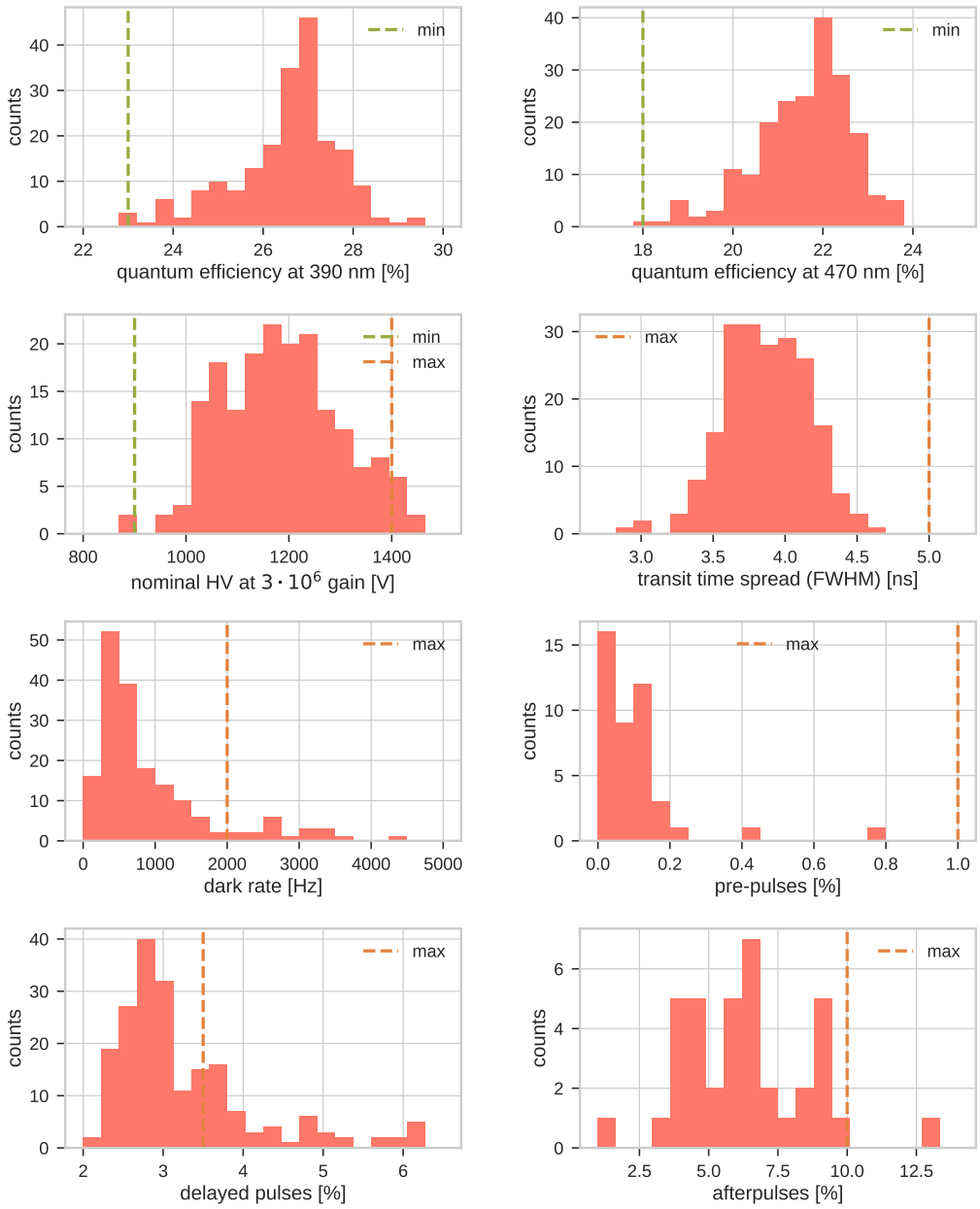

Figure 6.7: *Distributions of the measured PMT parameters. From top left to bottom right: quantum efficiency at 390 nm; quantum efficiency at 470 nm; nominal high voltage at a gain of 3×10^6 in V; FWHM of the transit time spread; dark rate; pre-pulse probability; delayed pulse probability; afterpulse probability. Specified values are indicated by green and orange dashed lines.*

Chapter 7

Passive optical components

In this chapter investigations of passive optical components are discussed. These are the glass sphere, the optical gel and the reflector rings mentioned in Chapter 5. In particular, the transmittance of the glass and gel as well as the reflectivity of the reflector material are covered and compared to the spectral quantum efficiency of the PMTs and the expected signal spectrum at the DOM[1].

7.1 Glass and gel transmittance

In addition to shielding the internal components from the pressure in the deep sea, the glass sphere pressure vessels should provide adequate transmittance in the relevant wavelength regime. The glass sphere chosen for the KM3NeT project consists of standard borosilicate glass called *Vitrovex* from *Nautilus GmbH* and is mass-producible at relatively low cost. This type of glass is also used in existing underwater neutrino telescopes and has been proven to resist the pressure over a long time fulfilling the requirements of transmittance. The *Wacker 612* gel is a two-component silicon gel where both parts are liquid, solidifying after compounding. The transmittances of the gel, the glass sphere and the glass tube of the PMTs are expected to have a cut-off at around 300 nm[2]. A modification of the spectral quantum efficiency test bench, introduced in Section 6.2.1, was used to perform the transmittance measurements of the glass and gel and for the reflectivity scans of the reflector materials shown in the following section. A xenon lamp with good coverage in the relevant wavelength range was used as light source. A monochromator selected a small wavelength band which is detected by a photodiode. A schematic of the setup is shown in Figure 7.1. The current measured by a picoampere meter with the light passing through a sample (glass sphere or gel) I_{sample} and the measured current without sample (as a reference) I_{ref} are used to calculate the transmittance T via

$$T(\lambda) = \frac{I_{\text{sample}}(\lambda)}{I_{\text{ref}}(\lambda)} \,. \tag{7.1}$$

Ten different spheres were measured, randomly chosen from one batch. The wall thickness of the glass vessels is 1.5 cm. The results are shown in Figure 7.2 in the context of the convolution of the Cherenkov spectrum and the water transparency for a path length of the photons of 100 m. The cut-off for all spheres varies by roughly 5 nm. This indicates a very stable manufacturing process and

[1] The signal spectrum is a convolution of the Cherenkov spectrum and the transmittance of sea water.

[2] The PMT tube also consists of borosilicate glass but the cut-off in transmittance should be slightly shifted to lower wavelengths due to its lower thickness.

material composition. The transmittance is very stable at roughly 90% between 350 and 700 nm. In the region of the cut-off, between 300 and 350 nm, the contribution to the photon spectrum is below 10%. The transmittance of a 1 cm thick gel sample is also shown in Figure 7.2. Similar to the glass spheres, the transmittance of the gel sample is roughly 90% in the relevant wavelength band. The angle of incidence of the light passing through the glass and gel was roughly 90°.

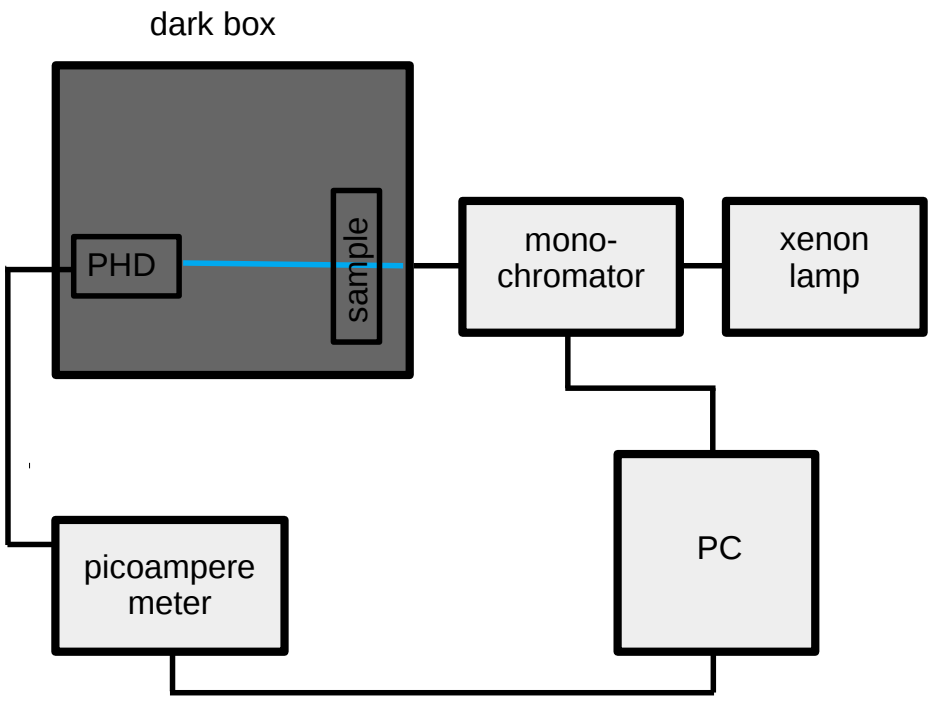

Figure 7.1: *Schematic of the transmittance measurement setup. The spectral scans were performed with and without samples between the monochromator and the photodiode.*

7.2 Reflector materials

The main purpose of using reflector rings is to benefit from spare space close to the surface of the DOM, by collecting photons which would otherwise be absorbed by the PMT holding structure. As shown in Chapter 7.3, using reflector rings increases the sensitivity of a PMT for photons with angles of incidence smaller than 90° and decreases it for photons with angles of incidence larger than 90°, where the support structure would absorb most of them anyway. The first idea of benefiting from the concept of reflector rings by using aluminium-coated acrylic glass was sorted out quickly after it had been realised that, at a wavelength of roughly 400 nm, the reflectivity was cut off to smaller wavelengths. This cut-off was partly originating from the transmittance of the acrylic glass and the use of generic aluminium as reflective material. By adding e.g. a silver layer to the reflecting surface, a higher overall reflectivity can be achieved and the cut-off can be shifted to shorter wavelengths.

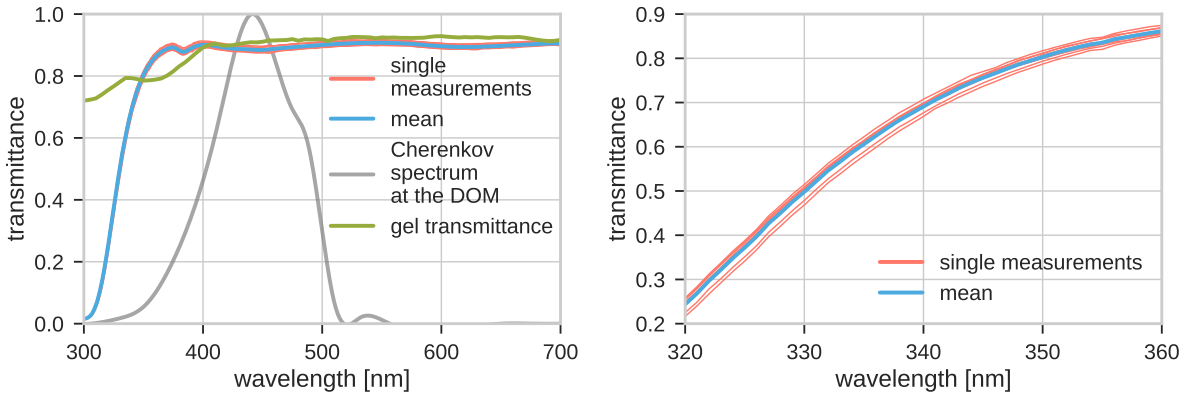

Figure 7.2: *Measured transmittance of a sample of ten different half spheres from one batch as well as the transmittance of a 1 cm thick gel sample. A comparison with a cubic spline interpolation of the convolution of the Cherenkov spectrum and the water transparency for a path length of 100 m (left) and a zoom in the cut-off range (right).*

Similar to the transmittance, the reflectivity was measured with a modified version of the quantum efficiency test setup of Section 6.2.1. A sample of reflection material was positioned in a 45° angle with respect to the angle of incidence of the photon beam, and the photodiode was set at the same emergent angle. A spectral scan was performed and the current I_{sample} was monitored and divided by the current of a reference measurement I_{ref}, where the photons were directly measured by the photodiode. The reflectivity R could then be calculated:

$$R(\lambda) = \frac{I_{\text{sample}}(\lambda)}{I_{\text{ref}}(\lambda)}\,. \tag{7.2}$$

Figure 7.3 shows the modified test setup as well as a sketch of a PMT and reflector ring in the support structure of a DOM. Reflector material samples from various manufacturers were ordered to probe their reflectivity. An important advantage of these materials is that they consist of coated metal plates. They can be laser cut and bent to conical shape so that they can be directly inserted into the support structure. Figure 7.4 shows the spectral reflectivity of different material samples compared to the expected Cherenkov spectrum at the DOM, the glass sphere transmittance and the transmittance of a 1 cm thick gel sample. With a peak reflectivity of roughly 0.8 and a cut-off at 400 nm, the aluminium-coated acrylic glass (PMMA) performs worst. The *ALMECOV95100* reflector material performed best in the measurement with a cut-off at roughly 330 nm and a peak reflectivity well above 0.9 and was thus used as standard reflector material for the DOM integration.

7.3 Angular acceptance

In the scope of this work, the angular acceptance is measured as response to illumination of the full photocathode area with parallel photons. The impact of the support structure and the reflector rings on the angular acceptance of the PMTs is investigated in this section. In addition, the measured angular acceptance is a valuable input for detector simulations investigating the influence of different configurations on the detector sensitivity.

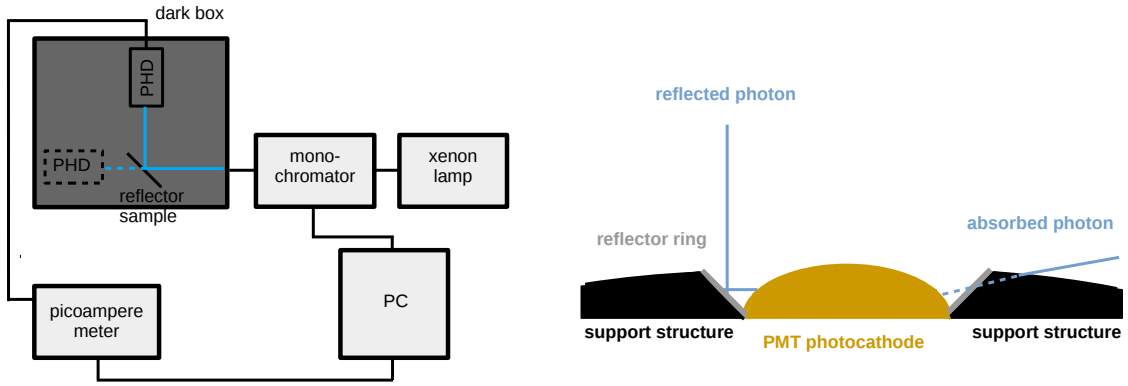

Figure 7.3: *Test setup used to determine the reflectivity of different reflector materials (left); each measurement with sample is followed by a reference measurement with direct illumination of the photodiode. Sketch of a PMT and reflector ring embedded in the support structure of a DOM (right). While a part of the photons with large angles of incidence gets absorbed, more photons with small angles of incidence can reach the PMT due to reflection at the reflector ring.*

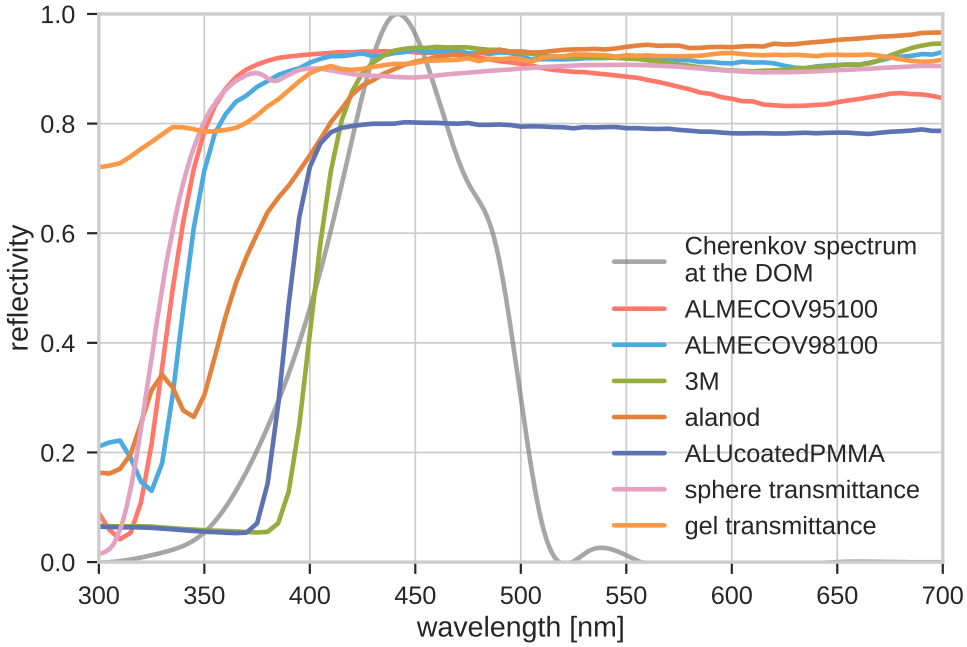

Figure 7.4: *Measured reflectivities of different material samples as candidates for the reflector rings. The Cherenkov spectrum at the DOM, sphere transmittance and the transmittance of a 1 cm thick gel sample are also shown.*

There are two obvious ways of measuring the effective area of a PMT. The measurement can be

performed in pulse mode, where the signal pulses of the PMT are measured with an oscilloscope as response to the light pulses from the light source, determining the mean charge of the resulting charge spectrum as a measure of the number of detected photons. This matches best the time-resolved data acquisition of a PMT in a DOM deployed in a KM3NeT detection unit. It was, however, shown by L. Classen in his PhD thesis [49] that a more simple approach delivers comparable results. Integrating the signal output of a PMT over time by measuring the current works equally well in regard to the determination of the relative acceptance. In addition, it is less time-consuming and was thus used for the determination of the angular acceptance.

A schematic of the test setup is shown in Figure 7.5. Planning and installation of the test setup were effected by the author in collaboration with L. Classen. A PMT was placed on a rotating table driven by a stepper motor that was remote-controllable by a PC using dedicated python software. A so-called optical encoder, independently counting the steps performed by the motor, allowed for a correction of missed steps, thus improving the reliability of the setup. The light source, a pulsed LED equipped with a diffuser, was mounted in an approximate distance of 3 m in order to provide parallel photons at the whole PMT photocathode[3]. The LED was driven by a function generator, allowing for tuning the pulse height and pulse frequency. As the absolute number of photons arriving at the PMT remains unknown in this setup, acceptances can only be determined relative to each other. For the three configurations:

- a bare PMT,
- a PMT embedded in a support structure cut-out, also referred to as holder,
- and a PMT embedded in a support structure cut-out and equipped with a reflector ring,

the measured currents were divided by the current obtained from frontal illumination of the bare PMT. The intensity of the LED was not changed in between or during the measurements. The angular scan was performed in steps of two degrees for all configurations in a range from -180 to 180° in case of the bare PMT and -110 to 110° in case of the PMT embedded in the support structure with and without a reflector ring. Since the support structure shields the PMT from direct photons with angles higher (lower) than approximately 110° (-110°), the acceptance in these ranges was expected to be zero. The results of the scans for the three configurations are shown in Figure 7.6. The spherical shape of the photocathode of the PMT enables the detection of photons with very large angles of incidence in the case of the bare PMT. The inevitable use of a support structure, however, cuts away these photons and limits the sensitive angle range to roughly $\pm 90^\circ$. In order to make up for the losses, a reflector ring is used. It increases the pointing, collecting only photons with an angle of incidence of up to 50°. The overall gains and losses of the effective area can be calculated by integrating over all angles of incidence

$$A = c \cdot \int_0^{2\pi} \int_0^{\pi} a(\varphi, \theta)\, \mathrm{d}\varphi\, \sin\theta\, \mathrm{d}\theta\,, \tag{7.3}$$

where A is a relative measure of the effective area, $a(\varphi, \theta)$ is a relative measure of the angular acceptance depending on the angle of incidence, and c is a normalisation factor. Since only a

[3] For this purpose the whole setup was installed in a darkroom instead of a dark box.

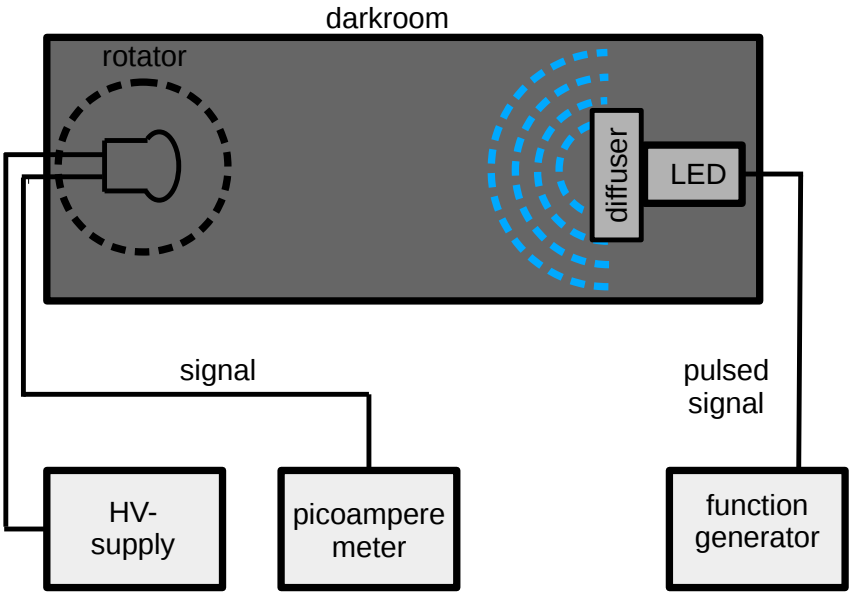

Figure 7.5: *Test setup for angular acceptance scans. A PMT is mounted at a rotating table in the far-field (3 m) of a diffuser-equipped, pulsed LED with a peak wavelength of 470 nm driven by a function generator. The current measured with a picoampere meter is a measure of the effective area, changing with the angle of incidence of the photons. The rotating table is driven by a stepper motor which is, together with the current monitoring, remote-controllable by a PC with dedicated python software.*

one-dimensional scan, here in the θ direction, was performed, rotational symmetry in φ is assumed, which leads to

$$A = c \cdot 2\pi \int_0^{\pi} a(\theta)\ \sin\theta \,\mathrm{d}\theta \tag{7.4}$$

and can be approximated for discrete values used in the measurement to

$$A = c \cdot 2\pi \sum_i a(\theta_i)\ \sin\theta_i\, \Delta\theta_i\,. \tag{7.5}$$

Ultimately, the ratio of the effective areas of a PMT equipped with a reflector A_{ring} and a bare PMT A_{bare} can be calculated, using their relative acceptance values $a_{\text{ring}}(\theta)$ and $a_{\text{bare}}(\theta)$, respectively and assuming equal angle step sizes $\Delta\theta$:

$$\frac{A_{\text{ring}}}{A_{\text{bare}}} = \frac{\sum_i a_{\text{ring}}(\theta_i)\ \sin\theta_i}{\sum_i a_{\text{bare}}(\theta_i)\ \sin\theta_i}\,. \tag{7.6}$$

Acceptance values for angles above 110 and below -110° in the cases of PMT with reflector ring and PMT in support structure are assumed to be zero and are thus neglected for this calculation.

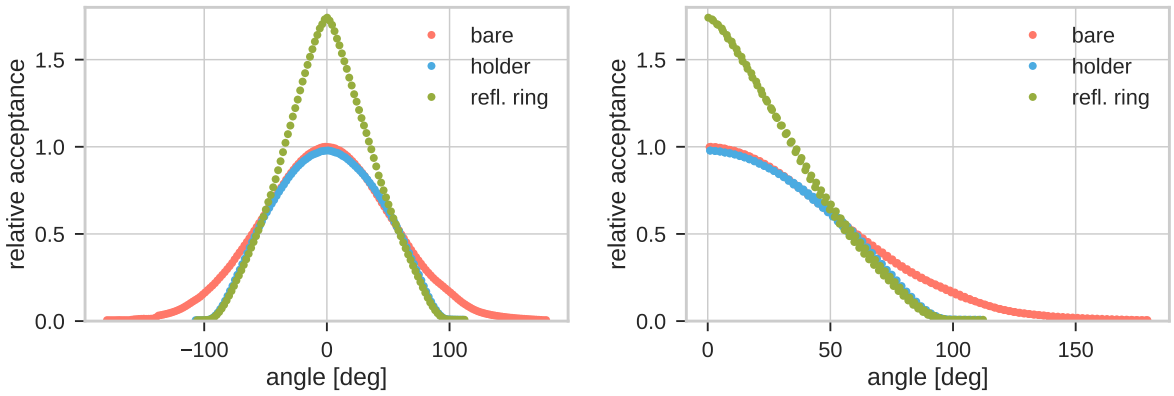

Figure 7.6: *Measured relative acceptance as a function of the angle of incidence of the parallel photons (left) and for absolute values of the angle (right). The bare PMT is shown in red, a PMT embedded in a support structure cut-out is shown in blue, and a reflector-equipped PMT is shown in green. All values are relative to the measured current of the bare PMT at an angle of incidence of* $0°$.

Ratios of effective areas are shown in Table 7.1. They were calculated separately for angles in positive and negative directions. Discrepancies can be explained by a distortion of the PMT position relative to the support structure and reflector ring.

In summary, it can be stated that with the support structure being inevitable, the reflector ring generates a yield in effective area of 17% and increases the directional sensitivity due to the acceptance increase for angles $< 50°$.

	$A_{\text{holder}}/A_{\text{bare}}$	$A_{\text{ring}}/A_{\text{holder}}$	$A_{\text{ring}}/A_{\text{bare}}$
positive angles	0.82	1.17	0.96
negative angles	0.78	1.17	0.91
mean	0.80	1.17	0.93

Table 7.1: *Effective area ratios for different PMT configurations measured. The inevitable use of a support structure reduces the effective area compared to the bare PMT; using a reflector ring increases the effective area again. The overall effective area using support structure and reflector ring is only a few percent below that of the bare PMT. Losses can be explained by the non-perfect reflectivity of the reflector material.*

Chapter 8

The KM3NeT active base

Following the multi-PMT concept of the KM3NeT digital optical module, each PMT is equipped with its own active base. Unlike resistive bases, that need an external high-voltage supply, the KM3NeT active bases provide the high voltage themselves using the Cockcroft-Walton principle described in Section 4.10. The tasks of the active bases in KM3NeT are:

- providing adjustable high voltage for all PMTs in order to match the nominal gain,
- amplifying and shaping the signal, and
- transforming the analogue signal to the time-over-threshold (ToT) signal with an adjustable threshold,

with low power consumption being advantageous. In this chapter, concept and functionality of the KM3NeT active base are introduced. In addition, the relation between the charge of the signal from the PMT and the resulting ToT produced by the base is determined. This allows the number of photons inducing a signal to be inferred from the ToT measurement.

8.1 Basic concept and functionality

The basic concept of the KM3NeT active base is to provide a PMT with high voltage to produce a gain of 3×10^6. In addition, the charge signal produced by a PMT as a result of a photon hit has to be transformed into a time-over-threshold (ToT) signal. Defining the so-called hit in KM3NeT to only consist of the start time, the ToT and the PMT identifier, allows for operating a huge detector with acceptable data flow. It is, however, important that each PMT-base pair produces the same ToT for a single photoelectron hit. This can be achieved by tuning the high voltage as well as the threshold of the comparator producing the ToT. Each active base has a very low overall power consumption of roughly 35 mW.

A schematic of the layout of an active base is shown in Figure 8.1. The functionality of the active base can be divided into two parts. The Cockcroft-Walton multiplier feedback control asic (CoCo) indicated by the green parts of Figure 8.1 is providing the high-voltage supply for the PMTs. A pulse generator produces a pulsed signal that is amplified using the Cockcroft-Walton technique (see Section 4.10) to a stable DC output voltage adjustable between 700 and 1500 V. The PROMiS chip indicated in dark blue in Figure 8.1 is in charge of the signal processing and ToT transformation.

The signal coming from the anode of the PMT is first preamplified by a charge-to-voltage converter. Using a comparator, the resulting signal is compared to a threshold which is adjustable between 0.8 and 2.4 V, producing the ToT signal. Low-voltage differential signalling (LVDS) provides low noise susceptibility of the ToT signal. For calibration purposes the positive and negative part of the differential preamplified analogue signal can also be accessed via an analogue buffer.

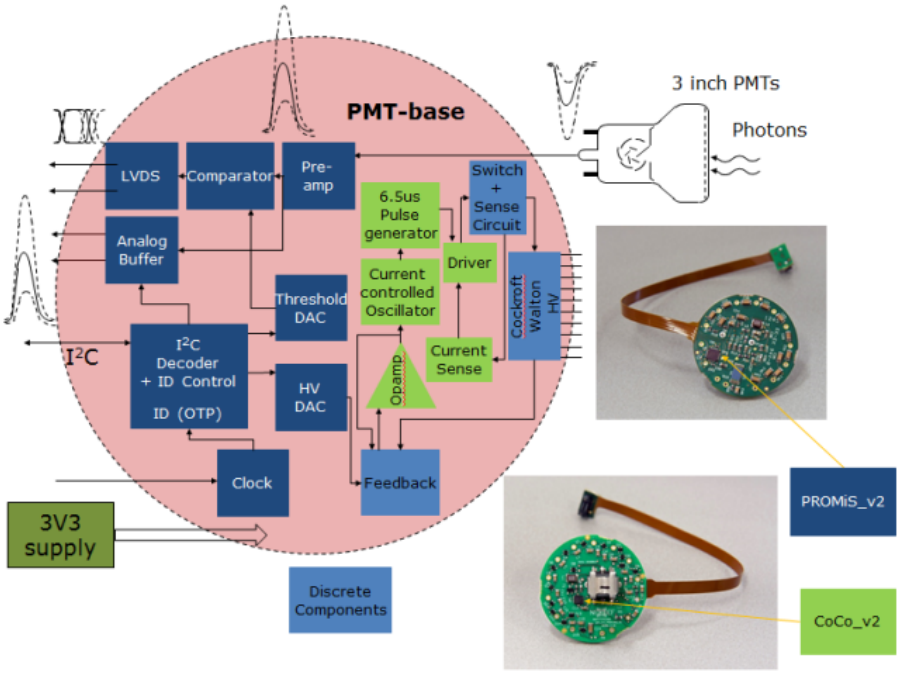

Figure 8.1: *Schematic of the KM3NeT active base. The supply voltage is 3.3 V DC.The parts indicated in green represent the high-voltage supply via the Cockcroft-Walton technique. Parts indicated in dark blue represent the signal processing via a preamplification and ToT conversion. Figure taken from [50].*

8.2 Charge ToT calibration

For easy access to the ToT and analogue signals from the LVDS and analogue buffer of the active base, a readout board was provided by the Nikhef group. It could be directly connected to an active base and had LEMO connectors for the data transmission to an oscilloscope as well as connectors for the supply voltage of 3.3 V. For a first ToT measurement, a PMT equipped with an active base connected to a readout board was placed in a dark box. The PMT was illuminated by an LED driven by a function generator with a pulsed signal of 20 ns width. The amplitude of the signal was adjusted so that the mean number of photoelectrons produced by the PMT as a response to a light pulse was of the order of 0.1. The ToT and analogue signals produced by the active base were measured with an oscilloscope, which was externally triggered by the function generator. The oscilloscope waveforms were stored on disk and analysed afterwards. Figure 8.2 shows the analogue and corresponding ToT signals of two single photoelectron hits as well as the ToT as a function of the maximum voltage of the analogue signal for all events in a certain data taking period. One of the hits

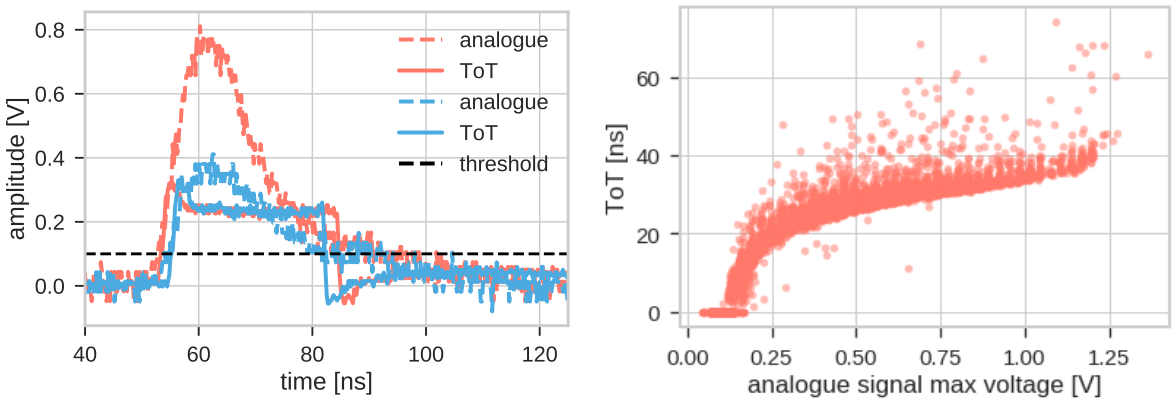

Figure 8.2: *Measured differential analogue and corresponding differential ToT signals from the oscilloscope (left). The threshold is indicated as black dashed line. ToT as a function of the maximum voltage for all events in one data taking period (right).*

producing roughly double the voltage compared to the other one[1] with the widths of the ToT signals being roughly the same contributes to the intrinsic uncertainty of the KM3NeT PMT-base-pair.

The actual charge-ToT calibration was realised with a slightly different approach. For different high voltages, and consequently different gains, single-photoelectron ToT spectra were recorded with the setup described above. The corresponding charges at the anode of the PMT (in units of the elementary charge) were equivalent to the gain since only single-photoelectron hits were considered. In the ToT spectrum, the single-photoelectron peak was identified and fitted with a Gaussian function. The gain was determined from the high voltage via a previously measured gain slope similar to that shown in Figure 6.5. An exemplary ToT spectrum with the Gaussian fit as well as the correlation between gain and the mean of the Gaussian fit of the ToTs for different high voltages for three different PMTs is shown in Figure 8.3 (a) and (b). Similar to Figure 8.2, right, a logarithmic-like relation can be identified for small gains up to $\approx 10^7$, which becomes linear for larger gains. This behaviour can be explained by the information given in Figure 8.3 (c). While the maximum amplitude of the analogue buffer signal increases linearly with the charge of the original PMT signal at small charges, an amplitude saturation is reached for larger charges. This saturation effect clearly causes the linear relation between gain and ToT displayed in Figure 8.3 (b). The preamplifier saturating at an input charge of roughly 5×10^6 electrons leads to a broadening of the output signal with a maximum amplitude of 1.3 V, where ultimately all excessive charge ΔQ linearly increases the ToT by:

$$\Delta t = \Delta Q \cdot \frac{R}{U}, \tag{8.1}$$

where $\frac{R}{U}$ is constant in the saturation regime. See the grey rectangle in Figure 8.3 (c) for illustration.

Since the above-described method for the charge-ToT calibration is limited by the high voltage, another approach is needed to extend the calibration to larger intensities. Therefore, instead of varying the charge by increasing the high voltage applied, the intensity of the light source was varied and thus the number of photoelectrons per pulse. A reference PMT equipped with a passive base was used to determine the mean number of photoelectrons per pulse, and a PMT equipped

[1] Since the preamplifier performs a charge-to-voltage conversion, the maximum amplitude of the analogue signal represents the charge of the original PMT anode signal.

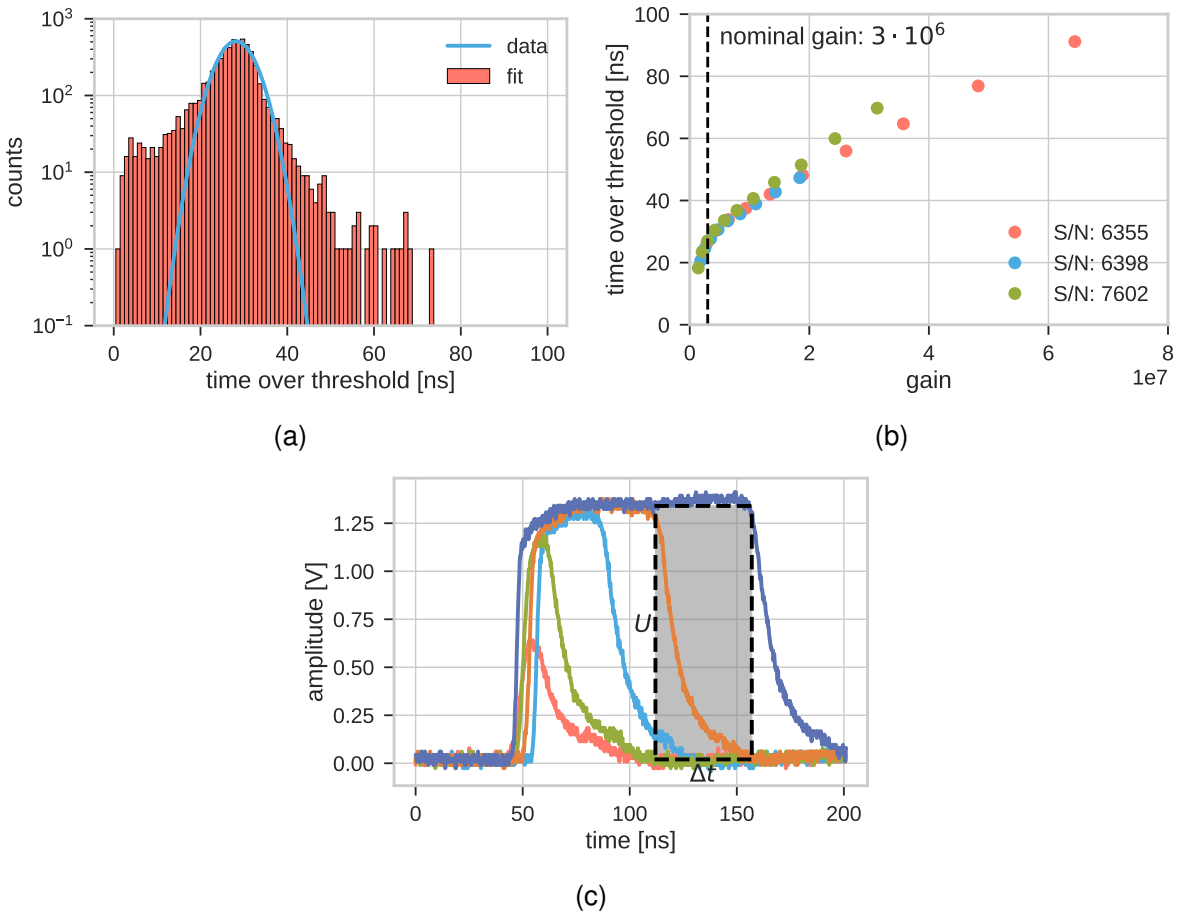

Figure 8.3: *Histogram of time over thresholds of all signals produced during a certain data taking period (a) and correlation between gain and ToT for different high voltages in the single-photoelectron regime for three different PMTs (b). Comparison of differential analogue buffer signals with different charges of the original PMT signal (c). Saturation starts at a charge of roughly 5×10^6 electrons. The difference in charge of two saturated signals (brown and dark blue curves in (c)) is described as a rectangle and the resulting difference in ToT is thus linearly related to it.*

with an active base was used to measure the ToT for each iteration. A factor compensating for the different efficiencies of both PMTs was determined by comparing the photoelectron yield of both PMTs in the single-photoelectron regime. The mean ToT measured by the PMT equipped with an active base was determined by a Gaussian fit as shown in Figure 8.3 (a), whereas the mean number of photoelectrons measured with the PMT equipped with a passive base was determined by a multi-Gaussian fit to the charge spectrum. In order to provide similar light intensities at both PMTs, they were placed in a darkroom next to each other in the far-field of a diffuser-equipped LED. The results of the calibration are shown in Figure 8.4. The linear behaviour continues up to a charge corresponding to roughly 30 photoelectrons. After this, another saturation can be identified.

To summarise the results of this section, it can be said that the relation between the charge produced by a PMT and the ToT produced by the active base in response to it was found to be well-defined. The information derived by the measurements described in this section contribute

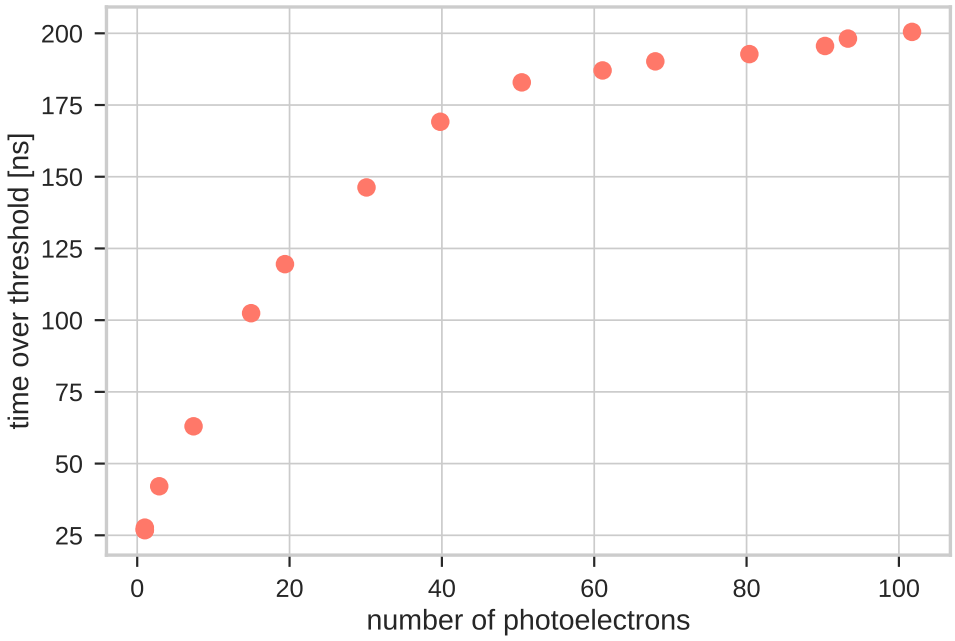

Figure 8.4: *Correlation between mean number of photoelectrons and ToT. ToT was measured by a PMT equipped with an active base, the number of photoelectrons was measured by a reference PMT equipped with a passive base. Differences in efficiencies were corrected by a factor determined by a comparison of the mean number of photoelectrons in the single-photoelectron regime.*

to the overall understanding of the detector response and represent valuable input for detector simulations as well as for the development of reconstruction algorithms. Using the individual ToT information as a measure of the charge or the number of photoelectrons enables increased accuracy in sophisticated reconstruction algorithms. The calibration shown in this section is limited to photons arriving in a small time window. In order to get information about successively arriving photons with larger time differences, a dedicated study has to be performed in the future.

Chapter 9

DOM acceptance scan

An angular acceptance measurement of a fully integrated KM3NeT DOM is presented in this chapter. Two angular scans, in azimuthal and zenithal direction, were performed using the KM3NeT DAQ system. The DOM was placed in a darkroom and its response to the far field of a pulsed laser was measured at different angles. The technical design of the test setup, the measurement procedure as well as the data analysis and a comparison to Monte Carlo simulations are presented in this chapter. Information derived from this measurement can be used to validate DOM simulations and constitutes valuable input for detector simulations.

9.1 Test setup and analysis methods

After the integration of the first DOM at ECAP was finished, a test setup for an angular acceptance measurement was designed by the author in collaboration with T. Gál and O. Kalekin. Figure 9.1 shows a schematic overview of the setup. The DOM was placed on a rotatable table in a darkroom in the far field (distance $\approx$ 3 m) of a light-guiding fibre equipped with a diffuser, providing parallel photons at the surface of the DOM. The fibre was fed with sub-nanosecond laser pulses with a frequency of 10 kHz. The spectral distribution can be approximated by a Gaussian with a mean wavelength of $\approx$ 460 nm and a width (FWHM) of $\approx$ 35 nm. Like an additional LED with a pulse width of 20 ns, the laser was driven by a function generator and thus had the same adjustable pulse frequency. A difference of roughly 100 ns between the arrival times of the photons from the laser and the LED at the DOM was adjusted using cable delay.

In order to measure the angular acceptance of a DOM, a stable photon flux at the DOM is needed. In addition, signal photon hits have to be distinguished from dark rate hits. While the dark rate hits are randomly distributed over time with a rate of the order of 1 kHz, the signal photons from the laser appear in a well-defined and very small time window. Accessing these signal photons, however, is the key to a successful angular acceptance measurement and was first tried by iterating over all hits in a timeslice and searching for tuples with a time difference matching the pulse frequency of the laser. This algorithm ended up being far too slow, and thus a more sophisticated method was developed. Utilising trigger algorithms already available in the KM3NeT DAQ framework, photons from the LED illuminating the back of the DOM were applied to trigger so-called events. When a set of hits meets the trigger condition (usually several hits in a short time window), an event is produced, snapshotting all hits in a certain time window before and after the triggered hits. The trigger condition was optimised in order to almost only trigger on photons from the LED.

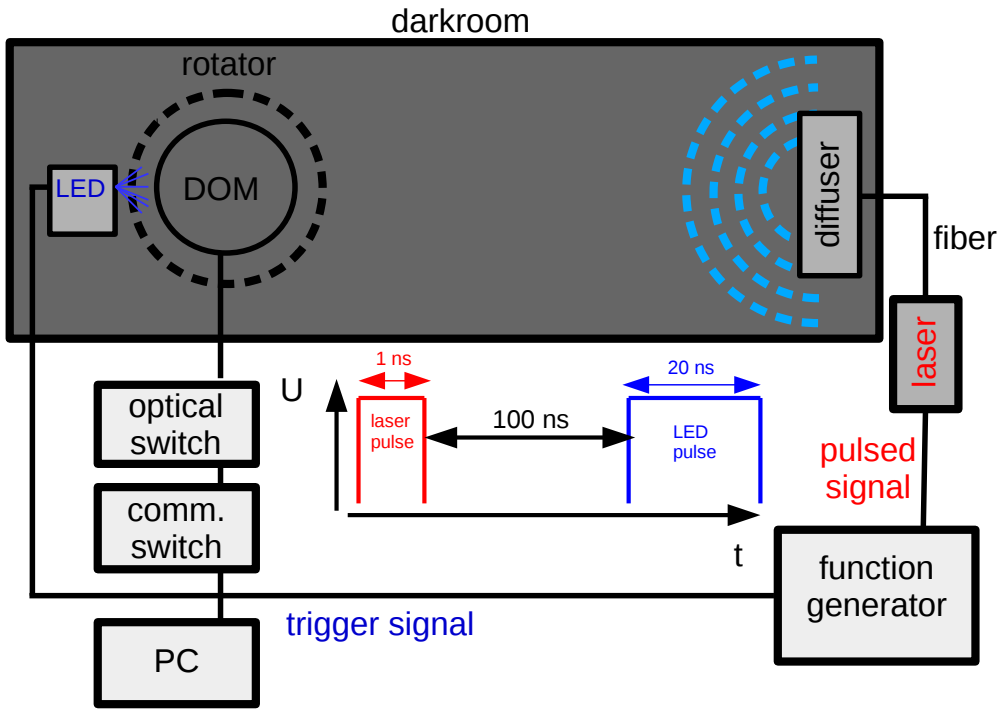

Figure 9.1: *Schematic overview of the test setup design for the angular acceptance measurement of a KM3NeT DOM.*

As the LED and laser pulses were synchronised in time, the photons from the laser were stored as snapshot hits in the events at a time of roughly 100 ns earlier[1] than the triggered LED hits. There were, however, also events produced with the LED switched off, but only with a frequency of the order of 1 Hz so that they were neglected compared to the trigger rate of light pulses of roughly 3 kHz.

The time distribution of hits in the 10000 recorded events used for the calculation of the angular acceptance for a certain angle is shown in Figure 9.2. The hits of two PMTs, one facing in the direction of the LED at the back of the DOM and the other one facing in the direction of the laser are shown. When hits caused by the LED meet the trigger condition, all hits in a time window of ±200 ns are stored. The laser hits appear at times between -100 ns and -50 ns in Figure 9.2. These hits are almost pure signal hits from the laser[2] and can be simply summed for each PMT to get a measure of their acceptance for the corresponding angle. As the photons in a laser pulse are Poisson distributed, the summed number of hits has to be corrected due to the fact that two or more photon hits are only counted once. By knowing the probability of a PMT not measuring photons of

[1] Placing the laser pulse shortly before and not after the LED trigger pulse reduces the effect of afterpulse interference.

[2] With a dark rate of 1 kHz, the probability of a random hit appearing in a time window of 50 ns is of the order of 10^{-5}.

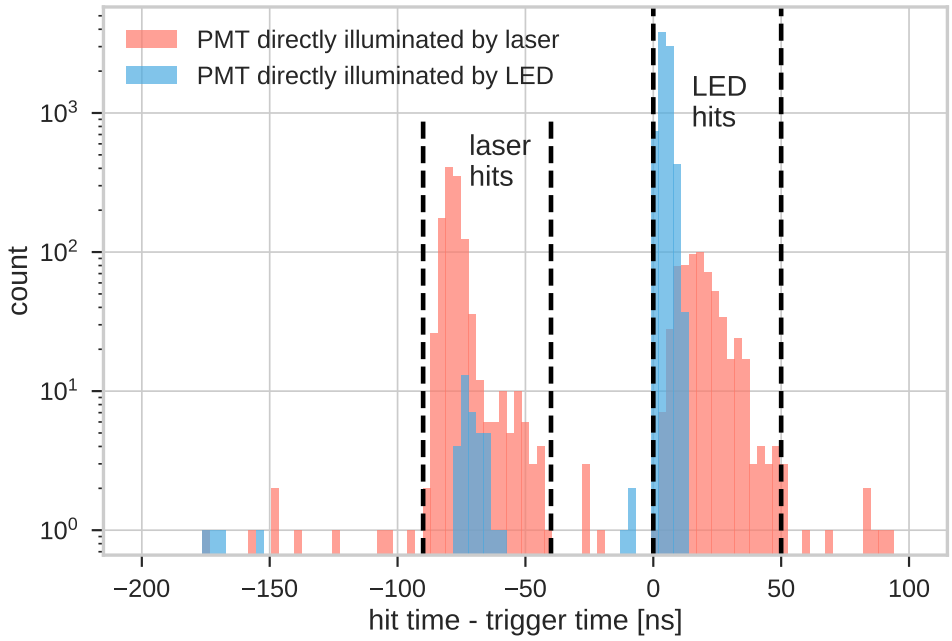

Figure 9.2: *Time distribution of hits in all events used for the angular acceptance calculation for a certain angle. Shown in red are hits from the PMT that was directly illuminated by the laser; shown in blue are hits from the PMT that was directly illuminated by the LED. The presence of hits of the PMTs facing away from the respective sources can be explained by multiple scattering in the glass sphere of the DOM.*

a pulse

$$1 - \frac{N_{\text{hits}}}{N_{\text{events}}} = P(0,\lambda) = \frac{\lambda^0}{0!} \cdot e^{-\lambda}, \tag{9.1}$$

the mean number of photoelectrons λ can be calculated:

$$\lambda = -\ln\left(1 - \frac{N_{\text{hits}}}{N_{\text{events}}}\right), \tag{9.2}$$

where N_{hits} is the number of measured hits from the laser pulses and N_{events} is the number of events triggered from hits of the LED pulses. The mean number of photoelectrons is calculated for every PMT and angle, resulting in a table of $31 \cdot 360$ values λ_{ij} where the index i stands for the 31 different PMTs and the index j for the 360 different scan angles.

9.2 Results and comparison of data and Monte Carlo simulation

With the setup described in the previous section, two acceptance scans were performed. One scan in azimuthal direction with the DOM being positioned upright at the rotating table (see Figure 9.3

(a)) and the other one with the DOM turned by 90° which leads to a scan in zenithal direction with respect to an upright orientation of the DOM (see Figure 9.3 (b)). The scan paths are also indicated in Figure 9.3 (c), which shows a Mollweide projection [51] of the PMT active areas positioned on the surface of a DOM by the red (azimuthal scan) and blue (zenithal scan) lines. A point on these lines represents the direction to the light source for one step of the scan. As reference, the PMT-channel IDs are also depicted. The scans were performed in steps of 1°. The mean number of photoelectrons was calculated for all PMTs and all scanned angles as shown in the previous section.

Systematic differences between measurement and Monte Carlo setups

The data from the Monte Carlo simulation was produced by L. Classen [49] with a modified *GEANT4* simulation toolkit of B. Herold [39]. In the simulation, the DOM is illuminated by a photon-emitting disk. Photons are emitted from random positions on the disk, with their direction being parallel to the surface normal. The dimension of the disk was chosen in a way that the whole DOM is illuminated with parallel photons. There are some differences in the measurement and Monte Carlo simulation setups that can cause systematic effects. The light source used in the measurement does not produce parallel light but, the measured intensity reduction of 0.3% at the border areas of the DOM compared to the centre seems negligible. In addition, inevitable quantum efficiency variations between different PMTs are not accounted for in the Monte Carlo simulation. Also, auxiliary structures like the titanium collar or the aluminium holder for the optical fibres guided through the penetrator were missing in the simulation setup. The PMTs being simulated as absorbing disks[3] represent a systematic simplification that may have significant effects on the data to Monte Carlo comparison. In addition, in the full DOM simulation the angle of the reflector rings is 45°, whereas it is 48° in the actually measured DOM. Another simulation of a single PMT in glass is, however, available with a reflector ring angle of 48°. It is used to study the influence of the reflector ring angle and to explain differences of measurement and Monte Carlo simulation of the angular acceptance of a DOM.

DOM acceptance in azimuthal and zenithal scans

Figure 9.4 shows the overall DOM acceptance for each angle of the scan in azimuthal (a) and zenithal (b) direction. The relative acceptance A_{rel} is acquired by adding up the mean number of photoelectrons λ_{ij} over all PMTs (i) for each angle of the scan (j), respectively:

$$A_{\text{rel},j} = \sum_{i=0}^{30} \lambda_{ij} \,, \tag{9.3}$$

and dividing the result by the maximum value, for normalisation. For comparison, the Monte Carlo acceptance is shown as well as the difference between data and Monte Carlo. Seemingly random fluctuations in the azimuthal scan can be explained by differences in quantum efficiency of different PMTs as well as the influence of the titanium collar blocking light or allowing for reflections at certain angles.

[3] When a photon in the simulation hits such a disk, it is absorbed and, with a certain probability (which represents the detection efficiency) counted as a hit, disregarding any physical effects inside the PMT.

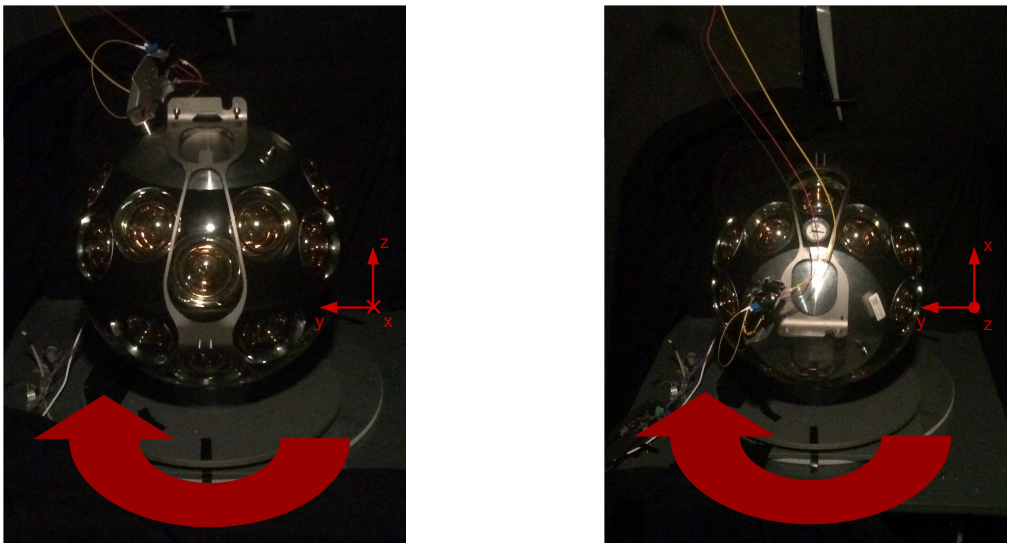

(a) (b)

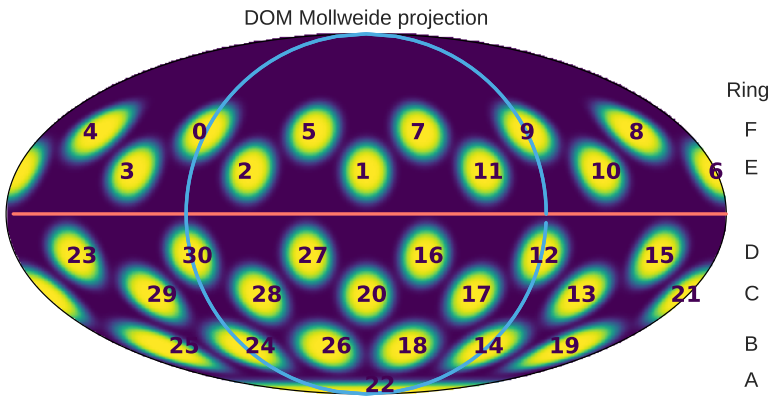

(c)

Figure 9.3: *Orientation of the DOM during the scan in azimuthal direction (a) and in zenithal direction (b) as well as a Mollweide projection of a DOM (c). The two scan directions are indicated by red (scan in azimuthal direction) and blue (scan in zenithal direction) lines. PMTs are indicated as yellow discs, and the numbers represent the corresponding PMT-channel IDs. The official DOM coordinate system is indicated as well.*

The comparison of the zenithal acceptances reveals systematic differences between data and Monte Carlo simulation. In order to explain these differences, the influence of the different reflector ring angles is investigated. For that, the simulated single PMT acceptances with reflector ring angles of 45° and 48° (see Figure 9.8 (left)) were scaled up to a full DOM acceptance by convoluting them with the 31 PMT pointing directions in the DOM. Similar to the Monte Carlo simulation in Figure 9.4 (b), a cut-out for $\varphi = 0$ for both reflector ring angles is presented in Figure 9.4 (c). The differences at small angles, resulting from the different reflector ring angles, explain, at least partly, the differences in the zenithal acceptances of data and Monte Carlo simulation in Figure 9.4 (b). The remaining discrepancies can be attributed to reflections at the walls of the darkroom or at the metal structures of the DOM (see Figure 9.3 (a) and (b)).

Figure 9.5 shows the intensity measured by the different PMTs during the azimuthal scan. The mean value of the mean number of photoelectrons over all angles (j) is calculated for the different PMTs (i):

$$\lambda_{i,\text{mean}} = \sum_{j=0}^{359} \frac{\lambda_{ij}}{360} \,. \tag{9.4}$$

Different colours represent the different rings the PMTs are positioned in. Variations in the mean number of photoelectrons of PMTs in the same ring can be explained by different quantum efficiencies, the titanium collar and other structures in the DOM. The zenith dependence fits a sine shape while the increased sensitivity for small angles (see Section 7.3) is diminished by refraction at the transitions between air and glass. In addition, during the azimuthal scan, PMTs are not directly illuminated (minimum angle of illumination is $\approx 17°$), which further reduces the pointing effect.

Mollweide projections of different scan angles in steps of 60° for the azimuthal and zenithal scan are shown in Figures 9.6 and 9.7.

Single PMT angular acceptance

A comparison between the relative angular acceptance of a PMT equipped with a reflector ring as shown in Section 7.3 and a PMT integrated in the scanned DOM as well as of a PMT from the Monte Carlo simulation is shown in Figure 9.8 (left). In addition, the Monte Carlo simulation with one PMT in a glass sphere with a reflector ring angle of 48°, matching the angles of the reflector rings in the measured DOM is shown. In the measurement, the PMT in the DOM pointing directly downwards is chosen for this comparison since it is directly illuminated during the zenithal scan so that the scan angle matches the angle relative to direct illumination (with an offset of 180°). It is noticeable that the pointing effect of the reflector rings expressed by the increased steepness of the dark blue curve (PMT with reflector measured outside of the DOM) is more pronounced compared to the other curves (PMT in the DOM data and Monte Carlo for 45° and 48° reflector angle). This difference can be explained by the refraction of photons at the transition between air and glass, reducing the angle of incidence at the glass α_{air} to

$$\alpha_{\text{glass}} = \arcsin\left(\sin(\alpha_{\text{air}}) \cdot \frac{n_{\text{air}}}{n_{\text{glass}}}\right), \tag{9.5}$$

where α_{glass} is the angle of the photon arriving at the PMT and n_{air} and n_{glass} are the refractive indices of air and glass, respectively. This refraction results in a lensing effect of the glass sphere, which

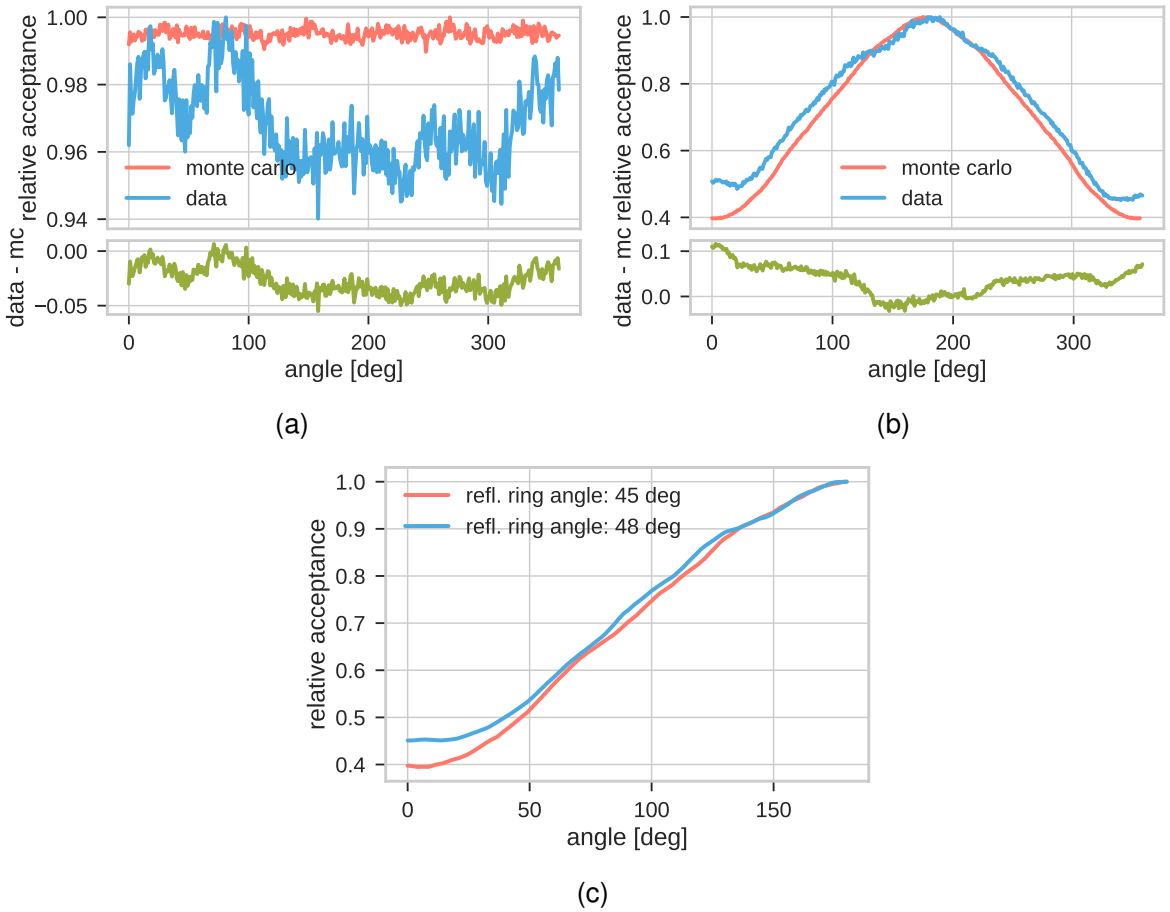

Figure 9.4: *Data/Monte Carlo comparison of DOM angular acceptance for both azimuthal (a) and zenithal (b) scans. Acceptance values are independently normalised to unity at their respective maximum values; Monte Carlo is shown in red, data in blue and the difference between data and Monte Carlo in green. In addition, the influence of different reflector ring angles on the acceptance in zenithal direction ($\varphi = 0$) is shown (c). For that, the simulated single PMT acceptances with reflector ring angles of 45° and 48° were used. The full DOM acceptances were calculated by convoluting the pointing directions of the 31 PMTs with the single PMT acceptances resulting in an acceptance map over the total solid angle range. A cut-out for $\varphi = 0$ is shown.*

does not exist in this form for a DOM in water since water and glass have a similar refractive index ($n_{\text{water}} \approx n_{\text{glass}} \neq n_{\text{air}}$). Transitions between glass and optical gel as well as optical gel and glass of the PMT are neglected here. The impact of the different reflector ring angles on the simulated angular acceptance seems rather large. In addition, the fact that the Monte Carlo acceptances with the correct angle of 48° matches the data better than that with the angle of 45° confirms the good agreement between data and Monte Carlo. Furthermore, it shows the susceptibility of the DOM acceptance to the reflector ring angle and can, at least partly, be held liable for the systematic differences in the data and Monte Carlo comparison of the overall DOM acceptance (since the wrong reflector angle of 45° was used in the full DOM Monte Carlo simulation).

Figure 9.8 (right) shows the mean number of photoelectrons for different PMTs, representing

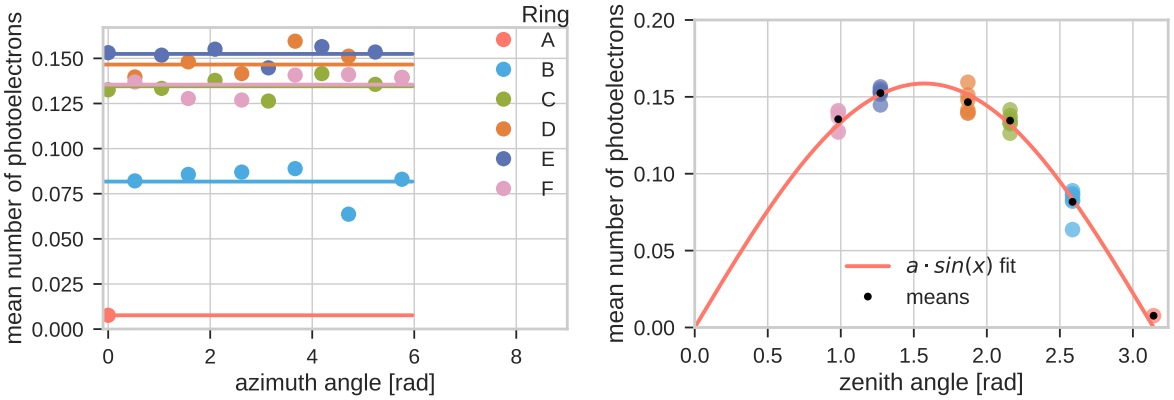

Figure 9.5: *Mean over all angles of the mean number of photoelectrons for all PMTs as a function of their azimuth angle (left); since the PMTs are arranged in rings, different colours represent different rings and different zenith angles θ. Fluctuations can be attributed to differences in quantum efficiency of the PMTs and the influence of the titanium collar and other structures in the DOM. In the right plot, the same data is shown as in the left plot but as a function of the zenith angle, and a sine function is fitted. Again, different rings are represented in different colours. The pointing effect (increase in sensitivity for small angles) of the reflector rings that increases the sensitivity at small angles, which is already diminished for a DOM scan in air (see Figure 9.8 and the text below), is further reduced by the fact that during the azimuthal scan, no PMT is ever directly illuminated.*

different rings as a function of the scan angle for the azimuthal scan. Note that the scan angle is not equal to the angle relative to head-on illumination of a PMT since no PMT is head-on illuminated during the azimuthal scan (see Figure 9.3). Hence, the pointing effect is only present for the PMTs closest to the scan axis (visible by the kink in the brown and dark blue curve) but quickly diminishes, leading to a broadening of the acceptances for PMTs further away from the scan axis.

Conclusion

Given the results presented in this section, it can be concluded that DOM scan measurement and simulation are in good agreement with the exception of some effects that can be attributed to the systematic differences in the setups, especially the different reflector ring angles. Nevertheless, it is important to remember that the measurement was performed in air, disregarding some effects arising from the different transition physics between water and glass compared to air and glass. The comparison shows that the simulations in air can be trusted. Changing the surrounding medium from air to water in the simulation is a relatively easy step where no major systematic errors should occur. A simulation with the official KM3NeT DOM simulation framework OMGSim [52] is, however, needed. This framework allows for a much better emulation of the conditions of the DOM scan measurement and a comparison of the simulated results with the data should yield an even better agreement.

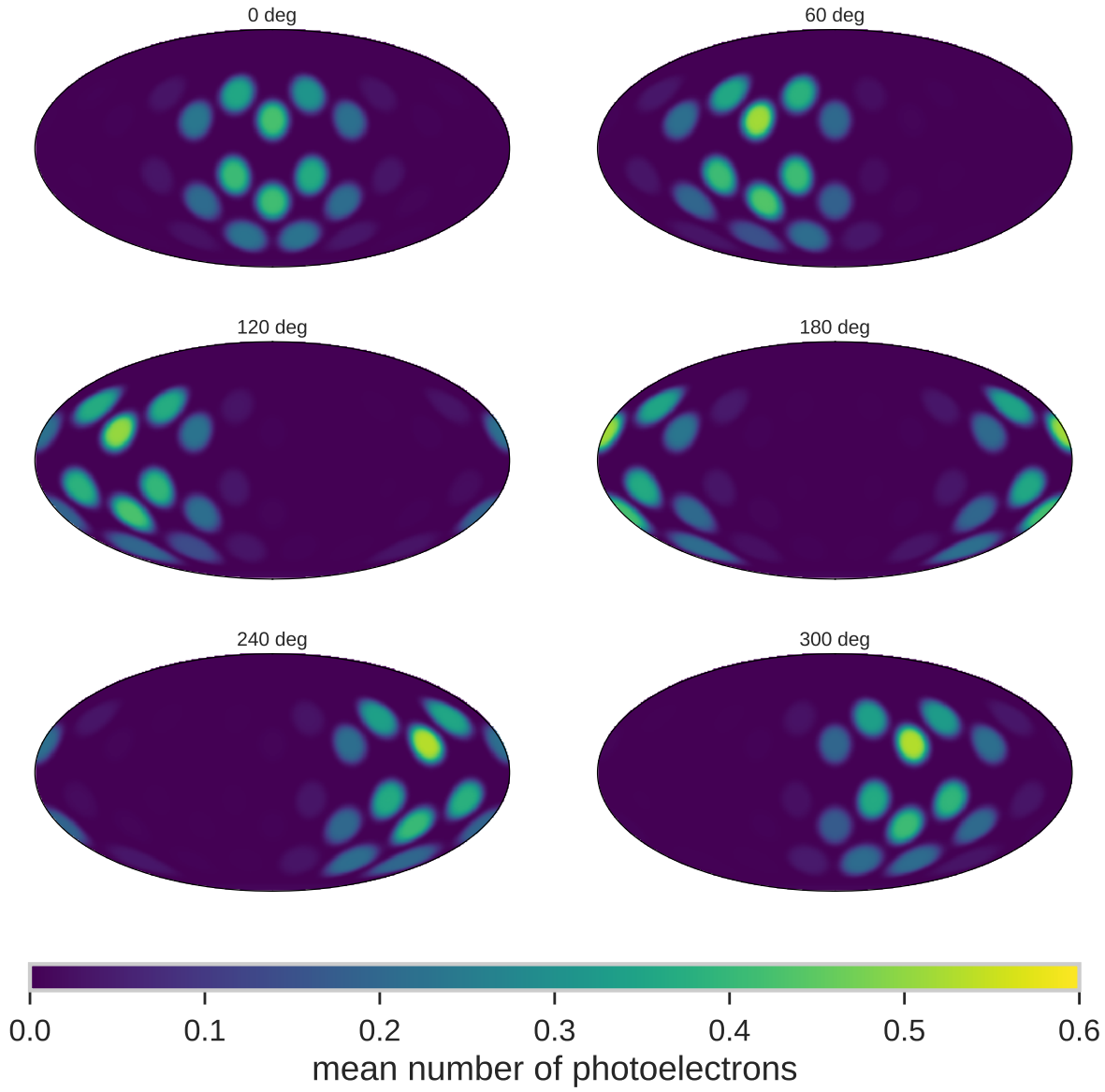

Figure 9.6: *Mollweide projection of the mean number of photoelectrons of all PMTs for different scan angles for the azimuthal scan.*

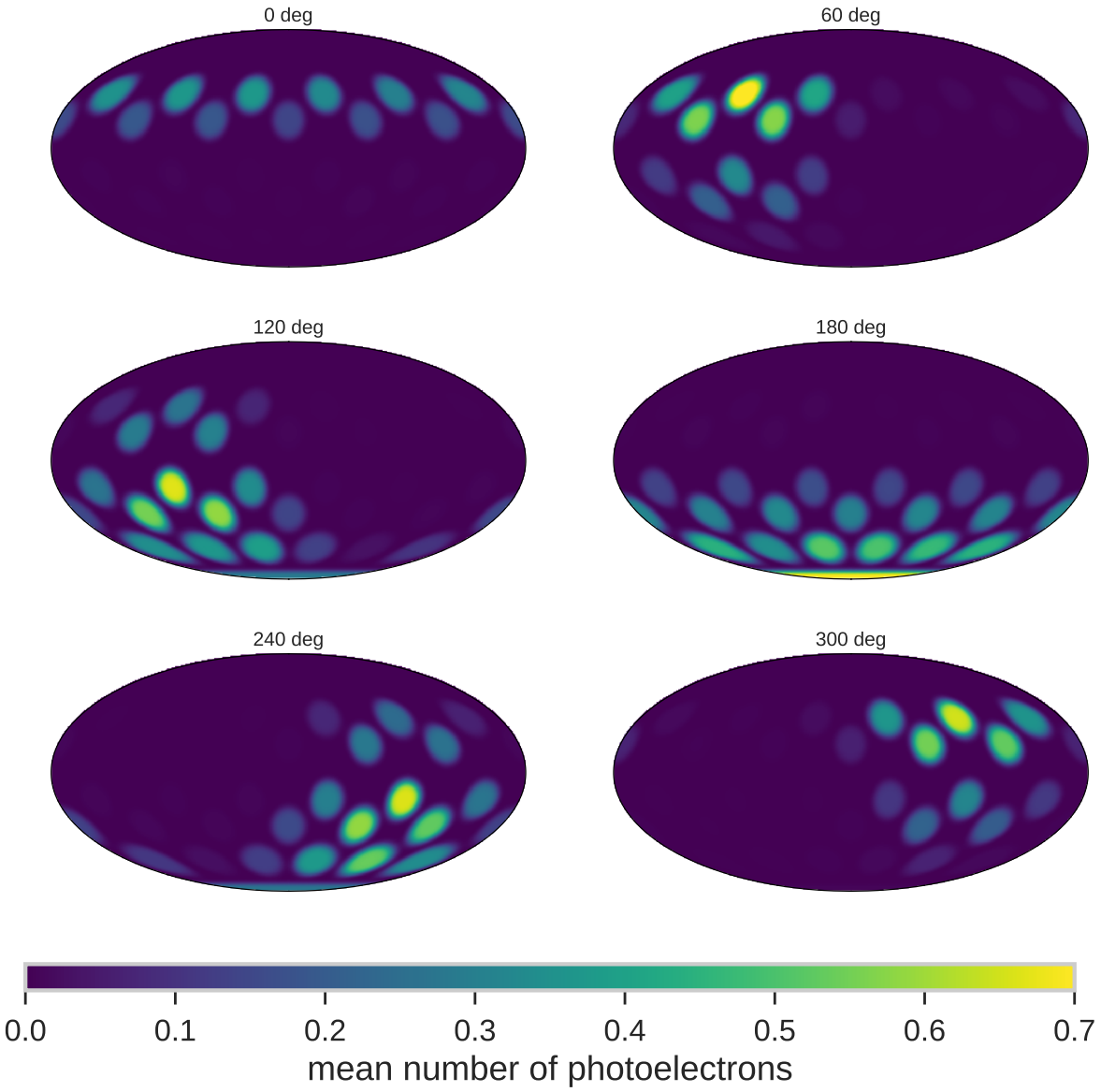

Figure 9.7: *Mollweide projection of the mean number of photoelectrons of all PMTs for different scan angles for the zenithal scan.*

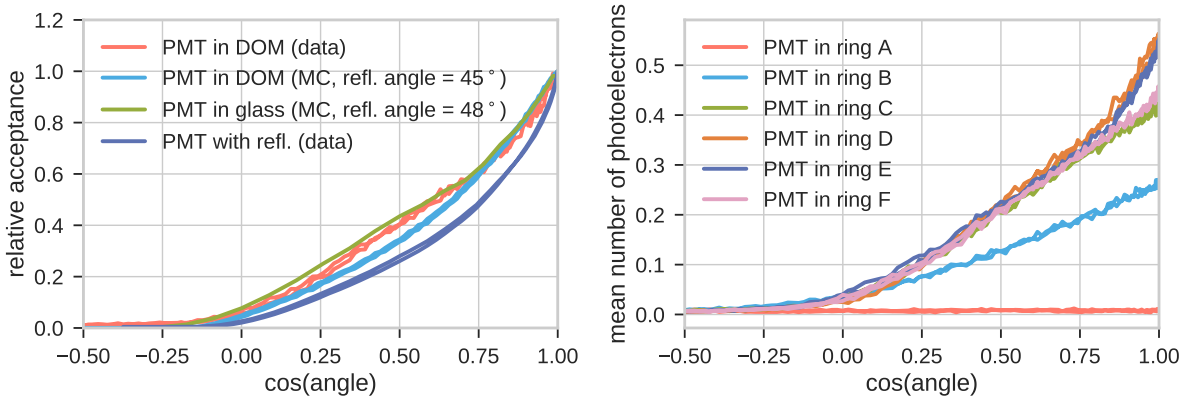

Figure 9.8: *Comparison between data and Monte Carlo simulation of single PMT angular acceptance in a DOM as well as angular acceptance of a PMT equipped with reflector ring not integrated in a DOM (left). The maximum value of each distribution is normalised to unity. The pointing effect (increased acceptance for small angles) is diminished by refractions at the transition of the photons from air to glass. The right plot shows the angular acceptance of different PMTs in different rings during the azimuthal scan. Increased sensitivity for small angles can be seen for PMTs in the rings closest to the scan direction (ring D and ring E).*

Part III

In-situ prototype calibration and data analysis

In this part analyses of in-situ data from the prototypes and the first lines of the KM3NeT detector are presented. With data from the prototype digital optical module (DOM), the influence of bioluminescent organisms on the measured rates is investigated. Additionally, coincident hits are used to study potassium 40 (^{40}K) decays and the directional distribution of atmospheric muons. A new concept to utilise ^{40}K decays for time and efficiency calibration of the DOMs is shown as well as its application to data retrieved from the prototype detection unit and from the first complete detection units. The influence of mechanical structures of the DOM on the determined efficiencies as well as an approach to correct for this influence is presented and the precision of time and efficiency calibration is discussed. Finally, the influence of the PMT high voltage on timing and measured rates of the DOMs is examined by a comparison of data from in-situ- and lab-based measurements.

Chapter 10

Prototype of a digital optical module

In April 2013, the first KM3NeT digital optical module (DOM) was mounted on the instrumentation line of the ANTARES detector, the so-called PPM-DOM (pre-production model of a digital optical module). A photograph is shown in Figure 10.1. It was the first time a module with the novel multi-PMT design was tested in situ. Data taking started at the day of deployment and ended in 2015. The PPM-DOM was equipped with 31 PMTs of the type ETEL D783KFLA with a photocathode diameter of 72 mm. Reflector rings surrounding the PMTs provide an increased effective diameter of 85 mm. A report on the deployment, data taking, calibration and data analysis was published [35]. Contributions of the author to the calibration and data analysis are presented in this chapter, which include investigations of

- single-hit rates and bioluminescence;
- genuine and random twofold coincidences;
- higher multiplicity coincidences and muon identification.

10.1 Single-hit rates and bioluminescence

Single hits are defined as hits not being coincident with other hits in a certain time window on the ns scale (here 20 ns). Main sources of single hits are the dark rate of the PMTs (see Section 4.9) and photons resulting from ^{40}K decays and bioluminescence (see Section 3.4). In the context of the KM3NeT data acquisition, hits consist of time, ToT and PMT-channel identifier and are stored in timeslices with a length of 134 ms in the case of the PPM-DOM. As a first step, data from one example run (run 901) with a data acquisition time of roughly one hour was analysed by counting the number of hits in each timeslice. Figure 10.2 (left) shows the hit rates for all individual PMTs (indicated by different colours) over the whole run. Different baseline rates can be identified with values between roughly 3 to 10 kHz and so-called bioluminescence bursts, with hit rate values in single timeslices of up to almost 1 MHz. The plot on the right in Figure 10.2 shows a zoomed-in view of a part of the run. Two different kinds of bursts can be identified: several PMTs counting increased rates in several consecutive timeslices and one or several PMTs counting increased rates in only one or two consecutive timeslices. The spatial distribution of the rates in timeslice 3236 during the burst shown in Figure 10.2 (right) is illustrated in Figure 10.4 (left). The clustering of the highest rates

Figure 10.1: *Photograph of the KM3NeT PPM-DOM mounted at the ANTARES instrumentation line. Figure taken from [37].*

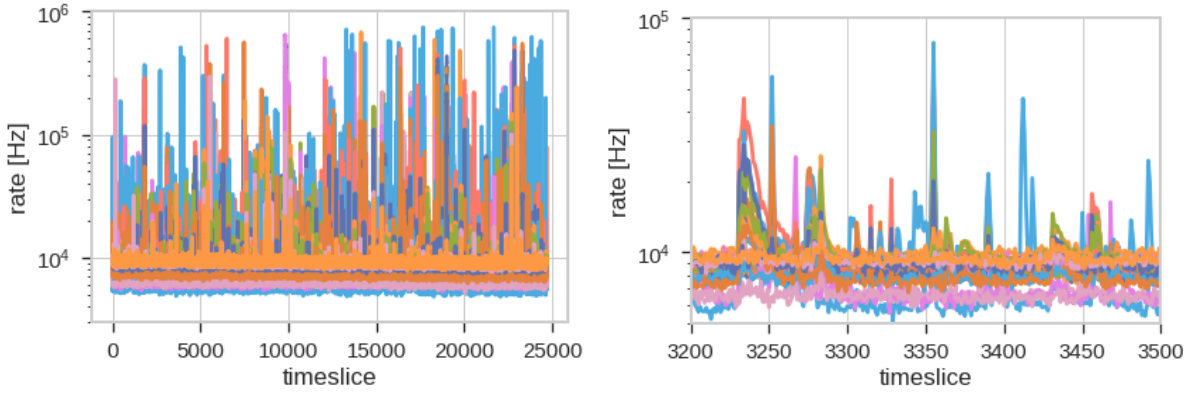

Figure 10.2: *Hit rates measured with the PPM-DOM in the example run (left) and a zoomed-in view of a part of the run (right). Different colours indicate different PMTs.*

indicates that most of the photons contributing to the burst come from a light emitting source close to the DOM, substantiating the assumption that the burst is caused by a bioluminescent organism hitting the DOM or being triggered by a turbulence near the DOM.

In order to remove most of the bioluminescence bursts, a high-rate veto can be introduced

suspending all timeslices with a rate exceeding a certain threshold. This threshold is determined for each PMT individually, considering their different base-line rates. The rates of all timeslices are filled in a histogram, and a Gaussian function is fitted to the histogram data. The high-rate veto is then determined by the Gaussian mean plus three standard deviations. Figure 10.3 shows the rate histograms of all PMTs during the example run (left) and definition of the high-rate veto for one PMT, indicated as black vertical line (right). The number of times a PMT exceeds the high-rate veto during the example run is given in Figure 10.4 (right) as a function of its pointing direction. A preferred direction can be identified with the PMTs with the highest number of high-rate veto timeslices pointing towards the electronics container of the ANTARES line. As stated in [35], most bioluminescence bursts are caused by stress-related photon emission of bioluminescent organisms hitting structures of the ANTARES line or the DOM itself.

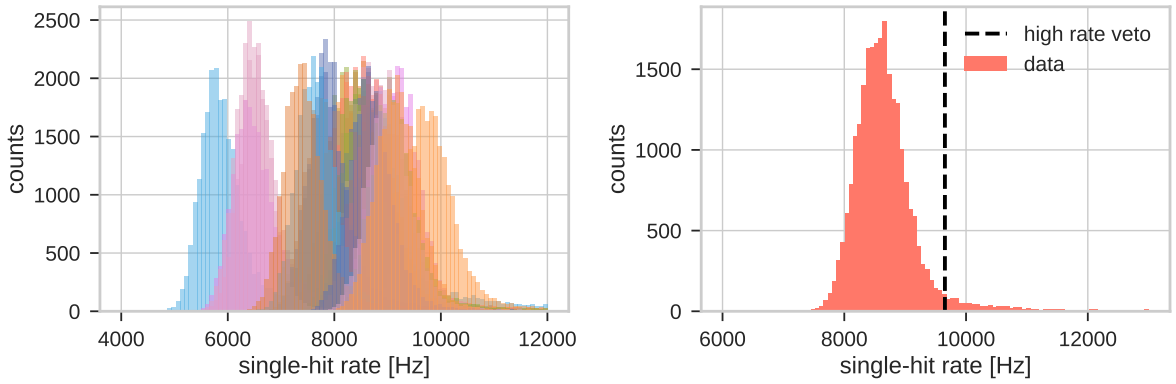

Figure 10.3: *Distributions of single-hit rates off all individual PMTs (different colours indicate different PMTs) (left) and number of high-rate veto determined by a Gaussian fit (three standard deviations above the mean) (right).*

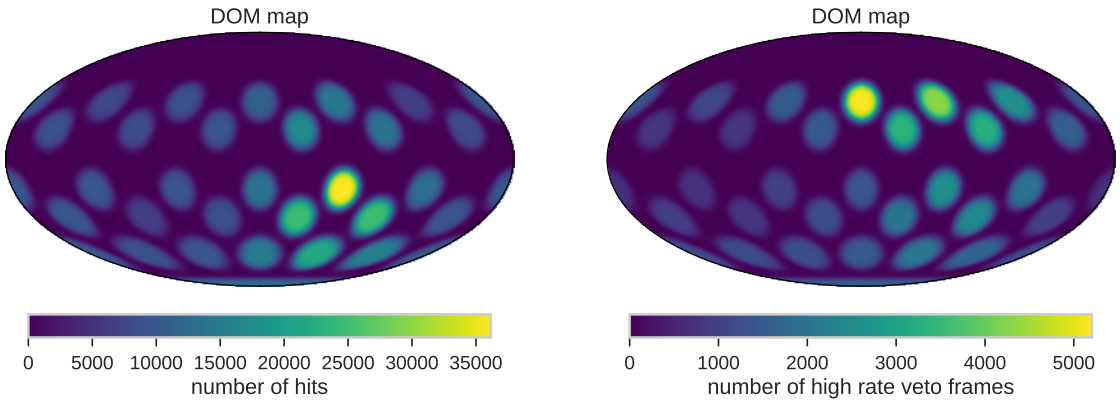

Figure 10.4: *Illustration of PMT rates in timeslice 3236 in Figure 10.2 during a burst (left) and high-rate veto frames for all PMTs during the example run (≈ 1 h) (right). The circles represent the different PMTs shown in a Mollweide projection.*

10.2 Coincident hits and potassium 40

The typical time differences of photons from a neutrino-induced event arriving at a single DOM is of the order of ns. In order to separate such events from random background like hits resulting from dark rate of the PMTs, bioluminescence and potassium 40 (^{40}K) decays, a first filter is to search for coincident hits in a time window of typically 20 ns. This filter is applied to all data. If the arrival times of a hit p and a subsequent hit q on a different PMT are less than 20 ns apart, they form a coincidence. Possible further hits arriving at the time of the first hit p + 20 ns are included in the coincidence. Figure 10.5 shows the multiplicity of all coincidences found in the example run (left), as well as single-hit rate, twofold coincidence rate and threefold coincidence rate summed over all PMTs of the DOM (right). The high-rate veto discussed in the previous section was not applied to this data. Therefore, bursts are still visible mostly in the single-hit rates and twofold coincidence rates; starting at threefold level, bursts are effectively filtered out. While single-hit rates are dominated by PMT dark rates, bioluminescence and ^{40}K decays, twofold coincidence rates are dominated by random coincidences. A considerable contribution is made by coincidences where all hits originate from the same ^{40}K decay (genuine ^{40}K coincidences) which dominate up to a hit multiplicity of roughly seven [39]. Coincidences with more than seven hits are mostly caused by atmospheric muons.

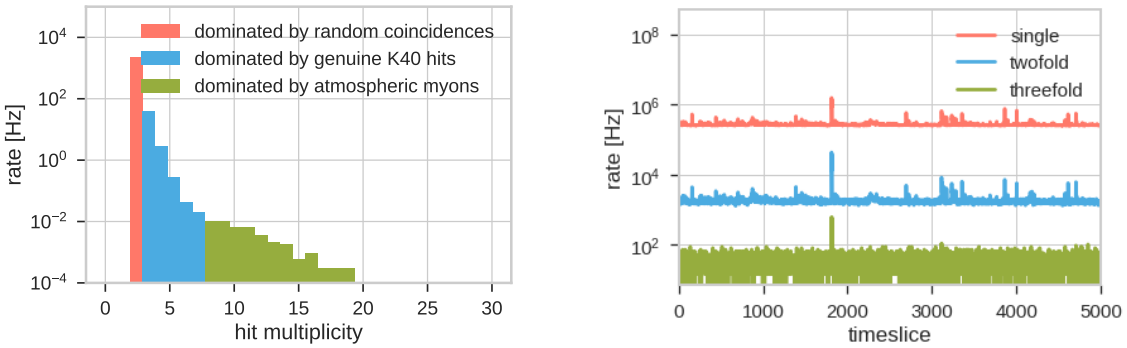

Figure 10.5: *Multiplicity of all coincidences found in the example run (left) and rates of single hits, twofold and threefold coincidences (right). The hits of all PMTs are summed. Most bursts present in the single-hit rates and the twofold coincidence rate are clearly suppressed in the threefold coincidence rate.*

In order to identify genuine twofold ^{40}K coincidences out of all twofold coincidences on a statistical basis, a unique index (also referred to as combination) is assigned to each PMT pair and the time difference between the hits is calculated for each combination. Figure 10.6 shows the rate of time differences ($t_{PMT2} - t_{PMT1}$) of all twofold coincidences found in the example run for each individual PMT pair (left), as well as an exemplary PMT pair with a small angle between the pointing directions and a Gaussian fit (right). The area below the Gaussian fit represents the genuine twofold ^{40}K rate. Those hits are smeared in time due to the spatial distribution of the ^{40}K decays as well as due to the transit time spreads of the PMTs involved. The mean of the Gaussian fit corresponds to the different data acquisition times of the PMT-base pairs. These time differences can be identified and corrected for in order to synchronise all PMTs in time. The methodology of time as well as efficiency calibration using twofold coincidence rates is subject of this work and is explained in detail

in Chapter 11. The baseline or offset value of the Gaussian fit represents random coincidences. The total rate is calculated by summing over all time bins. By applying the described method to all PMT pairs, the overall rate of genuine and random twofold coincidences are calculated, resulting in a roughly four times larger random than genuine twofold rate.

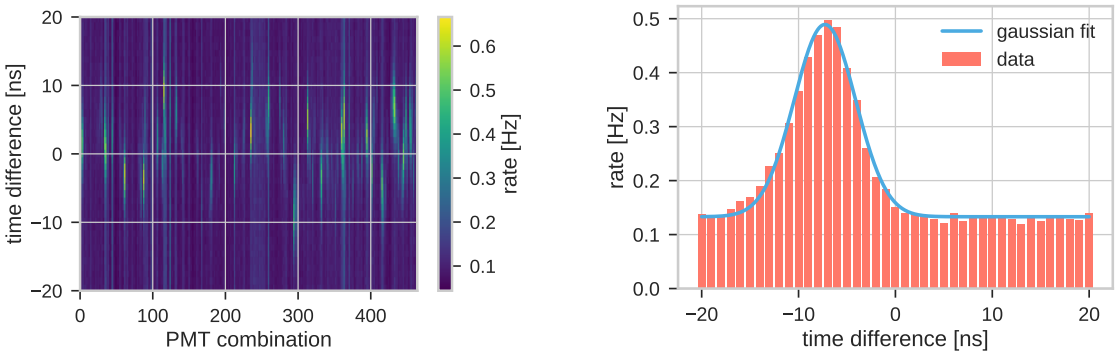

Figure 10.6: *Rates of time differences of hits in twofold coincidences for each individual PMT pair (left) and for a certain PMT pair with small angle between pointing directions (right).*

Another interesting way to look at the genuine twofold ^{40}K coincidences is to examine the dependence of the rate on the angle between the pointing directions of the involved PMTs. Those angles were calculated for each unique index, comprising all PMT combinations. Figure 10.7 shows the rates as a function of the cosine of the angle between all 465 PMT pairs. Although there is no analytic model explaining the exponential behaviour, simulations show a similar dependence. A comparison of data and Monte Carlo is shown in Chapter 13.

Figure 10.8 shows the rate of involvement of the PMTs in seven-fold or higher multiplicity coincidences as a function of their pointing directions. The excess at upwards pointing PMTs can be explained by downgoing atmospheric muons that dominate high-level coincidences. This result proves the capability of muon identification with a single multi-PMT optical module.

In this section, the concept of using hit coincidences in space and time as first level filter was introduced. It was shown that the raw data can be reduced by a significant amount and most parts of the background can be filtered out. In addition, the distinction between random and genuine coincidences offers the possibility of in-situ time and efficiency calibration. The angular distribution of high-multiplicity coincidences proves the capability of atmospheric muon identification with single DOMs.

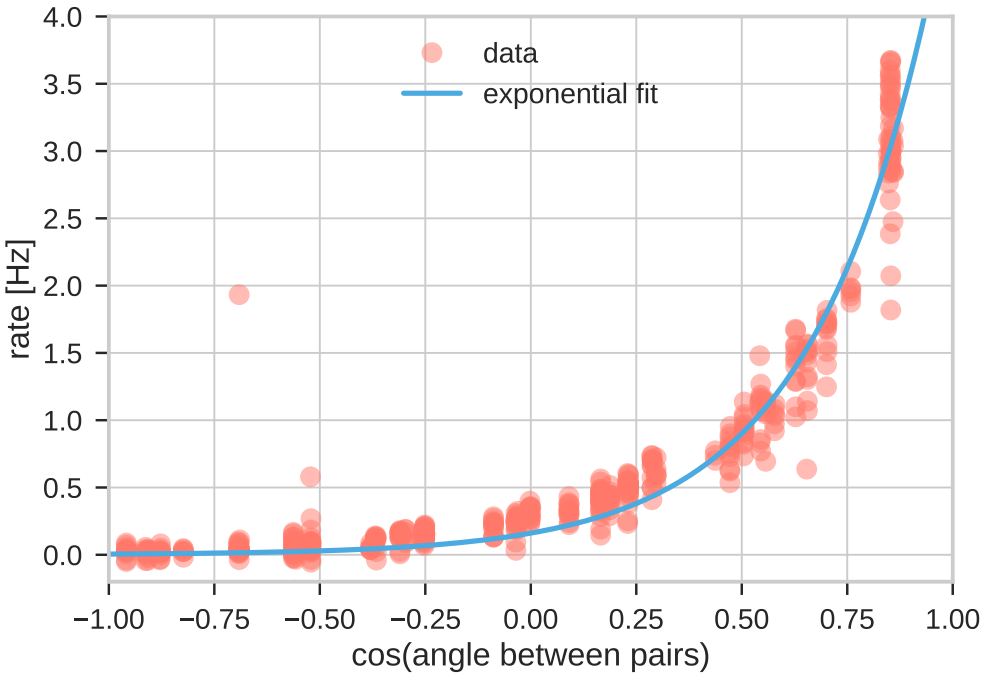

Figure 10.7: *Genuine twofold ^{40}K rates of all PMT combinations as a function of the cosine of the angle between the pointing directions of the involved PMTs. The line shows an exponential fit.*

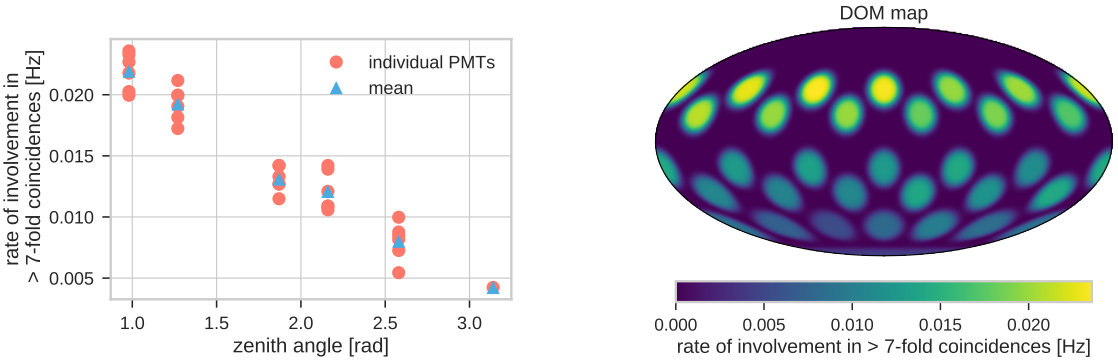

Figure 10.8: *Rate of involvements in sevenfold or higher multiplicity coincidences of PMTs as a function of the zenith angle of their pointing directions (left) and as a function of their pointing direction displayed in a DOM map in Mollweide projection (right). The visible excess at upwards pointing PMTs is consistent with the assumption that downgoing atmospheric muons dominate those high-multiplicity coincidences.*

Chapter 11

Methods of in-situ calibration

Knowing the relative efficiencies and correcting for the time offsets of the individual PMTs is important for reconstruction algorithms. In addition to calibration procedures in the lab using expensive test setups, there is an excellent way to use the radioactive decays of potassium 40 for an in-situ intra-DOM (also referred to as inter-PMT) time and efficiency calibration of the DOMs deployed in the deep sea. By using LEDs included in the DOM, so-called nano-beacons, it is also possible to perform an inter-DOM time calibration. Methods for those calibration procedures will be introduced in this chapter. It is shown that a precision of $\approx$ 1 ns can be achieved for both the intra-DOM and the inter-DOM time calibration.

11.1 Intra-DOM calibration

The salt dissolved in the sea water contains the radioactive nuclide potassium 40 (^{40}K) as mentioned in Section 3.4. Cherenkov light from the ^{40}K decays is ad hoc considered as optical background, but can be used for in-situ time and efficiency calibration. Photons produced by decays evenly distributed around the DOM can produce coincidences (hits on different PMTs in a small time window), as shown in Chapter 10. From the distribution of the time differences of such coincident hits the differences in data acquisition times of the PMTs can be identified. These differences originate from different transit times of the PMTs and different time delays in the readout electronics, resulting in different time stamps of hits even though they were produced by simultaneously arriving photons. The coincidences are extracted from all hits, as mentioned in Section 3.2, using the level-one trigger which searches for twofold or higher coincidences. It is possible to use only twofold coincidences or also higher multiplicities by counting each twofold combination within it (e.g. twofold combinations ij, ik and jk of a threefold coincidence ijk). In order to visualise the time differences, a histogram is filled for each PMT combination (i, j) with the time difference of twofold coincidences $t_j - t_i$. The coincidences can be divided into genuine ^{40}K coincidences and random coincidences. The shapes of the distributions are well described by Gaussians with constant offsets. The mean values of the Gaussians represent the corresponding time differences, their widths represent a combination of the transit time spreads of both PMTs, the spatial distributions of the ^{40}K decays and scattering of the photons; the areas below the Gaussians are proportional to the decay rates; and the offsets originate from random coincidences (mostly from ^{40}K decays and bioluminescence). Figure 11.1 shows such a fitted histogram and the parameters derived. Data was taken from one PMT combination of a DOM of the first detection unit deployed at the *Capo Passero* site (see Chapter 13).

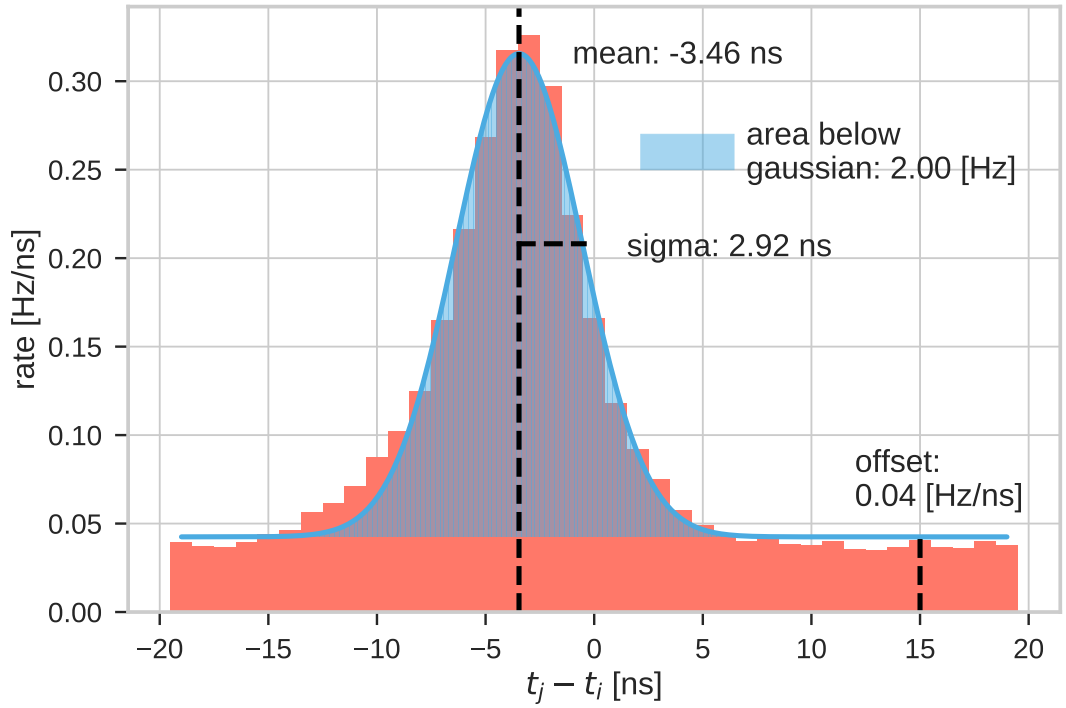

Figure 11.1: *Rate distribution of twofold coincidences for a certain PMT pair (i, j) with small angle between the pointing directions fitted by a Gaussian function. Data was taken with the first detection unit deployed at the Capo Passero site. The number of coincidences is divided by the time of data acquisition, resulting in a rate per time difference bin. The mean value corresponds to the relative time difference between the PMTs; the sigma represents the combined effects of the transit times of the PMTs, the spatial distribution of ^{40}K decays and scattering of the photons; the blue area below the Gaussian represents the total genuine ^{40}K rate; the offset is created by random twofold coincidences due to random ^{40}K hits, bioluminescence and dark rate.*

The next step is to repeat the procedure of filling the histograms with coincidences for all PMT combinations. Determining the time and efficiency calibration can follow different approaches. The goal of time calibration is to correct for the 31 individual time offsets of the PMTs so that simultaneously arriving photons result in equal measured hit times ($t_j - t_i = 0$). That means that in the ideal case all time difference distributions are centred around zero. In the following, available methods for time and efficiency calibration are listed.

- Time calibration by **PMT hopping** is the most generic method. Starting e.g. at the PMT pointing downwards and chaining all PMTs, the time differences of all PMTs relative to the starting PMT can be calculated. By moving over different paths, a mean value can be determined and the error can be reduced.

- A slightly more advanced method is to solve the **over-determined set of equations**

$$A \cdot \vec{t}_{\text{PMT}} = \vec{t}_{\text{comb}} \tag{11.1}$$

where A is a 31×465 matrix where each line represents a PMT combination with $+1$ and -1 at the columns representing the PMT IDs of the combination. The remaining entries are zero. $\vec{t}_{\text{comb}}$ has a dimension of 465 and consists of the time differences of the PMTs of each combination determined from the mean of the respective Gaussian fits (as shown in Figure 11.3, left), and $\vec{t}_{\text{PMT}}$ has a dimension of 31 and solves the equation system with the resulting time offsets of the PMTs that have to be applied for the correction.

- A **global fit** to the 465 time difference histograms implemented in the official KM3NeT software framework *Jpp*. A two-dimensional histogram (see Figure 11.2) with the time difference of the coincidences Δt on the one axis and the unique combination ID c, depending on the PMTs involved in the coincidence (see Table 11.1), on the other axis is fitted by a two-dimensional function

$$R(\Delta t, c) = A(\alpha(c)) \cdot \epsilon(c) \cdot G(\Delta t, t_0(c), \sigma(c)) \tag{11.2}$$

where

$$A(\alpha) = p_0 \cdot \exp(p_1 + \alpha \cdot (p_2 + \alpha \cdot (p_3 + \alpha \cdot p_4))) \tag{11.3}$$

and

$$G(t, t_0, \sigma) = \frac{1}{\sqrt{2\pi\sigma^2}} \cdot \exp\left(-\frac{1}{2} \cdot \frac{(t - t_0)^2}{\sigma^2}\right). \tag{11.4}$$

Where $\alpha(c)$ is the angular distance between the PMTs of the combination c. Free parameters of the fit are $p_0 \dots p_4$, 31 efficiencies ϵ, relative time offset t_0 and widths σ values for each individual PMT with

$$\epsilon(c) = \epsilon_{c_1} \cdot \epsilon_{c_2}, \quad t_0(c) = t_{0_{c_1}} - t_{0_{c_2}} \quad \text{and} \quad \sigma(c) = \sqrt{\sigma_{c_1}^2 + \sigma_{c_2}^2}\,, \tag{11.5}$$

where c_1 and c_2 are the PMTs of a combination c. The random coincidences that lead to a non-zero offset in the histogram are subtracted before the fit so that the parameter for the offset is fixed at zero in the fit.

- Another method, developed by the author, consists of a number of **independent fits and minimisations** and is implemented in the *KM3Pipe* framework [53]. The first step is to fit every one-dimensional histogram (see Figure 11.1) with a Gaussian function and derive the respective mean, rate (area below the Gaussian) and sigma values. Mean and rate values are, as shown in Figure 11.3, plotted as a function of the angle between the pointing directions of the PMTs involved in the respective combination. The rates are fitted with an exponential function similar to that in Equation 11.3. After that, three independent minimisation procedures are performed. For the mean values m_c, the following sum

$$\sum_c \left(\left(m_c - \left(t_{0_{c_2}} - t_{0_{c_1}}\right)\right) \cdot w_c\right)^2, \tag{11.6}$$

is minimised by varying the 31 t_0 values with w_c being a combination-dependent weight which is, by default, the error of m_c retrieved from the respective Gaussian fit. This provides for an

c_1 (PMT ID 1)	c_1 (PMT ID 2)	c (combination ID)
0	1	0
0	2	1
⋮	⋮	⋮
0	30	29
1	2	30
⋮	⋮	⋮
29	30	464

Table 11.1: *Assignment of a unique combination ID to all individual PMT pairs.*

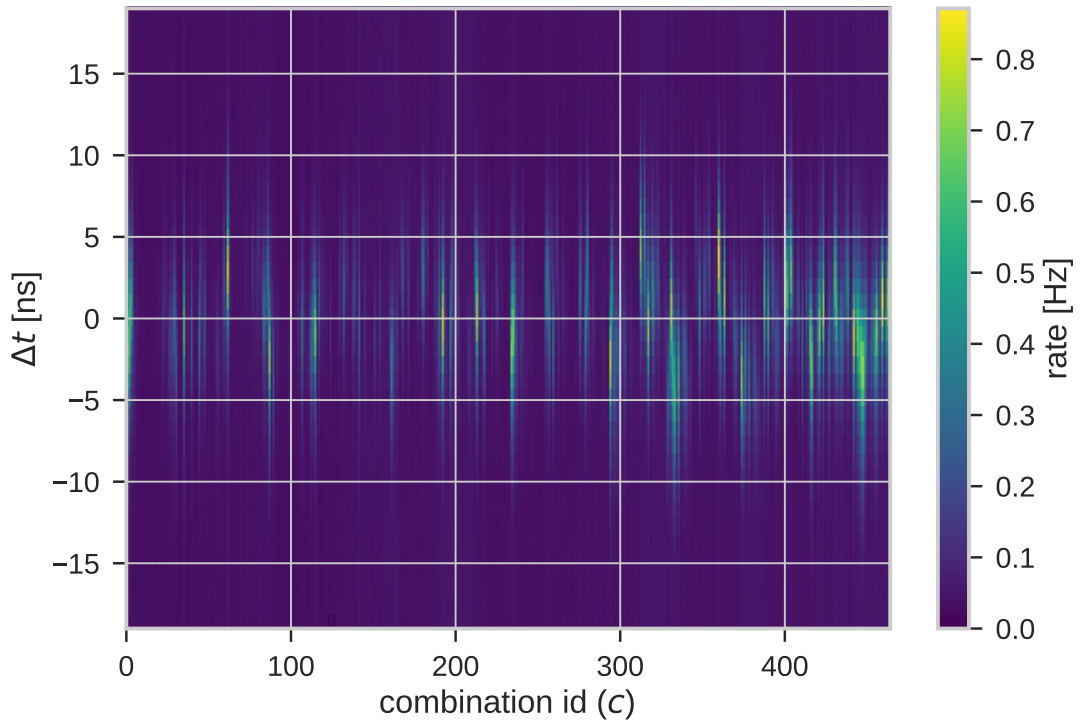

Figure 11.2: *Rate of twofold coincidences as a function of the PMT combination ID and the time between hits.*

increased weighting of close-by PMT combinations with a well working Gaussian fit, down-weighting those with a large angle between their pointing directions where the Gaussian fit is usually not that good.

The 31 efficiency values ϵ are acquired by minimising the sum

$$\sum_c \left(\left(\frac{r_c}{\epsilon_{c_1} \cdot \epsilon_{c_2}} - f_c \right) \cdot w_c \right)^2 , \tag{11.7}$$

where r_c is the rate (area below the Gaussian fit) for each combination, f_c is the value of the exponential fit function at the angle value corresponding to each combination, and w_c is, again, a weight that is here the error of the fitted rate value.

In addition to the time offset and efficiency values, the widths of the Gaussian fits g_c can be used to determine a measure of the PMT transit time spreads σ. This is achieved by minimising the sum

$$\sum_c \left(\left(\sqrt{\sigma_{c_1}^2 + \sigma_{c_2}^2} - g_c \right) \cdot w_c \right)^2 , \tag{11.8}$$

where w_c is the combination dependent error of the fitted widths. As the local distribution of the ^{40}K decays around the DOM also has an impact on the widths of the distribution of twofold ^{40}K rates of the different PMT combinations, the determined transit time spreads have larger values than the pure transit time spreads of PMTs measured in the lab.

The Gaussian mean and rate values can then be corrected with the optimal efficiency and time difference values found in the minimisation. The Gaussian means for each combination m_c are shifted towards zero by subtracting the respective optimal time difference found in the minimisation of the sum in Equation 11.6:

$$m_c^{\text{corrected}} = m_c - \left(t_{0_{c_2}}^{\text{opt}} - t_{0_{c_1}}^{\text{opt}} \right) , \tag{11.9}$$

where $m_c^{\text{corrected}}$ are the corrected means shown as blue points in Figure 11.3 (left). The rate values for all combinations r_c are shifted towards the exponential fit by dividing them by the optimal efficiency values found in the minimisation of the sum in Equation 11.7:

$$r_c^{\text{corrected}} = \frac{r_c}{\epsilon_{c_1}^{\text{opt}} \cdot \epsilon_{c_2}^{\text{opt}}} , \tag{11.10}$$

where $r_c^{\text{corrected}}$ are the corrected rates shown as blue points in Figure 11.3 (right). The minimisation works very well in the case of the time differences, as the blue points (after correction) lie very close to zero, except for very large angles close to 180° where the rates are low and the Gaussian fits, and thus the means, have large errors. In case of the rates, the effect of structures in the DOMs, e.g. the titanium collar, is not included in the minimisation, a rather large scatter around the exponential fit curve remains. This problem as well as the precisions of time and efficiency calibration is discussed in Chapter 13.

11.2 Inter-DOM time calibration

For the inter-DOM time calibration so-called nanobeacon devices are used. A nanobeacon consists of a small electronics board equipped with an LED. The LED has a peak wavelength of $\approx$ 470 nm.

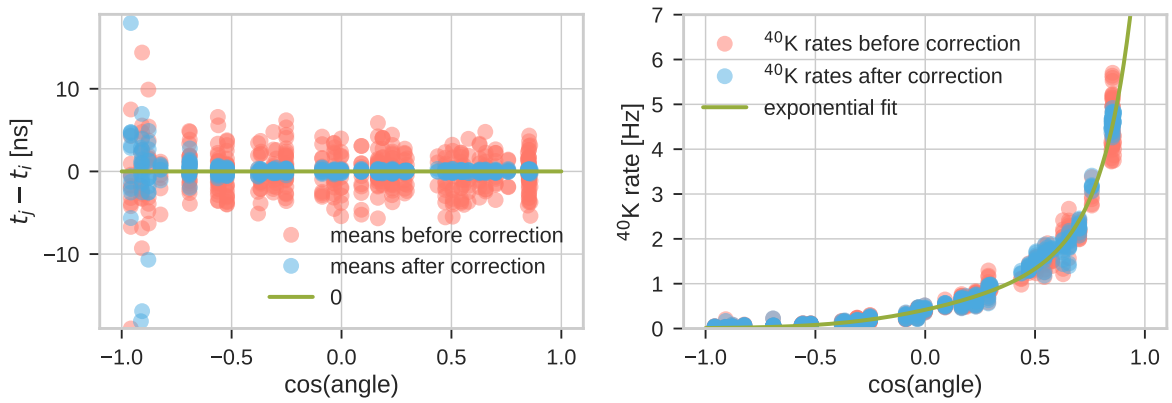

Figure 11.3: *Gaussian means (left) and areas below Gaussians (right) for all PMT combinations as a function of the angle between their pointing directions before (red) and after (blue) correction.*

It is included in each DOM, positioned at the top and pointing upwards. Being remote-controllable, the nanobeacon can emit light pulses with adjustable frequency and amplitude. Driven at maximum intensity, the number of photons per pulse is high enough that multiple DOMs can measure photons from one nanobeacon. Figure 11.4 shows a photograph of a nanobeacon device. A more detailed introduction of the nanobeacon device is given in [54]. There are different approaches for the in-situ determination of inter-DOM time offset using the nanobeacon. The one described in this section can achieve nanosecond precision. The application to data taken with the PPM-DU is shown in Section 12.2.

When a light pulse is emitted by the nanobeacon LED, it consists of a large number of photons. Most of the photons will be absorbed by the water on their way to the DOM. Relevant for the time calibration are those photons that reach the DOM above without being scattered. There are also always photons that never leave the DOM and are scattered onto PMTs in the same DOM as the active nanobeacon. The respective first hits on both DOMs originating from the nanobeacon light pulse can be found by using the trigger condition of two hits on one DOM in a 20 ns time window on at least two DOMs in a time window of the order of microseconds. With this condition events are produced. In those events, hits produced in either the DOM with the nanobeacon or e.g. the DOM directly above, are searched for. The time difference of the respective first hits is calculated, and the time that the photons need to travel between the two DOMs is subtracted. The resulting distribution of time differences is fitted with a Gaussian function, and the mean value is the time correction that has to be applied in the data acquisition in order to synchronise the two DOMs in time.

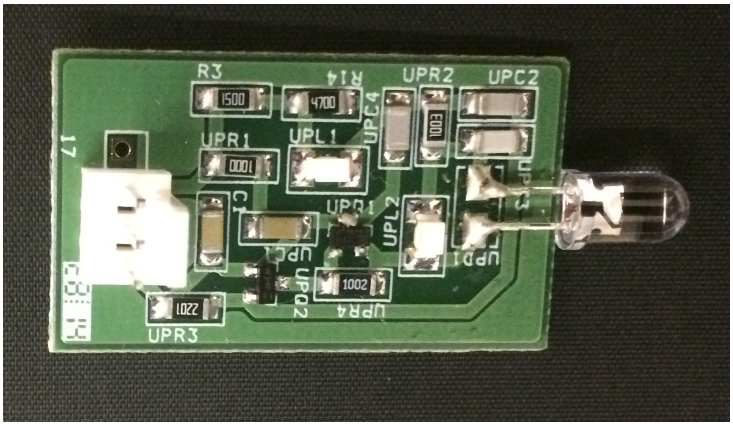

Figure 11.4: *Photograph of the nanobeacon device.*

Chapter 12

Prototype of a detection unit

Besides being the first working detector part deployed at the Italian site near *Capo Passero* on *Sicily*, the prototype detection unit (PPM-DU) was also the first opportunity to test newly developed deployment techniques, as well as auxiliary structures and devices like e.g. the nanobeacon. Although the PPM-DOM described in Chapter 10 had already been tested successfully, the PPM-DU was a very important step in the prototyping phase of KM3NeT since it first allowed for testing the interplay of several DOMs. The PPM-DU was deployed at a depth of 3500 m in May 2014 and operated until July 2015. Data taken during that time was analysed by the collaboration including intra-DOM and inter-DOM time calibration to which the author contributed significantly. In addition, a data/Monte Carlo comparison of high-level coincidences and muon reconstruction was performed. The results were published in [36]. Figure 12.1 shows a schematic drawing of the PPM-DU. It is anchored at the sea-bed and pulled upwards by submerged buoys. The DOMs are mechanically connected by Dyneema® ropes. Data and power are transferred via the vertical electro-optical cable VEOC. The vertical distances between the DOMs are roughly 36 m. DOM1 and DOM2 were equipped with ETEL D783KFLA PMTs and DOM3 with Hamamatsu R12199 PMTs with larger effective area. DOM3 was developed and assembled at ECAP by O. Kalekin with contributions by the author. As shown in this chapter, the time calibration of the PMTs in each DOM as well as the time calibration between DOMs can reach nanosecond precision, thus fulfilling the requirements for event reconstruction.

12.1 Intra-DOM calibration

For the time calibration, auxiliary algorithms included in the official software framework *Jpp* were used. They consist of a coincidence finder which stores for each DOM independently the coincidences for all PMT combinations and time differences in a certain time window in a two-dimensional histogram. A second script reads the data from these histograms, again independently, and performs the global fit described in Section 11.1. The optimal parameters for the PMT time offsets, the relative efficiencies and a measure of the PMTs' time spreads are stored in respective histograms. The time offsets relative to the mean of all PMTs of each DOM, determined from an example run (run 1664) are shown in Figure 12.2. For most PMTs, deviations from the mean lie in the range of ± 10 ns, which can easily be explained by differences in transit times or delays in the signal processing (see Section 13.3). Efficiencies are normalised to the maximum efficiency. It is clearly visible that the efficiencies of the PMTs of DOM3 are significantly larger compared to those of DOM 1 and

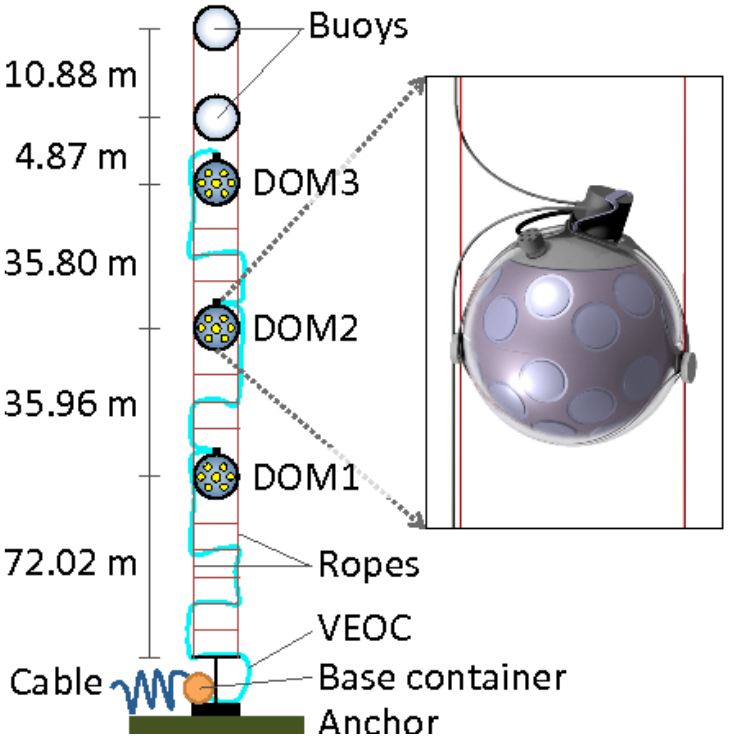

Figure 12.1: *Schematic of the PPM-DU deployed at the Capo Passero site. It consists of a base container connected to the DOMs by Dyneema® ropes. The power supply and data transfer is handled by the vertical electro-optical cable VEOC. Figure taken from [36].*

DOM 2, which can be attributed to the larger effective area of the Hamamatsu PMTs compared to the ETL PMTs. In addition, the reflector rings used in DOM3 also have an increased area compared to the ones used in DOM1 and DOM2. Two PMTs, one in DOM2 and one in DOM3, have an efficiency of zero as they were not functional during the example run. The fact that they still have a relative time offset is an artefact of the minimisation procedure.

In order to verify the accuracy and long-term stability of the time calibration, several runs distributed over the active time of the PPM-DU were analysed to determine the respective time offsets. The result is shown in Figure 12.3, revealing overwhelming stability in the sub-nanosecond level over a period of more than half a year for all PMTs, which are represented by different colours.

An investigation of the total amount of genuine twofold ^{40}K coincidences also shows the superior detection efficiency of DOM3. The number of twofold coincidences in a 20 ns time window for each PMT combination was summed up and the rate of random twofold coincidences was subtracted. The total genuine twofold ^{40}K rate was calculated for all three DOMs for the example run. Figure 12.4 shows the angular distribution of the rate of genuine twofold ^{40}K coincidences as well as the respective integral for different runs as a function of the date the run was taken. Both plots show the enhanced efficiency of DOM3, resulting in an increased rate. Furthermore, the rates are quite stable over the course of several months and no systematic efficiency loss is visible. Mean values (standard deviations) of genuine twofold ^{40}K rates for the runs shown, leaving out the two

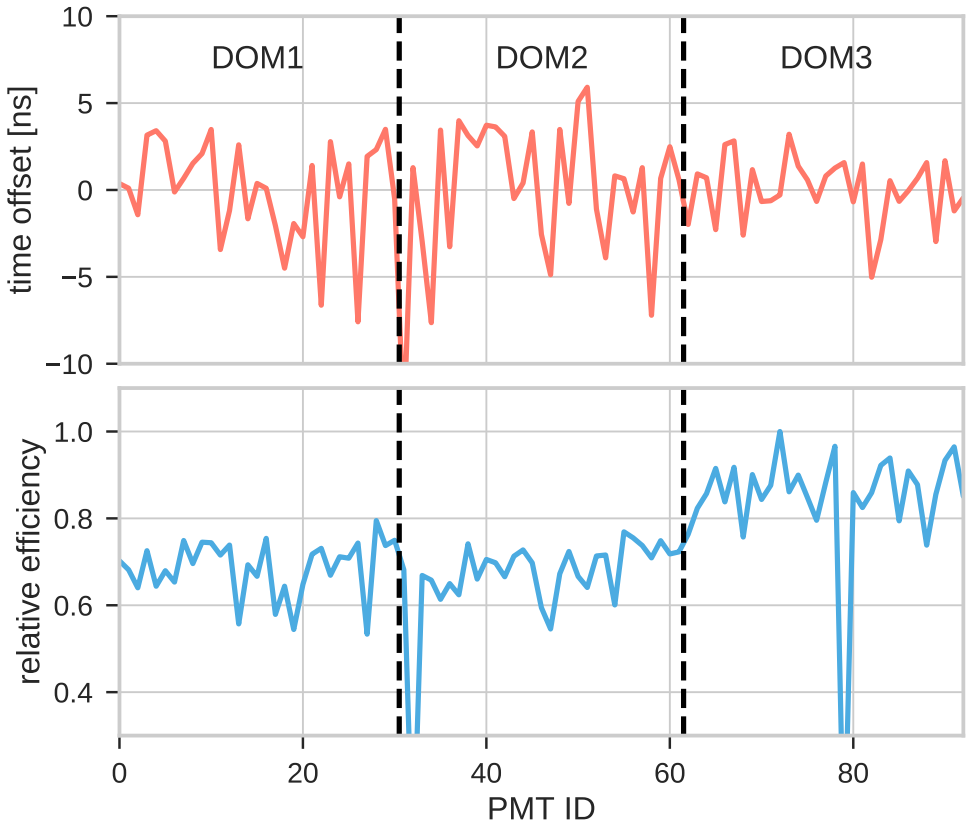

Figure 12.2: *Relative time offsets (top) and efficiencies (bottom) of all three DOMs of the PPM-DU determined from the example run. For most PMTs, time offsets lie between ±10 ns of each other; the mean value for each DOM is set to zero. Efficiencies are relative to the PMT with the largest efficiency and are significantly larger for DOM3 where both the PMTs (Hamamatsu) and the reflector rings have larger effective areas.*

outliers of DOM2 are:

DOM1: 307.2 Hz (3.8 Hz)
DOM2: 272.7 Hz (3.7 Hz)
DOM3: 462.9 Hz (8.3 Hz)

The ratio between the rates of DOM3 and DOM1 (DOM2) is 1.51 (1.70). These ratios can be used to calculate the ratio of the detection efficiencies, due to different effective areas, of the Hamamatsu and ETL PMTs used in the DOMs. Assuming equal effective areas for all PMTs in each DOM, the single PMT efficiency goes with the square root of the total two-fold coincidence rate of a DOM. That means that the PMT-reflector combination in DOM3 has, on average, a 22% larger effective area than that in DOM1 and even 30% larger than DOM2. The smaller rates in DOM2 compared to DOM1 can at least partly be explained by the one dysfunctional PMT in DOM2. Since there is a

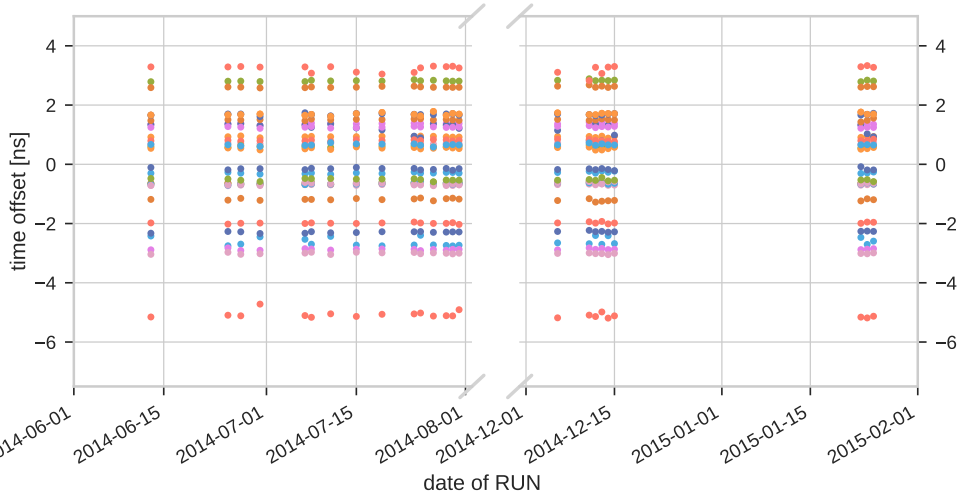

Figure 12.3: *Stability of the PPM-DU time calibration of DOM3 over various runs. Different colours represent different PMTs. Variations are below 1 ns.*

dysfunctional PMT in DOM3 as well, the comparison between DOM2 and DOM3 is supposed to be more accurate.

In summary, it can be said that timing and efficiency of the PPM-DU are very stable over periods of months. The time calibration works very well and a sub-nanosecond precision can be achieved.

12.2 Inter-DOM time calibration

For the inter-DOM time calibration, several nanobeacon runs, with the nanobeacon on DOM1 being active, were taken over a period of roughly two months. They were analysed using the method described in Section 11.2. The time difference between DOM1 and DOM2 as well as the time difference between DOM1 and DOM3 were extracted from the data. Searching in every event for the time difference between the first hit on DOM1 and the first hit on DOM2 or DOM3 and correcting for the respective light travel times in water leads to a Gaussian-like distribution. This distribution was fitted with a Gaussian function for each run and DOM combination. The time difference between DOM1 and DOM2 for one example run (run 103) is shown in Figure 12.5 (top). The stability of the inter-DOM time calibration for DOM1-DOM2 and DOM1-DOM3 over the course of two months is shown in the bottom plot. While the time difference between DOM1 and DOM2 is very stable with a standard deviation of roughly 0.9 ns, there are major jumps in the time difference between DOM1 and DOM3. Those jumps can be attributed to different power cycles, which are expected to deteriorate the time calibration to the extent observed, as no complete time synchronisation was implemented in the PPM-DU. Within the same power cycle the time calibration was, however, very stable.

The results presented in this section show that a nanosecond precision can also be reached for the inter-DOM time calibration using the nanobeacon. However, there are additional methods of calibrating the timing between the DOMs of a string, e.g. using test setups in the lab where time-synchronised lasers illuminate the different DOMs, or atmospheric muon reconstruction in the lab

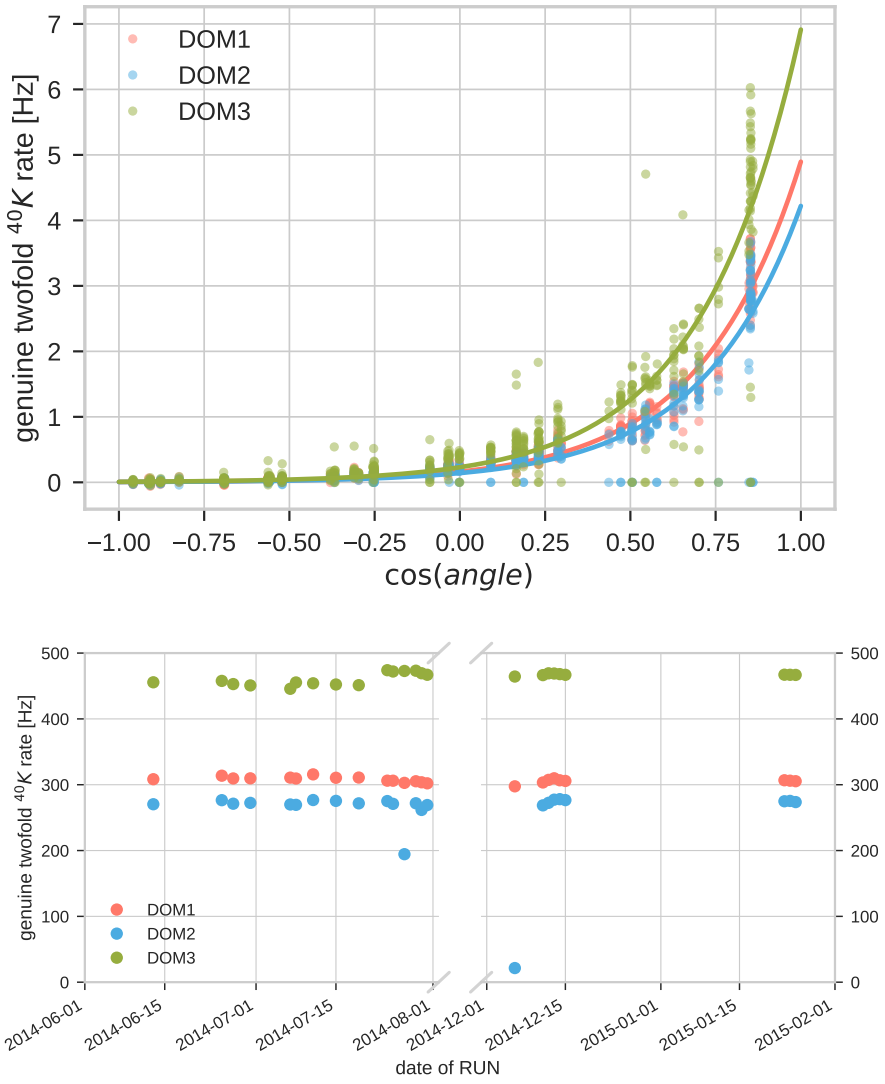

Figure 12.4: *Angular distribution (top) and long-term stability (bottom) of genuine twofold ^{40}K rates.*

or in situ.

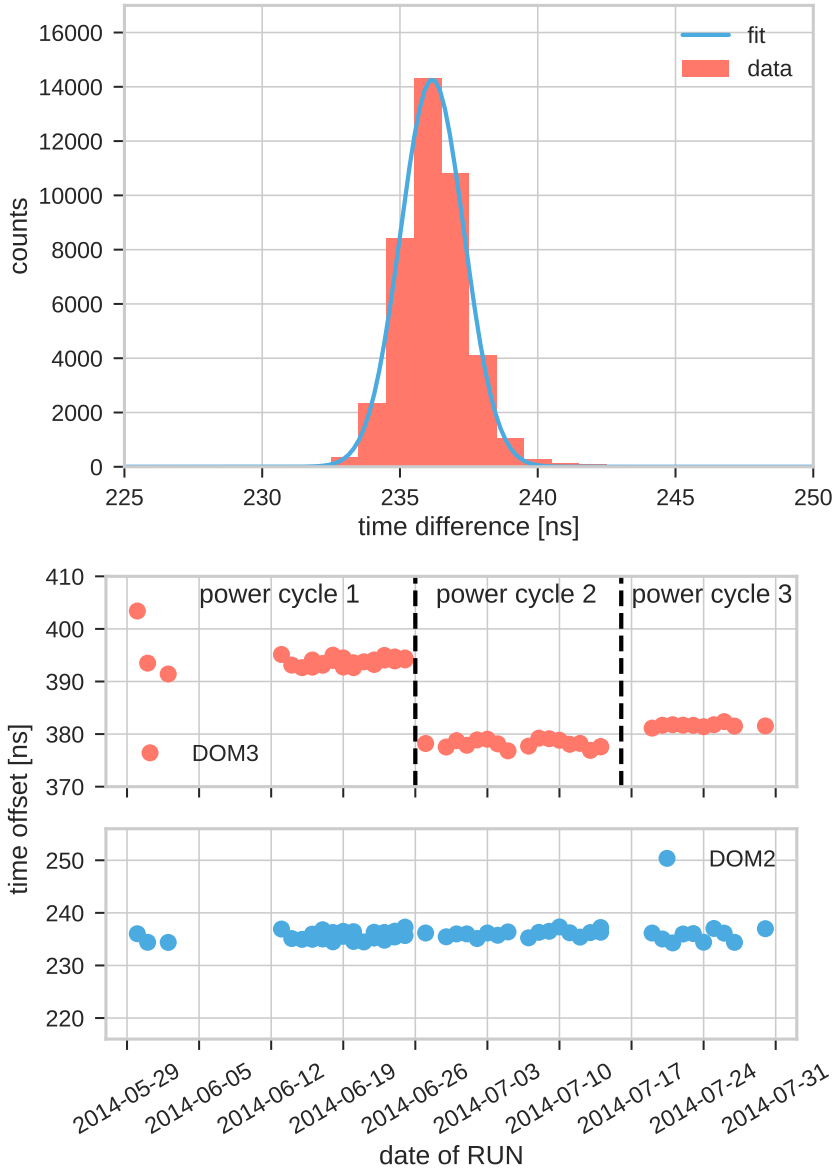

Figure 12.5: *Time difference between DOM1 and DOM2 for all events in one nanobeacon run (top) and stability of the time calibration over several runs over the course of two months for DOM1-DOM2 and DOM1-DOM3 (bottom).*

Chapter 13

Detection unit

In December 2015, the first full detection unit (DU) of KM3NeT was successfully deployed at the Italian site, 100 km off the cost of Sicily. Anchored 3500 m deep at the seabed, the DU consists of 18 DOMs with a vertical spacing between the DOMs of roughly 36 m. The DU spans an overall height of approximately 700 m. In May 2016, a second DU was installed with a horizontal spacing of roughly 100 m to the first DU. With the integration procedures and components being standardised, all DOMs of the two DUs are considered to be very similar in performance. As optical sensors, Hamamatsu R12199 PMTs are used (see Chapter 6).

In this chapter, a comparison between data taken with the first DUs and Monte Carlo simulations of ^{40}K-induced twofold coincidences is presented. In addition, a comparison of PMT efficiencies measured in the lab and those derived in situ from ^{40}K rates is made. The influence of the structures of the DOMs on the rate of ^{40}K coincidences measured with the individual PMT combinations is also investigated, as well as the influence of the PMT high voltage on single-hit rates, twofold ^{40}K rates and the timing of the PMTs.

13.1 Comparison of data and Monte Carlo simulation

The official KM3NeT DOM Monte Carlo simulation is a GEANT4-based ray tracing simulation described in [52,55]. It models the KM3NeT multi-PMT DOM with great detail and also includes the simulation of the DOM response to the Cherenkov light produced by ^{40}K decays in sea water. An apparent difference between the simulation setup and a real DOM in water is the absence of the titanium collar and other auxiliary structures outside of the DOM. The resulting consequences are discussed in this section.

Since the simulation result was available as a listing of hits produced by ^{40}K decays, it had to be transformed into the KM3NeT data format in order to allow for a reasonable comparison. For this purpose, the hits were written into timeslices, and random background was added. After that, local coincidences were calculated with the method described in Section 11.1. The two-dimensional histogram of twofold coincidences with the time differences between hits on the one axis, and the PMT combination ID, as shown in Table 11.1 in Section 11.1 on the other axis can then be further analysed. For the analysis in this chapter, the method of independent fits and minimisations described in Section 11.1 was used, since it allows better insight and control over the individual fitting steps compared to the global fit.

The angular distribution (here cosine of angle between PMTs in each combination) of ^{40}K rates

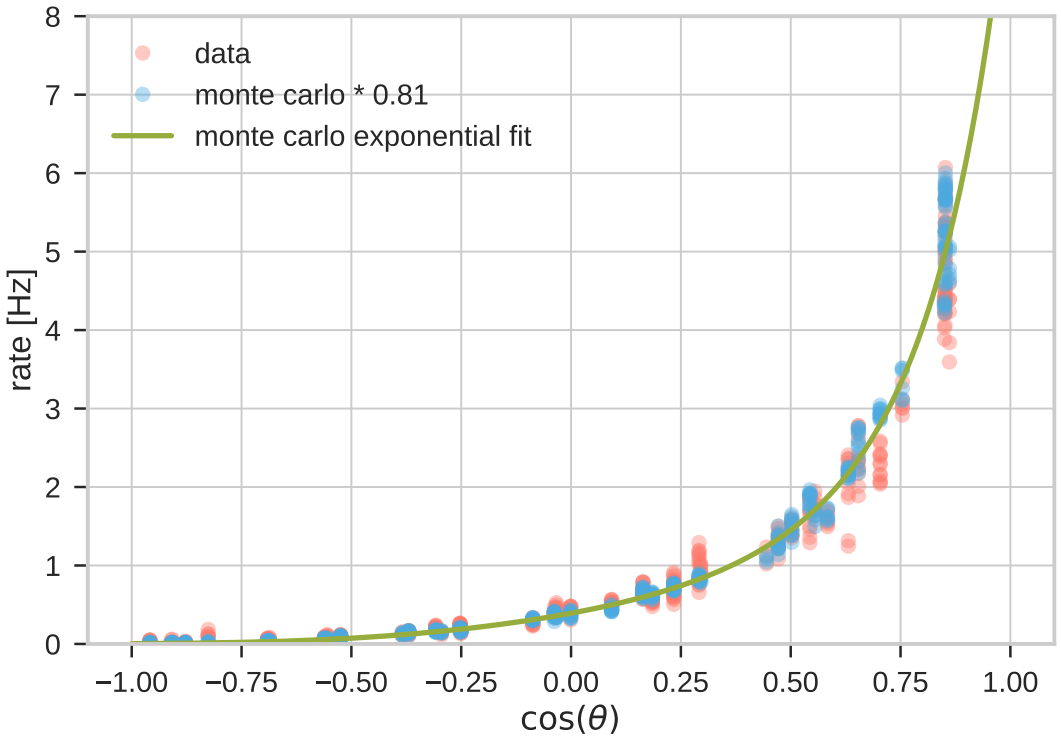

Figure 13.1: *Comparison of angular distribution of ^{40}K rates of data (red dots) and Monte Carlo simulation (blue dots). Monte Carlo is scaled by a factor of 0.81 to match the data rates. In addition to a wider statistical spread of the data rates for the individual angles compared to the simulation, systematic differences can be explained by the absence of the titanium collar and other auxiliary structures. An exponential fit to Monte Carlo is shown in green.*

is shown in Figure 13.1 in comparison to a representative DOM of one of the two DUs. The Monte Carlo rates are scaled to match the data. Up to a constant scaling factor data and Monte Carlo are in good agreement with regard to the shape of the angular distribution of ^{40}K rates. This constant scaling factor can be explained by the collection efficiency of the PMTs, that is not accounted for in the simulation. Systematic differences originate from the discrepancies between the Monte Carlo and experimental setups. As shown in Section 13.2, the systematic differences are mainly due to the absence of the titanium collar in the simulation. The exponential fit shown as green line in Figure 13.1 represents nominal rates for each angle that would be produced by a PMT combination where both PMTs have the nominal efficiency. Deviations from the fit originate from different efficiencies of the PMTs as well as from influences of structures in the DOM.

The nominal values extracted from the fits are used in the following to investigate the systematic deviations of the coincidence rates measured with the first two detection units from the Monte Carlo rates.

13.2 DOM structure and efficiency investigations

The original idea of a comparison of quantum efficiencies, measured in the lab (see Section 6.2.1) and the efficiency determined by coincidences measured from ^{40}K decays was realised with PPM-DU data. This was possible as one DOM of the PPM-DU was equipped with Hamamatsu PMTs that were also measured in the lab. Unfortunately, no correlation between lab and in-situ determined efficiencies was found. It was therefore assumed that auxiliary structures, like the titanium collar have a considerable impact on the ^{40}K rates. Assuming equal efficiencies in PMTs of two different combinations with equal angular distance, the measured ^{40}K-induced twofold rates can be different if for instance a part of the titanium collar has a shadowing effect for one but not the other combination. As a consequence, different efficiencies are wrongly assigned.

Rate and efficiency correlation between different DOMs

In order to test this assumption, the ^{40}K rates for all PMT combinations, R_c, and the exponential fit values of the angular distribution of the scaled Monte Carlo simulation for each angle between the PMTs of all combinations, F_c, were calculated. The ratio $r = R_c/F_c$, being an array with 465 values (one for each PMT combination), was calculated for all DOMs where all PMTs were active during an example run (run 5162, detector id 14). Figure 13.2 (left) shows the correlation of the ratio r between the DOMs of all DOM combinations (DOM$_i$, DOM$_j$). In addition, the correlation coefficient is calculated for each DOM combination and is shown in a one-dimensional histogram (right). Overall, a strong correlation is observed with a mean value of roughly 0.8, confirming the assumption that the auxiliary structures outside of the DOM have a significant impact on the ^{40}K rates. This implies that the overall PMT efficiencies are not represented solely by those derived in

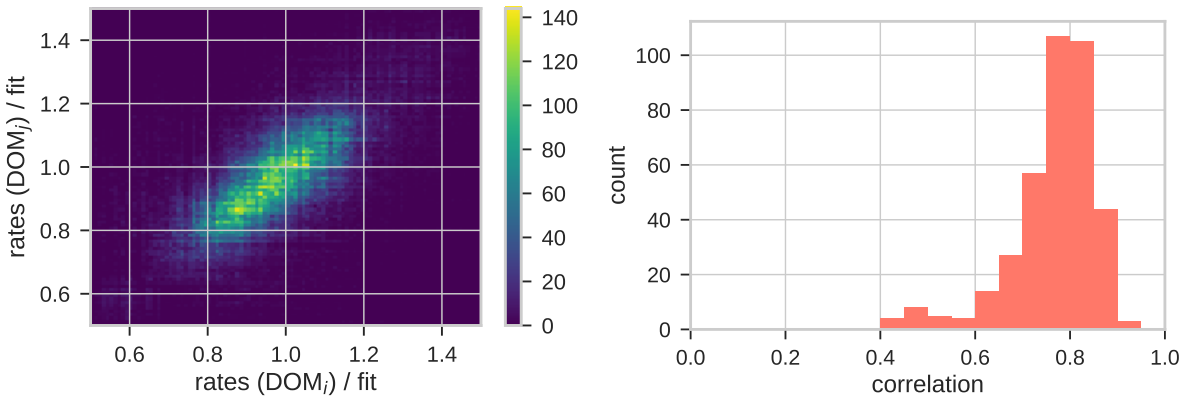

Figure 13.2: *Correlation plot of the ratios of the measured ^{40}K rates and fitted Monte Carlo rates for all DOM combinations (left) and calculated correlation coefficients (right). A strong correlation of roughly 0.8 can be identified.*

situ from ^{40}K rates (with the minimisation procedure shown in Equation 11.7 in Section 11.1), but are also influenced by the structures of the DOM. This statement is confirmed by the strong correlation found for the efficiencies derived in-situ for all DOM combinations as shown in Figure 13.3.

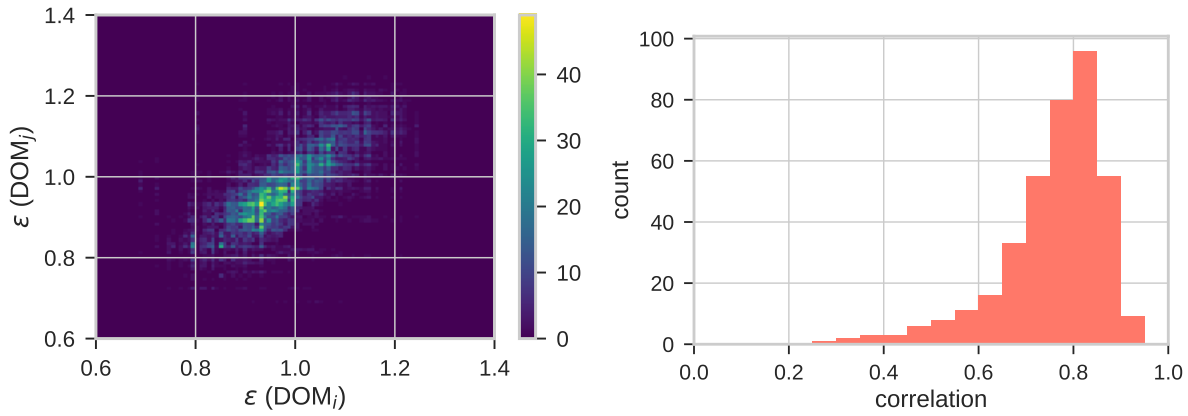

Figure 13.3: *Correlation plot (left) and histogram of correlation coefficients (right) of the efficiencies derived from the in-situ measured ^{40}K rates.*

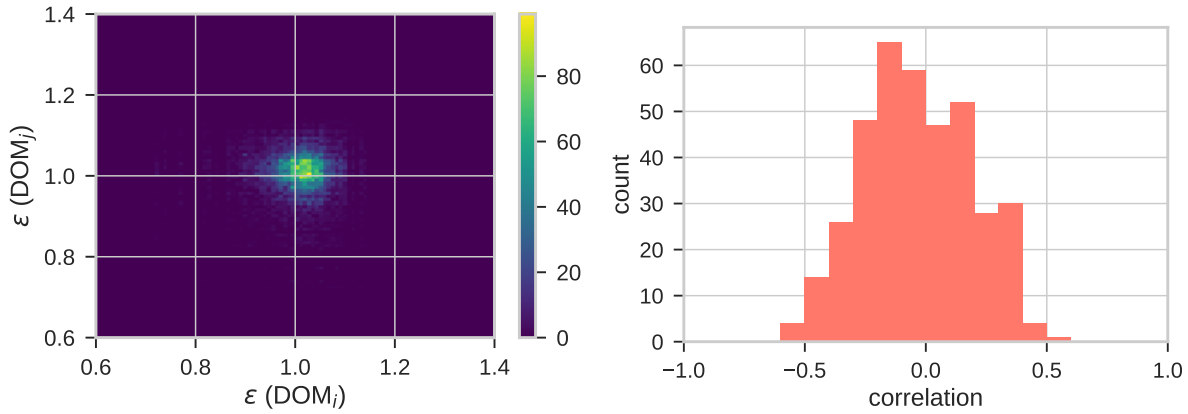

Figure 13.4: *Correlation plot (left) and histogram of correlation coefficients (right) of the efficiencies derived from the in-situ measured ^{40}K rates after structure correction.*

Correction for structure effects

In order to get a more realistic measure of the efficiencies of the PMTs, the ^{40}K rates have to be corrected for their structure-induced effects. Since the DOMs were built with standardised procedures and components, it can be assumed that the structure-induced effect on the ^{40}K rates is similar for all DOMs. Hence, the mean values of the 465 ratios r over all DOMs, r_m, are calculated and can be considered the mean structure effect on the ^{40}K rates. The rates can then be corrected for this effect in order to get the structure-corrected rates R'_c

$$R'_c = \frac{R_c}{r_m} .$$

Figure 13.4 shows the correlation of efficiencies for different DOMs after the structure correction was applied to the rates. The distribution of correlations for the different DOM combinations is centred around zero; thus no correlation can be identified.

Since the mean structure effect is supposed to originate mostly from the titanium collar, all next

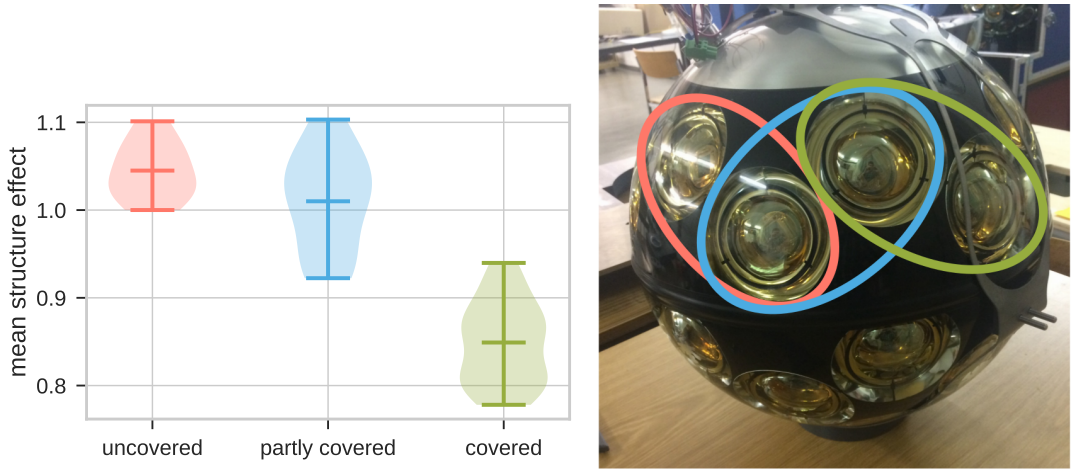

Figure 13.5: *Mean structure effect r_m for the next neighbour PMT combinations divided into groups of uncovered (red), partly covered (blue) and covered (green) (left) and examples of combinations in the groups shown on a photograph of a DOM (right).*

neighbour PMT combinations were divided into three groups. Uncovered combinations, where none of the PMTs has the titanium collar in its field of view; partly covered combinations, where one of the PMTs has the titanium collar in its field of view; and covered combinations, where both PMTs have the collar in their fields of view or the collar even passes between both PMTs. For the three groups of combinations, the mean structure effect r_m and an illustration of the groups on a photograph of a DOM are shown in Figure 13.5. With a mean structure effect of roughly 1.05, the uncovered PMT combinations have the largest ^{40}K rates, followed by the partly covered combinations with a value of approximately 1.00. The covered combinations, where the shielding of the titanium collar is maximal, have a mean structure effect value of 0.85. These values confirm the significant influence of the titanium collar on the mean structure effect.

Figure 13.6 shows the angular distribution of ^{40}K rates compared to the exponential fit to the Monte Carlo simulation for different correction steps applied. From top left to bottom right:

- uncorrected rates R_c ,
- efficiency-corrected rates, where the efficiencies were adjusted to minimise the distance of the data points from the fit (see Section 11.1),
- mean structure-corrected rates R'_c, and
- rates first corrected for the mean structure effect and then corrected for the efficiencies of the PMTs.

The efficiency correction reduces the mean deviation of the data points from the fit from 0.154 Hz to 0.099 Hz, but systematic differences remain. Correcting for the mean structure reduces the mean deviation to 0.068 Hz. The remaining differences can be attributed to statistical fluctuations of the PMT efficiencies. When applying both, the mean structure and efficiency correction, the best result is achieved. The mean deviation of the data points from the fit is reduced significantly to 0.025 Hz.

According to the results presented above, the efficiencies derived after the mean structure correction reflect the real PMT efficiencies much better. Since there is unfortunately no overlap in the

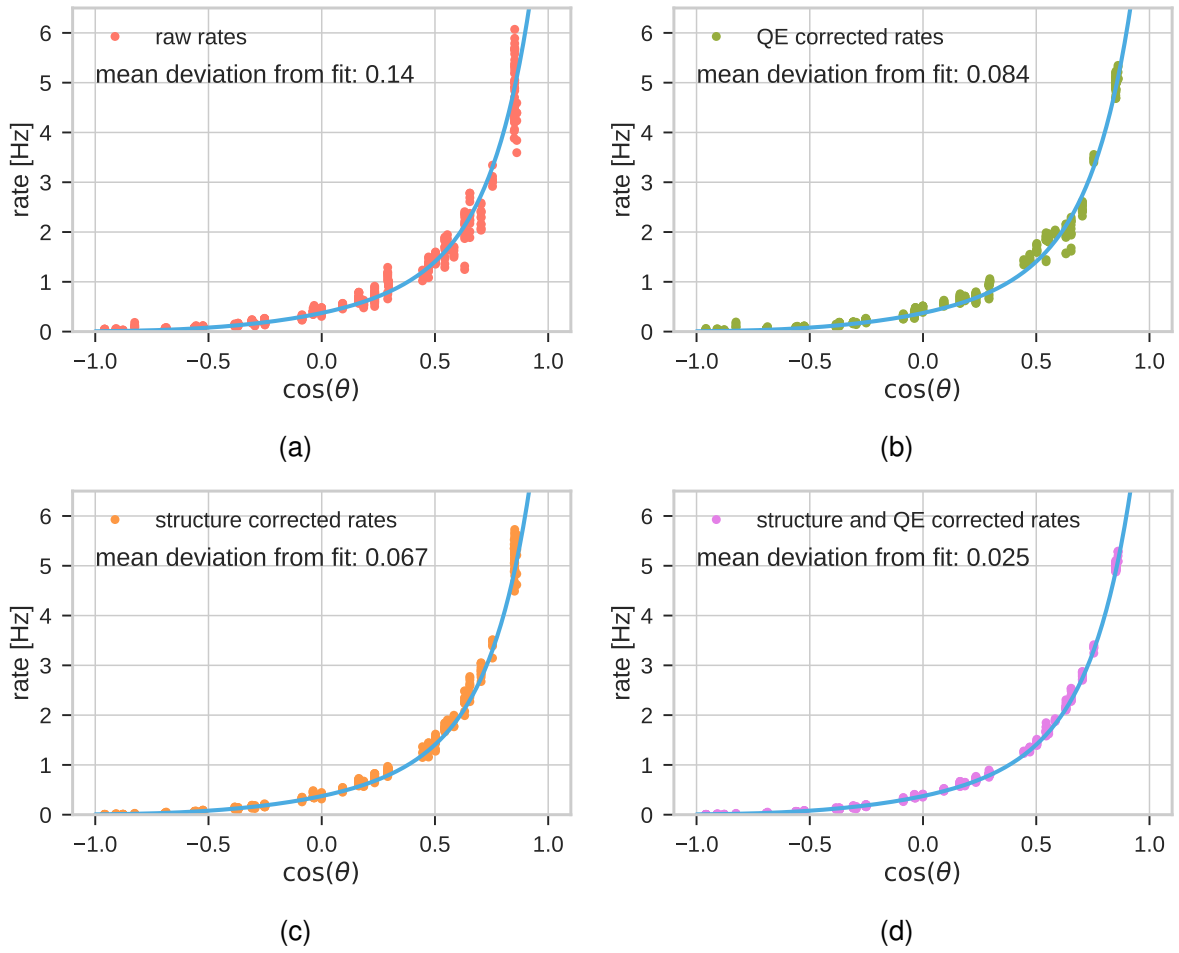

Figure 13.6: *Angular distribution of ^{40}K rates (points) compared to the fit to the Monte Carlo simulation (line) before and after the different correction steps: (a) raw rates without any correction R_c; (b) efficiency-corrected rates as described in Section 11.1; (c) mean structure-corrected rates R'_c; (d) mean structure- and efficiency-corrected rates. The mean deviations of the data points from the fit are indicated in the plots and is decreasing from top left to bottom right.*

batch of PMTs measured in the lab and PMTs integrated in the DOMs of the first two detection units, only statistical statements can be made. For this purpose, all efficiencies derived from the ^{40}K rates measured before and after the structure correction and the relative integrated quantum efficiency measured of 200 PMTs in the lab (see Section 6.2.1) are shown in Figure 13.7. The relative standard deviations of their distributions are 9% before structure correction and 5% after the correction, being in good agreement with that of the lab measurement of also 5%. This suggests that the variations in the in-situ determined efficiencies are dominated by the variations of the PMT quantum efficiencies. It can thus be concluded that the efficiencies derived in situ after the structure correction reflect the real PMT quantum efficiencies with high precision. As a cross-check it would, of course, be helpful to integrate PMTs with lab-measured quantum efficiencies in future detection units.

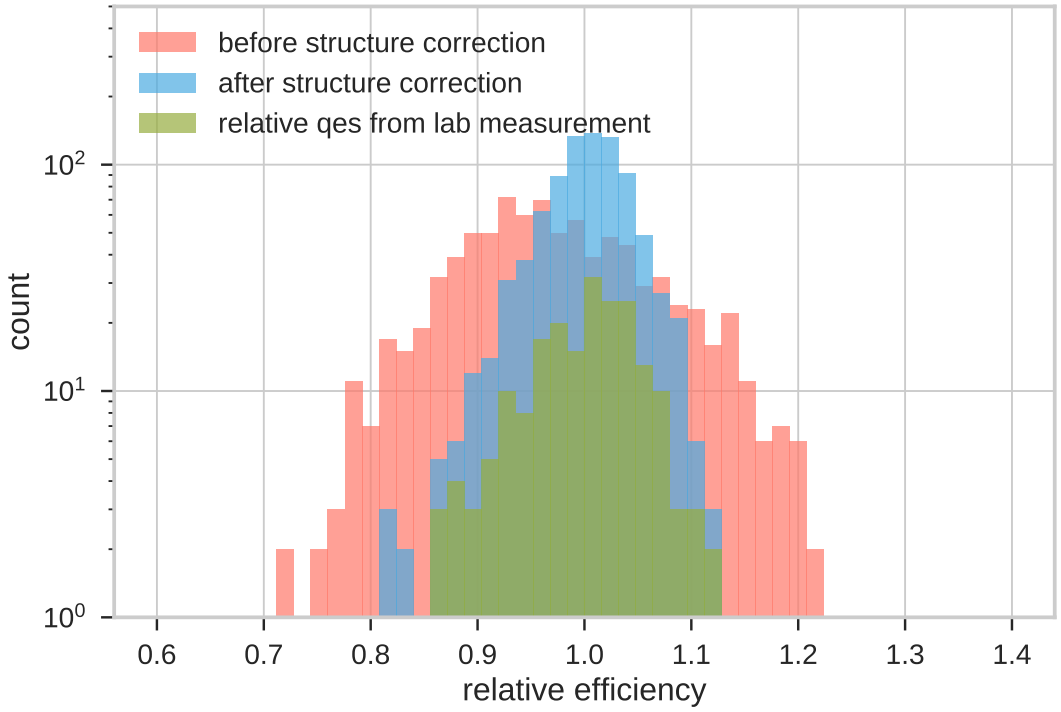

Figure 13.7: *Distribution of PMT efficiencies before and after correction for the mean structure effect as well as relative quantum efficiencies from lab measurements.*

Effects of glass sphere quality on the detection efficiency of a DOM

As shown in Section 7.1, the transmittance of glass spheres produced in one batch does not vary a lot. It is, however, well known and confirmed by the manufacturer that the quality of the glass changes over longer periods of time. In addition to the maximum transmittance, the variation of the spectral cut-off, which is located between 300 and 350 nm, is crucial. Unlike the Cherenkov spectra reaching the DOMs resulting from muon or shower events which do not contain many UV-photons since most of them are absorbed during their propagation through the water, the detected spectrum of the ^{40}K-induced Cherenkov photons has a significant share of UV-photons. This is due to the fact that most of the decays occur within a maximum distance of 5 m to the DOM [39]. This UV content may have a significant influence on the sensitivity determination of DOMs with different peak transmittances and transmittance cut-offs. Moreover, the borosilicate glass used for the glass spheres contains a considerable amount of potassium oxide (K_2O) and a natural contamination with ^{40}K is expected. A variation in the K_2O content and in the ^{40}K contamination might thus have an effect on the measured genuine twofold ^{40}K rate on which the analysis is based.

In order to investigate these effects, the mean quantum efficiency after structure correction was calculated for all DOMs. It is shown as a function of the glass sphere manufacturer serial number in Figure 13.8. The data points are divided into two batches, indicated by their large difference in serial number. A slightly lower mean efficiency can be identified for the second batch (shown in

blue) compared to the first batch (shown in red). Given the categorisation into two batches and leaving out the outlier with a mean efficiency below 0.93, the statistical significance s of the mean values being different can be calculated:

$$s = \frac{\epsilon_{m,2} - \epsilon_{m,1}}{\sqrt{\Delta\epsilon^2_{m,1} + \Delta\epsilon^2_{m,2}}} = 3.3\,, \tag{13.1}$$

where $\epsilon_{m,1}$ and $\epsilon_{m,2}$ are the mean efficiency values of the first and second batch, respectively, and $\Delta\epsilon^2_{m,1}$ and $\Delta\epsilon^2_{m,2}$ are the respective statistical errors on the mean values.

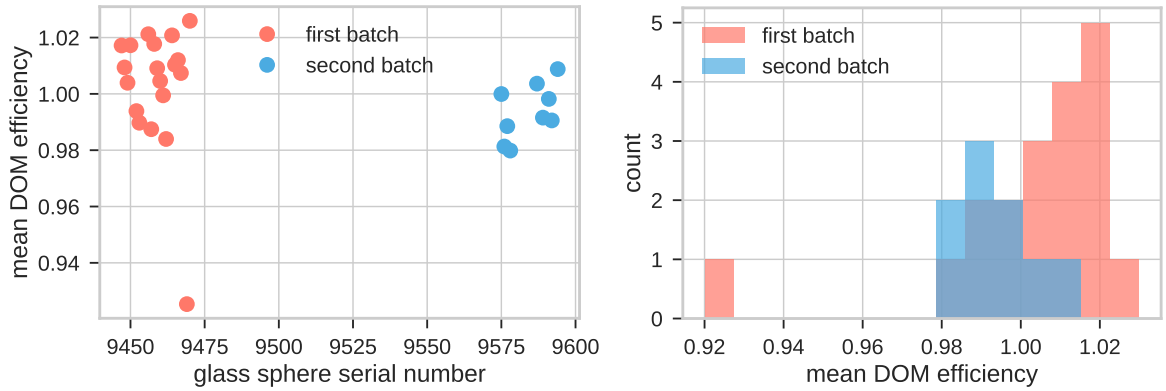

Figure 13.8: *Mean DOM efficiencies as a function of the glass sphere serial number (left). Distribution of the mean DOM efficiencies for two different glass sphere batches (right).*

Conclusion

The results presented in this section show the influence of auxiliary structures of the DOMs on the measured ^{40}K rate. By combining the rates of different DOMs, this effect can be calculated and efficiently corrected for. After the correction, the PMT efficiencies can be determined with high precision and even glass property fluctuations on the 1-2% level can be identified. These fluctuations are most likely caused by a combination of the changing transmittance and ^{40}K contamination of the borosilicate glass. In order to confirm the results, detection units deployed in the future should at least partly be equipped with PMTs with quantum efficiencies measured in the lab.

13.3 Influence of high-voltage variations on PMT parameters

During the operation time of the first DU, runs were taken with varying high voltages applied to the PMTs. Eleven runs[1] with voltages from -125 to +125 V compared to the nominal high voltage of each PMT were recorded in step sizes of 25 V. These runs are used to analyse the influence of the

[1] The runs 2307, 2309, 2311, 2313, 2315, 2317, 2319, 2321, 2323, 2325 and 2327 with detector id 7 were used.

high voltage on different parameters like the single-hit rates and twofold ^{40}K rates, as well as on the timing parameters of the PMTs determined by the fitting procedure for the intra-DOM calibration as described in Section 11.1. As the characterisation process of PMTs in the lab also includes data taken with different high voltages in order to determine the nominal high voltage for a fixed gain as presented in Section 6.2.2, this investigation is also performed with lab data. In addition, a comparison to the in-situ measurements is performed. Note that the PMT high voltages in KM3NeT are of negative polarity. In the context of this section, the nominal high voltage is regarded as its absolute value, leading to an increase when adding 125 V and to a decrease when subtracting 125 V.

Single-hit rates were read from the summary data and the mean value over all PMTs in all DOMs was calculated for each high-voltage setting. The twofold ^{40}K rates were determined by summing the areas below the Gaussian fits of all PMT combinations with an angle between their pointing directions of less than 90° in order to avoid badly working fits. A mean value for all DOMs was calculated for each high-voltage setting. The widths of the Gaussian fits of all PMT combinations were used to calculate the widths corresponding to each PMT, as explained in Section 11.1. The time offsets of all PMTs were calculated from the mean values of the Gaussian fits, as also explained in Section 11.1.

The relative PMT rates were determined from the lab measurements by counting the hits with charges above 0.3 times the mean single photoelectron charge with applied nominal high voltage. This number of hits is divided by the total number of hits. Since with increased (decreased) applied high voltage, the mean charge increases (decreases) and more (less) hits are above the threshold, the number of hits counted as signal increases (decreases) and so does the rate. The transit times decrease with increased high voltage, as the acceleration of the electrons between the photocathode and the first dynode as well as between the dynodes is increased. The transit time spreads also decrease, as with larger high voltage the flight paths of the electrons are straighter and their variation is smaller. Figure 13.9 illustrates the effects described above by showing the high-voltage-dependent charge spectra and timing parameters for a PMT measured in the lab.

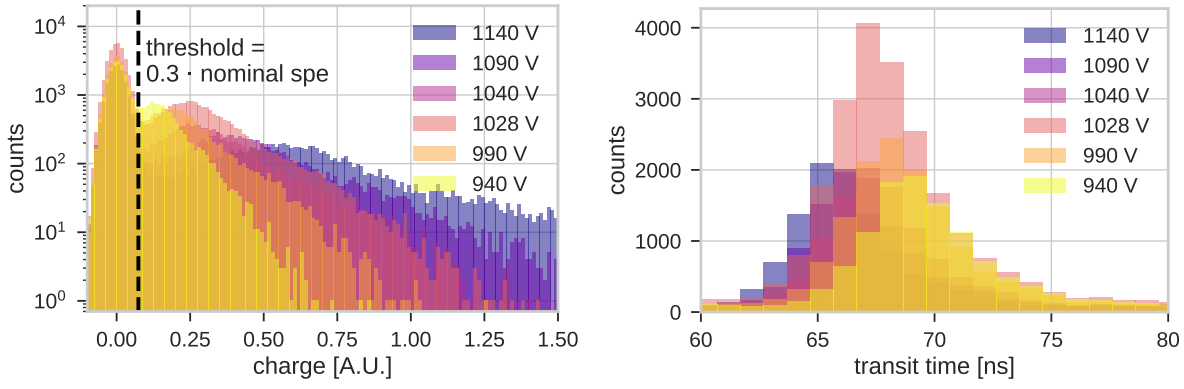

Figure 13.9: *High-voltage-dependent single photoelectron charge spectra (left) and transit time histograms (right).*

High-voltage-dependent rates

Figure 13.10 shows the trend of single-hit rates and twofold ^{40}K rates determined from the in-situ measurements as well as their comparison to the relative rates determined from measurements in the lab. Since the PMTs were measured with different high voltages in the lab, a linear interpolation between the measuring points was performed, and a mean value over all PMTs for the interpolated values was calculated in a range between nominal high voltage - 125 V and nominal high voltage + 125 V. These interpolated values and their errors are represented by the red and blue bands in Figure 13.10 (right). While the overall relative rate change of in-situ determined single-hit rates and relative PMT rates measured in the lab are in good agreement, the change in bioluminescence and thus the single-hit rates causes fluctuations over a large part of the measured high-voltage range. At first sight, the relative twofold ^{40}K rates are expected to follow the square of the relative PMT rates, since for instance a relative rate change from 1 to 0.9 has to be applied to two PMTs, resulting in a change from $1 \cdot 1$ to $0.9 \cdot 0.9 = 0.81$. In reality, the composition of the ^{40}K hits as to their number of photoelectrons has to be considered. Since the fraction of hits with two or more photoelectrons is larger for twofold ^{40}K hits compared to single hits and hits with two or more photoelectrons have a significantly lower chance to fall below the threshold when reducing the high voltage, the real shape follows a power law with an exponent of smaller than two. The relative PMT rates to the power of 1.5 shown in Figure 13.10 fit the relative in-situ ^{40}K rates quite well. Possible further effects influencing the high-voltage-dependent rates might be found in the charge-to-voltage conversion performed in the KM3NeT active base and are worth to be investigated in the future.

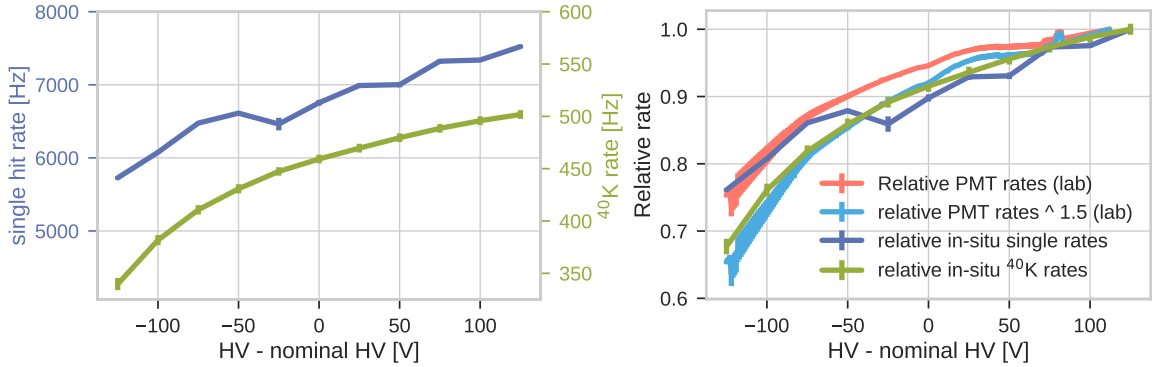

Figure 13.10: *Single-hit rates per PMT (blue) and twofold ^{40}K rates per DOM (green) as a function of the applied high voltage minus the nominal high voltage (left) and a comparison of the relative rates (rates divided by the maximum rate) determined in situ and in the lab (right). The single-hit rates are averaged over all PMTs and the ^{40}K rates are averaged over all DOMs. The PMT rates measured in the lab are interpolated, since different PMTs were measured with different high voltages, and averaged over a sample of eight measured PMTs.*

High-voltage-dependent PMT timing spread

The results of the high-voltage-dependent in-situ and lab-measurement based timing spread analysis are shown in Figure 13.11. The mean PMT sigmas as well as the standard deviation of the time

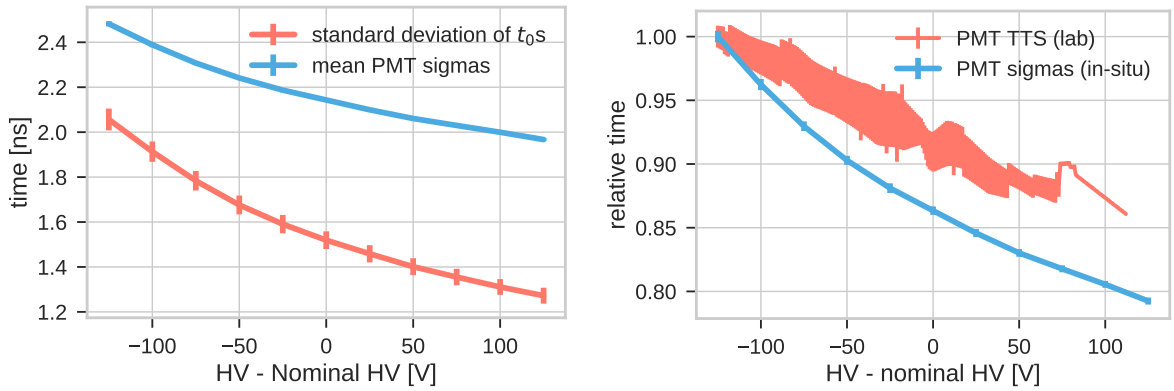

Figure 13.11: *Mean PMT sigmas and standard deviation of time offsets as a function of the applied high voltage determined in situ from twofold ^{40}K hits as explained in Section 11.1 (left) and comparison of the relative transit time spread changes with high voltage of in-situ and lab measurements (right). The unregular shape of the PMT TTSs measured in the lab can be explained by the averaging over the different PMTs where the data had been interpolated and the limited statistics in certain high-voltage ranges.*

offsets determined from the twofold ^{40}K rates (as presented in Section 11.1) are shown as a function of the applied high voltage. The comparison of in-situ- and lab-based measurements[2] shows a significantly steeper decrease in the in-situ determined sigmas compared to the transit time spreads determined in the lab. The in-situ changes can thus only partly be explained by the change in the transit time spreads of the PMTs, and a closer look into the effects caused by the charge-to-voltage conversion of the active base is needed. The voltage-based signal in the active base is formed by an RC circuit, where the overall charge is expected to have a significant influence on the rise time and thus on the time spreads between different signals. Note that the absolute sigmas determined in situ are larger than the transit time spreads of the PMTs measured in the lab, because an additional timing spread is caused by the local distribution of the ^{40}K decays which is not supposed to be impacted by high-voltage changes, however.

High-voltage-dependent PMT time offsets

The high-voltage-dependent time offsets determined in situ via the twofold ^{40}K rate distribution (as shown in Section 11.1) are compared to transit times measured for different PMTs and applied high voltages in the lab. Figure 13.12 (a) shows the relative transit time as a function of the applied high voltage for the bare PMTs measured in the lab. The expected decrease in the transit time with increased high voltage is clearly seen. It can be explained by the acceleration of the electrons in the PMT caused by the electric fields between the photocathode and the first dynode as well as between the dynodes. Increased high voltage causes increased acceleration and thus decreased transit times. Figure 13.12 (b) shows the correlation between the nominal high voltages for the first detection unit minus the high voltage of the reference PMT[3] in each DOM and the time offset of the

[2]The transit time spreads determined from lab measurements are, again, interpolated between the high voltage values measured and are shown, together with their corresponding errors, as red band in Figure 13.12.

[3]The PMT connected to channel zero of the octopus board is always used as reference PMT.

PMTs compared to the reference PMT. A linear fit to the data with a slope of -0.014 ns/V is shown as blue line. For comparison, the average of the linear fits to the lab data with a slope of -0.016 ns/V (Figure 13.12 (a)) is shown as green line. Besides the small deviation between the slopes of the lab and in-situ data, a constant offset from zero of the fit to the in-situ data can be identified. A possible explanation is the fact that the channel zero of the octopus board has a small time advantage in the signal processing compared to the other channels. All in all, the time offsets of the PMTs are mainly caused by the difference in their high voltages.

Figure 13.12 (c) shows the changes in transit time over a voltage range of 250 V as a function of the PMTs' nominal high voltages measured in the lab. A linear fit shows that the absolute transit time change over a voltage range of 250 V decreases with increasing nominal high voltage with a slope of 0.0033 ns/V. This can be explained by the acceleration of the electrons in the PMTs, which can be approximated by the acceleration a in a constant electric field E:

$$a = \frac{Q}{m} \cdot E \,,$$

where Q and m are the electric charge and the mass of the electron. Assuming a resting electron at the photocathode, the equation of motion is:

$$x = \frac{1}{2} \cdot \frac{Q}{m} \cdot E \cdot t^2 \,,$$

where x is the travelled distance and t is the travel time. Since in a homogeneous electric field, the voltage difference U is equal to the electric field times the distance, the travel time of the electron can be expressed as:

$$t = x \cdot \sqrt{\frac{2m}{QU}} \,.$$

That implies that the larger the high voltage, the smaller is the change in travelling time over a certain high-voltage range. Figure 13.12 (d) shows the change of the time offsets of all PMTs compared to the respective reference PMTs over a voltage range of 250 V as a function of the high voltage of the PMTs minus that of the reference PMT. A linear fit with a slope of 0.0097 ns/V is shown as blue line. A comparison of the lab and in-situ results shows that the PMT time offset changes cannot be fully explained by the transit time changes measured in the lab. A possible additional factor can again be found in the charge-to-voltage conversion in the active base, where different charges might result in different signal shapes, influencing the timing of the signal.

Conclusion

The results shown in this section show that the in-situ determined, high-voltage-dependent rates can be explained, to a good extent, by the high-voltage-dependent rates measured in the lab. The relation between single-hit rates and twofold ^{40}K rates however is not clear yet and has to be further investigated. It has also been shown that the time offsets of the PMTs in the DOMs mostly originate from the different nominal high voltages of the PMTs, while an additional contribution by the active base is likely. The in-situ determined time offset and time spread changes with high voltage, in contrast, cannot be explained by the behaviour measured in the lab, and the dominating influences remain unknown but might be found in the charge-to-voltage conversion in the KM3NeT active base or in the signal processing.

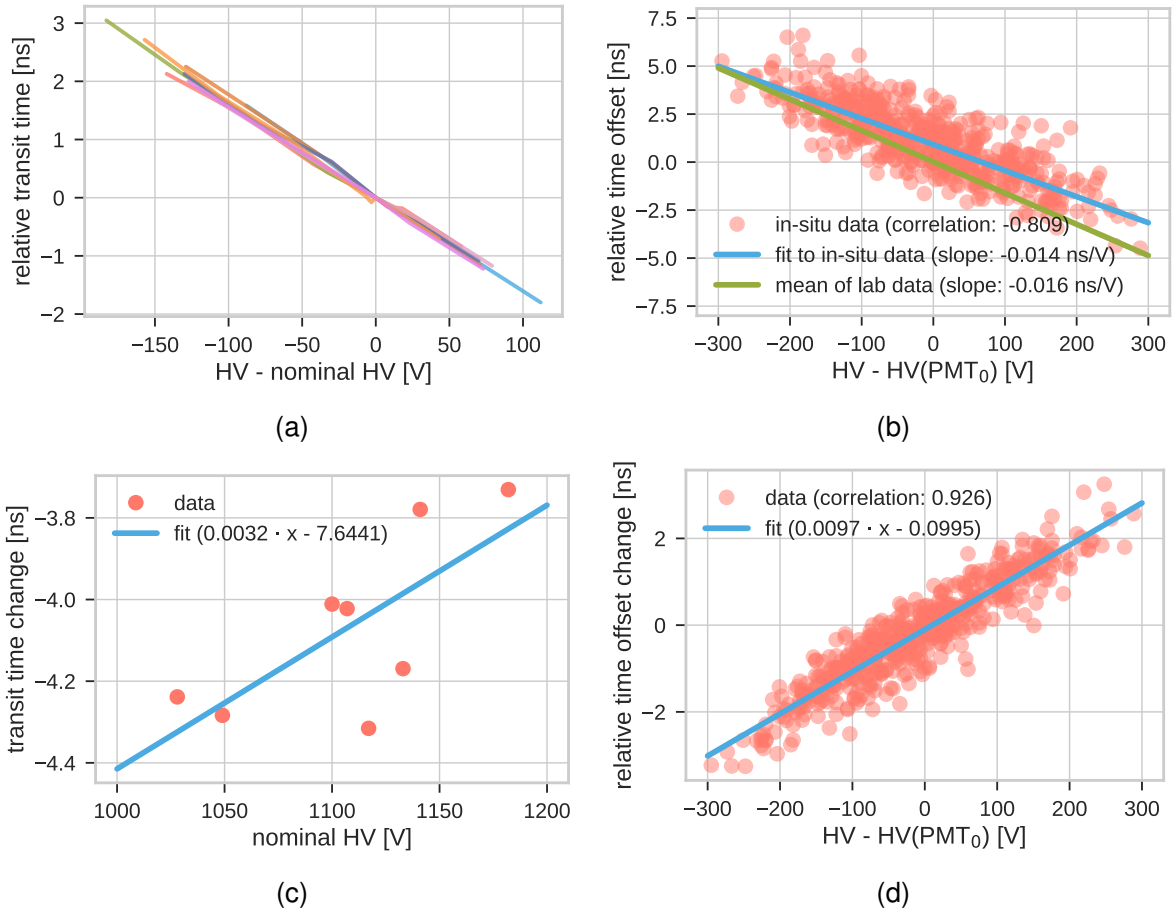

Figure 13.12: *High-voltage-dependent time offsets: (a) transit times as a function of the applied high voltage measured in the lab; (b) correlation between applied high voltage minus high voltage of the reference PMT and relative time offsets compared to the reference PMT determined from two-fold ^{40}K hits for all PMTs in the first DU. Fit to the data is shown in blue, average of PMT transit time measured in the lab is shown in green; (c) transit time change in a range of 250 V, calculated from the slopes fitted to the data shown in (a), as a function of the PMT's nominal high voltage fitted by a straight line; (d) correlation of the high voltage minus the high voltage of the reference PMT and the change of the transit time compared to the reference PMT over a range of 250 V for all PMTs in the first DU, and a linear fit to the data.*

Chapter 14

Summary

In this thesis, a novel type of optical sensor for the application in deep-sea neutrino telescopes, the multi-PMT digital optical module (DOM), is investigated. KM3NeT is the first detector to use this innovative technique boosting its overall sensitivity as well as energy and directional resolution compared to detectors using the conventional single-PMT module designs. Consequently, KM3NeT will largely contribute to a better understanding of the origins of high-energy cosmic neutrinos and of fundamental neutrino properties, in particular neutrino oscillations and the neutrino mass hierarchy.

By extensive testing of critical parameters, it has been shown that custom-designed 3-inch PMTs from different manufacturers to be used as optical sensors fulfil the requirements formulated by the KM3NeT collaboration. This guarantees stable operation and high performance of the multi-PMT DOMs used in KM3NeT. By using reflector rings surrounding the PMTs, the directional sensitivity and the overall effective area of the DOMs is increased. With the performed reflectivity measurements of different reflector ring materials combined with measurements of the PMT quantum efficiency and angular acceptance as well as glass sphere transmittance, the optimised solutions for material and layout were found.

A big challenge the multi-PMT design entails is the significantly increased data flow from the 31 PMTs compared to that from a single PMT. The solution to this is the data reduction performed, individually for each PMT, by the active bases . The analogue signals of the PMTs are transformed into start times and time over thresholds (ToT), considerably reducing the amount of data to be transferred and stored. The relation between the original signal charge and the ToT has been determined. Although the relation is not linear over the whole measured intensity range, it is well defined and thus enables the conservation of the information about the charge of the initial signal.

The angular acceptance scan performed of a fully assembled DOM proves the superior sensitivity of the multi-PMT design. With the development of advanced measurement techniques eliminating most of the background, a very accurate estimate of the DOM acceptance has been achieved. Small systematic discrepancies between data and Monte Carlo of the zenithal scan and the single PMT angular acceptances can be explained by the difference of the reflector ring angles (45° in the Monte Carlo setup and 48° in the measurement setup). The overall good agreement between data and Monte Carlo, confirms the viability of the results. Furthermore, they constitute valuable input for detector simulations and reconstruction algorithms.

A major part of this thesis is the calibration and data analysis of deployed prototype DOMs. The influence of bioluminescence on the background rate of the DOMs was investigated. It is shown that it can be significantly reduced by using coincident hits of two or more PMTs. Another source of background, ^{40}K decays in the sea water, was used for the in-situ time and efficiency

calibration of the PMTs in a DOM. Using dedicated algorithms, a precision of the time calibration of better than 1 ns is achieved. Moreover, the nanobeacon LED mounted at each DOM was used to perform a time calibration between different DOMs of a line with similar precision. Investigations of higher multiplicity coincidences reveal a single DOM's capability of identifying atmospheric muons. Due to the segmentation of the active area of the multi-PMT DOM, an estimation of the directional distribution of the muons could be performed.

An analysis of data from the first two lines deployed shows the influence of auxiliary structures in the DOM on the measured ^{40}K rate. By correcting for those structure effects, the efficiencies of the PMTs could be determined with very high precision so that even small variations in the quality of the glass spheres surrounding the DOMs can be identified. The achieved accuracy in efficiency and time calibration enables advanced reconstruction algorithms and thus improves the sensitivity of the KM3NeT detector to the direction and energy of the detected neutrinos. Furthermore, the behaviour of timing and efficiency characteristics of the DOMs upon PMT high-voltage variation was investigated comparing in-situ data to data from PMT lab measurements. The high-voltage-dependent single rates of the DOMs are in good agreement with the PMT rates measured in the lab. In addition, it was found that the absolute timing of the PMTs in a DOM can mostly be explained by their different nominal high voltages.

List of Figures

List of Tables

Bibliography

[1] V. F. Hess. Über Beobachtungen der durchdringenden Strahlung bei sieben Freiballonfahrten. *Physikalische Zeitschrift*, 13:1084–1091, November 1912.

[2] Wolfgang Pauli. Offener Brief an die Gruppe der radioaktiven bei der Gauvereins-Tagung zu Tübingen. In *Open letter to the group of radioactive people at the Gauverein meeting in Tübingen*, 1930.

[3] E. Fermi. Versuch einer theorie der β-strahlen. i. *Zeitschrift für Physik*, 88(3):161–177, Mar 1934.

[4] C. L. Cowan, F. Reines, F. B. Harrison, H. W. Kruse, and A. D. McGuire. Detection of the free neutrino: A Confirmation. *Science*, 124:103–104, 1956.

[5] Bruno Pontecorvo. Mesonium and antimesonium. *Zhur. Eksptl'. i Teoret. Fiz.*, 33, 1957.

[6] Y. Fukuda et al. Evidence for oscillation of atmospheric neutrinos. *Phys. Rev. Lett.*, 81:1562–1567, 1998.

[7] M. G. Aartsen et al. Probing the origin of cosmic rays with extremely high energy neutrinos using the IceCube Observatory. *Phys. Rev.*, D88:112008, 2013.

[8] IceCube web pages. `https://icecube.wisc.edu/`. Accessed: 2018-08-29.

[9] M. G. Aartsen et al. Multimessenger observations of a flaring blazar coincident with high-energy neutrino IceCube-170922A. *Science*, 361(6398):eaat1378, 2018.

[10] P. A. Cerenkov. Visible radiation produced by electrons moving in a medium with velocities exceeding that of light. *Phys. Rev.*, 52:378–379, 1937.

[11] U. F. Katz and Ch. Spiering. High-Energy Neutrino Astrophysics: Status and Perspectives. *Prog. Part. Nucl. Phys.*, 67:651–704, 2012.

[12] K. Hirata et al. Observation of a Neutrino Burst from the Supernova SN 1987a. *Phys. Rev. Lett.*, 58:1490–1493, 1987. [,727(1987)].

[13] R. M. Bionta et al. Observation of a Neutrino Burst in Coincidence with Supernova SN 1987a in the Large Magellanic Cloud. *Phys. Rev. Lett.*, 58:1494, 1987.

[14] Kenneth Greisen. End to the cosmic ray spectrum? *Phys. Rev. Lett.*, 16:748–750, 1966.

[15] G. T. Zatsepin and V. A. Kuzmin. Upper limit of the spectrum of cosmic rays. *JETP Lett.*, 4:78–80, 1966. [Pisma Zh. Eksp. Teor. Fiz.4,114(1966)].

[16] Enrico Fermi. On the Origin of the Cosmic Radiation. *Phys. Rev.*, 75:1169–1174, 1949.

[17] T. Piran. Gamma-ray bursts and the fireball model. *Phys. Rept.*, 314:575–667, 1999.

[18] Eli Waxman and John N. Bahcall. High-energy neutrinos from cosmological gamma-ray burst fireballs. *Phys. Rev. Lett.*, 78:2292–2295, 1997.

[19] VS Beresinsky and GT Zatsepin. Cosmic rays at ultra high energies (neutrino?). *Physics Letters B*, 28(6):423–424, 1969.

[20] M. Ageron et al. ANTARES: the first undersea neutrino telescope. *Nucl. Instrum. Meth.*, A656:11–38, 2011.

[21] J. A. Aguilar et al. AMADEUS - The Acoustic Neutrino Detection Test System of the ANTARES Deep-Sea Neutrino Telescope. *Nucl. Instrum. Meth.*, A626-627:128–143, 2011.

[22] S. Adrián-Martínez et al. The Positioning System of the ANTARES Neutrino Telescope. *JINST*, 7:T08002, 2012.

[23] Veronique Van Elewyck. Recent results from the ANTARES neutrino telescope. *Nucl. Instrum. Meth.*, A742:63–70, 2014.

[24] Agata Trovato. Recent results from ANTARES. *EPJ Web Conf.*, 99:06003, 2015.

[25] J. Ahrens et al. Icecube - the next generation neutrino telescope at the south pole. *Nucl. Phys. Proc. Suppl.*, 118:388–395, 2003. [,388(2002)].

[26] E. Andres et al. The AMANDA neutrino telescope: Principle of operation and first results. *Astropart. Phys.*, 13:1–20, 2000.

[27] Delia Tosi and Kyle Jero. IceTop as Veto for IceCube. *PoS*, ICRC2015:1086, 2016.

[28] R. Abbasi et al. The Design and Performance of IceCube DeepCore. *Astropart. Phys.*, 35:615–624, 2012.

[29] K. Hanson and O. Tarasova. Design and production of the IceCube digital optical module. *Nucl. Instrum. Meth.*, A567:214–217, 2006.

[30] Pietro Antonioli et al. SNEWS: The Supernova Early Warning System. *New J. Phys.*, 6:114, 2004.

[31] R. Abbasi et al. An absence of neutrinos associated with cosmic-ray acceleration in γ-ray bursts. *Nature*, 484:351–353, 2012.

[32] P. Bagley et al. (KM3NeT Collaboration). Conceptual Design Report. `https://www.km3net.org/wp-content/uploads/2015/07/CDR-KM3NeT.pdf`, 2006. Accessed: 2018-08-29.

[33] P. Bagley et al. (KM3NeT Collaboration). Technical Design Report. http://www.km3net.org/wp-content/uploads/2015/07/KM3NeT-TDR-Part-1.pdf http://www.km3net.org/wp-content/uploads/2015/07/KM3NeT-TDR-Part-2.pdf http://www.km3net.org/wp-content/uploads/2015/07/KM3NeT-TDR-Part3.pdf, 2008. Accessed: 2018-08-29.

[34] S. Adrián-Martínez et al. Letter of intent for KM3NeT 2.0. *J. Phys.*, G43(8):084001, 2016.

[35] S. Adrián-Martínez et al. Deep sea tests of a prototype of the KM3NeT digital optical module. *Eur. Phys. J.*, C74(9):3056, 2014.

[36] S. Adrián-Martínez et al. The prototype detection unit of the KM3NeT detector. *Eur. Phys. J.*, C76(2):54, 2016.

[37] KM3NeT web pages. http://www.km3net.org/. Accessed: 2018-08-29.

[38] M. G. Aartsen et al. Observation of High-Energy Astrophysical Neutrinos in Three Years of IceCube Data. *Phys. Rev. Lett.*, 113:101101, 2014.

[39] Bjoern Herold. Study of 40k-induced rates for a KM3NeT design option with multi-pmt optical modules. *Nuclear Instruments and Methods in Physics Research Section A: Accelerators, Spectrometers, Detectors and Associated Equipment*, 626–627, Supplement:S234 – S236, 2011.

[40] Hamamatsu Phtotonics. Photomultiplier tubes, basics and applications, 2007. Online available at: https://www.hamamatsu.com/resources/pdf/etd/PMT_handbook_v3aE.pdf; Accessed: 2018-08-29.

[41] S-O Flyckt and Carole Marmonier. Photomultiplier tubes, principles and applications, 2002. Online available at: http://www2.pv.infn.it/~debari/doc/Flyckt_Marmonier.pdf; Accessed: 2018-08-29.

[42] E. H. Bellamy, G. Bellettini, F. Gervelli, M. Incagli, D. Lucchesi, C. Pagliarone, F. Zetti, Yu. Budagov, I. Chirikov-Zorin, and S. Tokar. Absolute calibration and monitoring of a spectrometric channel using a photomultiplier. *Nucl. Instrum. Meth.*, A339:468–476, 1994.

[43] J. D. Cockcroft and E.T.S. Walton. Experiments with high velocity positive ions. (i) further developments in the method of obtaining high velocity positive ions., 1932. Online available at: http://rspa.royalsocietypublishing.org/content/royprsa/136/830/619.full.pdf; Accessed: 2018-08-29.

[44] Hamamatsu Photonics web pages. https://www.hamamatsu.com/. Accessed: 2018-08-29.

[45] ET Enterprises Limited web pages. http://www.et-enterprises.com/. Accessed: 2018-08-29.

[46] MELZ FEU web pages. http://www.melz-feu.ru/. Accessed: 2018-08-29.

[47] HZC Photonics web pages. http://www.hzcphotonics.com/en_index.html. Accessed: 2018-08-29.

[48] Jonas Reubelt. Characterisation of photomultiplier tube models to be used in the KM3NeT project. M.Sc. Thesis, Friedrich-Alexander Universität Erlangen-Nürnberg, Erlangen, 2012.

[49] Lew Classen. *The mDOM – a multi-PMT digital optical module for the IceCube-Gen2 neutrino telescope*. PHD Thesis, Friedrich-Alexander-Universität Erlangen-Nürnberg (FAU), 2017.

[50] D. Real et al. DOM electronics Technical Design Report. *KM3NeT internal note*.

[51] E. Grafarend and A. Heidenreich. The generalized mollweide projection of the biaxial ellipsoid. In Fernando Sansò, editor, *Geodetic Theory Today*, pages 52–52, Berlin, Heidelberg, 1995. Springer Berlin Heidelberg.

[52] Christophe M.F. Hugon. Step by step simulation of phototubes for the km3net and antares optical modules. *Nuclear Instruments and Methods in Physics Research Section A: Accelerators, Spectrometers, Detectors and Associated Equipment*, 787:189 – 192, 2015. New Developments in Photodetection NDIP14.

[53] Tamas Gal and Moritz Lotze. Km3pipe 8.2.1, August 2018.

[54] Diego Real and David Calvo. Nanobeacon and Laser Beacon: KM3NeT Time Calibration Devices. *PoS*, TIPP2014:365, 2015.

[55] C. M. F. Hugon. Results and simulation of the prototype detection unit of KM3NeT-ARCA. In *European Physical Journal Web of Conferences*, volume 136 of *European Physical Journal Web of Conferences*, page 04009, March 2017.

Acknowledgements

I would like to express my gratitude to the following people without whom finishing this thesis would not have been possible:

- Uli Katz for offering me the opportunity to write a dissertation in this very interesting field and for always having an open door and mind for arising questions,
- Alexander Kappes for serving as second assessor of this thesis,
- Oleg Kalekin for teaching me all the basics about PMTs and hardware in general and for his advice to help answering a variety of arising questions,
- my office colleagues for the amazing work atmosphere and in particular Lew Classen for the excellent collaboration in setting up and carrying out several lab measurements as well as Dominik Stransky and Tamás Gál for their help to improve my coding and understanding of physics as well as for their administrative work,
- Kay Graf for successfully being the highest authority for any kinds of questions,
- all other colleagues at ECAP and other institutes for the collaboration and fruitful discussions,
- Jannik Hofestädt, Robert Lahmann, Oleg Kalekin, Tamás Gál and especially Ulla Müller for proofreading this work,
- my family for always offering non-technical support and motivation and
- all other people i did not mention for supporting me during the journey.